DTM GENERATION IN FORESTED AREAS FROM FULL-WAVEFORM AIRBORNE LiDAR DATA

Damir Gumerov

A THESIS SUBMITTED TO THE FACULTY OF
GRADUATE STUDIES IN PARTIAL
FULFILLMENT OF THE REQUIREMENTS FOR
THE DEGREE OF MASTER OF SCIENCE

GRADUATE PROGRAM IN
EARTH AND SPACE SCIENCE
YORK UNIVERSITY
TORONTO, ONTARIO

November 2014

Abstract

This study was aimed at improving overall quality of Digital Terrain Model (DTM) extraction from full-waveform LiDAR data. Specifically, the primary goal was to develop a novel method to improve DTM extraction by utilizing low amplitude pulses that are generated by terrain under vegetation, but undetectable using traditional Gaussian decomposition techniques. The secondary objective was to validate the developed methodology using ground reference data.

An integrated approach was developed to detect weak returns backscattered by the bare terrain using full-waveform data and implemented using Microsoft Visual Studio. In this approach, echo detection, identification of terrain points, and generation of the triangulated irregular network (TIN) were iteratively carried out. To validate the proposed method, airborne LiDAR datasets obtained from a Riegl's LMS-Q560 over five study sites in the Great Lakes-St. Lawrence forest region near Sault Ste. Marie, Ontario, Canada were used. The generated DTMs were compared with those obtained from the commercial software, TerraSolid's TerraScan, based on ground measurements. The validation results show that using the developed method, the improvement in DTM was up to 21% for the five study areas, but up to 29% only considering heavily wooded areas with variable terrain. In addition, the developed methodology demonstrated an increase in LiDAR density and coverage of terrain points detected (up to 10-15%), when compared to TerraScan's ground extraction routine.

Acknowledgments

First and foremost I would like to thank my supervisor Dr. Baoxin Hu and Professor Jian-Guo Wang for their guidance, encouragement and for their support during the many years of my graduate studies.

I would also like to thank my peers: Anna Jarvis and Sara Mazrouei for all their help with putting the final drafts of the thesis together as well as Jili Li and Julien Li-Chi-Ming for their help with the field survey portion of the data acquisition.

A special thank you to my strongest supporters in this endeavor -my wife and my parents. They have continued to encourage me throughout the past few years and without their support I do not think that I would have accomplished this.

Table of contents

List of Tables

List of Figures

List of Acronyms

3D	Three Dimensional
ALS	Airborne Laser Scanning
CBN	Canadian Base Network
CGAL	Computational Geometry Algorithm Library
CGVD28	Canadian Geodetic Vertical Datum of 1928
COSINE	Control Survey Information Exchange
CSRS	Canadian Spatial Reference System
DG	Direct Geo-referencing
DSM	Digital Surface Model
DTM	Digital Terrain Model
ECEF	Earth Centered Earth Fixed
EDM	Electronic Distance Measurement
EO	Exterior Orientation
FW	Full-Waveform
GNSS	Global Navigation Satellite System
GPS	Global Positional System
GSL	GNU Scientific Library
Hz	Hertz
IDW	Inverse Distance Weighting
IMU	Inertial Measurement Unit
ITRF	International Terrestrial Reference Frame

IR	Infra Red
LiDAR	Light Detection and Ranging
LM	Levenberg-Marquardt
NAD83	North American Datum of 1983
NED	North East Down
NRCan	Natural Recourses Canada
POS	Position and Orientation System
RMS	Root Mean Square
RMSE	Root Mean Square Error
SE	Structure Elements
SGD	Seeded Gaussian Decomposition
SBET	Smoothed Best Estimated Trajectory
TIN	Triangulated Irregular Network
UTM	Universal Transverse Mercator
WGS84	World Geodetic System of 1984

List of Symbols

A	amplitude of the Gaussian function
a	semi major axis
A, B, C	vertices defining a TIN facet
B_r	the width of a laser beam
a, b, c	parameters defining a line in 3D space
b_i	noise of sample i
c	the speed of light
D	the iteration distance
D_r	the diameter of receiver aperture
e	eccentricity
f_j	function value at sample point j.
h	ellipsoidal height
J	Jacobian Matrix
$M(i)$	mean of an opened DSM with a disk SE of a diameter i metres
N	the radius of curvature
P_r	the received signal power
P_t	the transmitted signal power
R	the range from sensor to target
R^2	correlation value
S	total station distance measurement
S_k	parameter is the measure of asymmetry of the Gaussian model

T	amplitude threshold
t	time of flight
u, v	unit vectors
v_g	the group velocity of the laser pulse
x_i	time of sample i
X_i, Y_i, Z_i	3D vector defined with respect to frame i
X_o, Y_o, Z_o	coordinates of a point of origin
X_{oi}, Y_{oi}, Z_{oi}	3D origin of the scanner defined with respect to frame i
y_i	amplitude value of sample i
α	is the shape parameter that defines the “sharpness” of the peak
ΔX, ΔY, ΔZ	the lever arm parameters
Δx, Δy, Δz	components of a 3D unit vector
ΔX_P, ΔY_P, ΔZ_P	components of a 3D vector from a facet vertex to point P
η_{atm}	the atmospheric transmission factor
η_{sys}	the system transmission factor
θ	the iteration angle
Θ	the terrain angle
λ	latitude
μ_k	is the position of the centre of the pulse
ξ	total station horizontal angle measurement
ρ	conversion from radians to seconds
σ	standard deviation, width of a Gaussian function
$\sigma(R)$	the differential backscattering cross-section

Φ	longitude
ϕ_K	the function describing each echo (return)
ψ	total station vertical angle measurement,
$(\omega, \theta, \varphi)$	roll, pitch, yaw
$\overrightarrow{\mathrm{AC}}$	vector
$\left\|\overrightarrow{\mathrm{AC}}\right\|$	norm of a vector

1 Introduction

A Digital Terrain Model (DTM) is an indispensable product in a wide variety of applications. DTMs have become essential in geospatial analysis and are an important part of the workflow in such applications as building extraction, 3D urban modelling and planning, hydrological monitoring, and costal/forestry management (Gonga-Saholiariliva et al., 2011; Liu, 2008). Traditionally DTMs are generated using surveyed data, either by land surveyors or using photogrammetric sensors. In the past decade, airborne light detection and ranging (LiDAR) or airborne laser scanning (ALS) has emerged as the main tool in use for the acquisition of the data used for the generation of DTMs (Hodgson et al., 2005). The collected airborne LiDAR data, as well as the traditional photogrammetric data are capable of covering substantially more terrain at a fraction of the time compared with the traditional land surveying techniques (Glennie, 2007; Liu, 2008). In terms of airborne LiDAR versus photogrammetric data, one is able to produce a terrain model with a higher resolution in vegetated and/or homogeneous areas using LiDAR data. In addition, processing LiDAR data is not labour intensive. These reasons make the LiDAR technique more suitable for DTM generation than digital imaging sensors (i.e., photogrammetric techniques). Research has indicated that the vertical accuracy of the DTM products generated from LiDAR data can be as high as 15 cm for open, flat, and hard surfaces (Su and Bork, 2006). However, the achievable accuracy of LiDAR-derived DTMs tends to deteriorate in vegetated landscapes, such as those areas covered with shrubs and trees.

As a result of some major improvements in data acquisition methods that have occurred over the past 10 years, a new type of LiDAR instrument, namely small footprint full-waveform LiDAR, has become available. The increasing availability of the small footprint full-waveform airborne LiDAR system provides a good opportunity for the improvement of DTM generation. This new product offers certain advantages over the previous discrete LiDAR instrument. Full-waveform systems store the whole signature of the returned signal (Mallet and Bretar, 2009), and thus the shape of a waveform can be analyzed to achieve high multi-target resolution and range accuracy (Chauve et al., 2007). In addition, waveform parameters such as the pulse width and the backscatter cross-section can be used to improve the separation between terrain and vegetation, which is a crucial step in DTM generation (Wagner et al., 2008). However, the classification of terrain points in a dense natural forest is still very difficult if one only uses the waveform parameters (Wagner et al., 2008). Based on these findings, Lin and Mills (2009) proposed a novel routine to integrate the pulse width information into the progressive densification filter developed by Axelsson (2000). This approach was demonstrated to be more effective at removing low vegetation points as well as being able to generate accurate DTM. In the methodology introduced by Lin and Mills (2009), it was necessary to derive the pulse information based on the Gaussian decomposition method (Lin et al., 2008, and Reitberger et al., 2008) before the integrated filter process.

Most of the methods mentioned above, however, cannot be applied to the low amplitude pulses that are commonly associated with bare earth in the heavily wooded areas, since

the extracted parameters of the low amplitude echoes are not reliable (Wagner et al., 2006). These weak echoes are too close to the noise threshold of the instrument which can cause erroneous results in the determination of the parameters through Gaussians fitting. Thus, weak echoes from the terrain may not be detected using the Gaussian decomposition method, which will be discussed in detail in Section 4.

As an example of the problem this study was trying to solve, Figure 1.1 shows a full-waveform signature produced by a tree and the underlying terrain (blue segmented line). The red curves in Figure 1.1 are the results of fitting four Gaussian functions to the observations. By examining the path of the emitted laser pulse, it could be seen that the weak echo circled in black was backscattered by the bare terrain under the tree; however, it could not be detected by the Gaussian decomposition method. On the other hand, if the Gaussian decomposition was constrained to only the circled interval, the weak terrain echo could be detected, as shown by the green curve. Figure 1.1 shows clearly if one knows where to look for a weak echo along the recorded full-waveform, one can detect it.

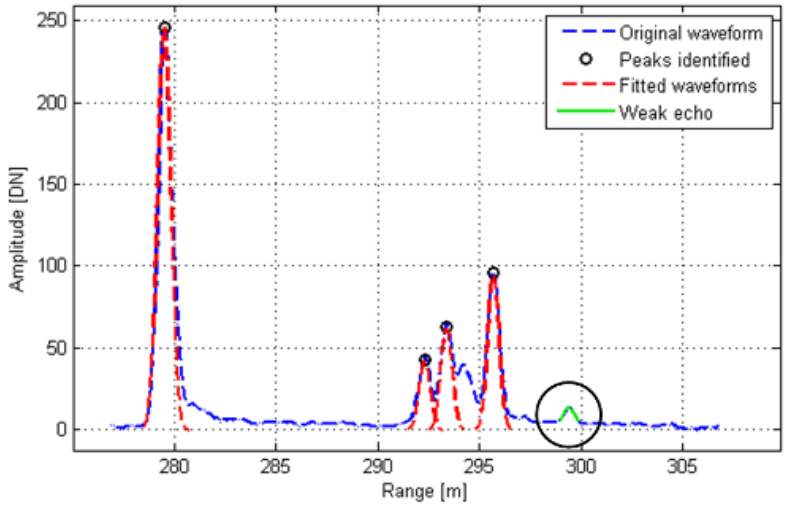

Figure 1.1 An example of a returned full-waveform of a laser pulse passing through a tree (blue line), and the modelled waveform obtained by fitting the summation of 4 Gaussian functions to whole waveform (red line). The circled echo was returned by the terrain and the green curve is the fitted weak echo.

Inspired by the results demonstrated in Figure 1.1, I developed an integrated approach to detect weak returns backscattered by the bare terrain using full-waveform data. In this approach, echo detection, identification of terrain points, and generation of the TIN were iteratively carried out. Specifically, the initial TIN was built through the use of the identified terrain points. This TIN was then used to guide the detection of the weak echoes backscattered by the terrain, yet undetected by the initial Gaussian decomposition process due to the noise constraints. To accomplish weak echo detection, for every individual TIN facet, all the returns passing through this TIN facet (the seeded search region) were examined for terrain echoes. The newly detected returns together with the original terrain points were then used to start the next iteration of ground point detection. This iterative process was performed until no further terrain points were detected.

This integrated approach allowed for the inclusion of lower amplitude pulses corresponding to the location of the ground, and as a result improved the generated DTM by means of point densification.

To test the developed method, airborne LiDAR datasets provided by GeoDigital International were used. These datasets were collected over northern Ontario from a helicopter platform using a Riegl's LMS-Q560 LiDAR instrument and Applanix' POS AV™ (a GNSS (Global Navigation Satellite System) aided inertial integrated navigation system) during a data acquisition campaign in August 2009. Except for the post-possessed navigation solution, the SBET (smoothed best estimated trajectory), the raw data processing and the designed methodology for DTM extraction were realized using a software utility I implemented in C/C++ using Microsoft Visual Studio. In terms of validation of the obtained results, the results were compared with those obtained from a ground survey and by the commercially available software TerraSolid.

The thesis structure is organized in the following manner: In Chapter 2, the background information on the LiDAR technology and DTM generation is provided. Chapter 3 includes the description of the used LiDAR data and their preliminary processing. The procedures for direct geo-referencing of the full waveform data and the collection of the reference data are also described in Chapter 3. Chapter 4 describes an implementation of the commonly used Gaussian decomposition method. The strategy used to detect "the ringing effect" is also integrated to the Gaussian decomposition method. The novel

integrated approach is introduced in detail in Chapter 5. Chapters 6 and 7 outline the performed validation and conclude with error analysis and summary of findings, followed by a discussion of potential future work.

2 Background

This chapter begins with an introduction to the fundamental principles of airborne LiDAR systems. An overview of full-waveform LiDAR systems, their operating principles and raw data processing techniques are then provided. Finally, an introduction to terrain modelling is presented, and existing methodologies for the extraction of bare ground from LiDAR data are discussed.

2.1 The LiDAR technology

Over the past decade, the acquisition and analysis of topographic data have seen a significant advancement in terms of technologies and methodologies associated with the use of LiDAR data. A LiDAR instrument is primarily designed for terrain mapping and general geospatial data collection. It is capable of collecting vast amounts of accurate 3D data and has been used more and more extensively over recent years, not only in the field of remote sensing and photogrammetry, but also in a wide variety of applications such as preservation of historical buildings and sculptures, aiding in the navigation of unmanned vehicles, and even as a tool to study the atmosphere on Mars (Whiteway et al., 2008).

2.1.1 Basic principles

A LiDAR instrument employs either continuous or pulsed lasers. The majority of commercially available LiDAR systems are operated by emitting short infrared (IR) pulses. It is these type of systems which the following discussion will be focused on. As

the emitted pulse propagates through space and interacts with the objects along its path, some of its energy is reflected back to the LiDAR instrument. The backscattered energy is then collected by the receiving sensor and recorded. A timing device in the instrument then time-tags the backscattered signal. The difference in time between when the emitted pulse leaves the LiDAR instrument and when the reflected signal arrives back to the unit is used to calculate the distance to the object as per Equation (2.1):

$$R = c\frac{t}{2} \tag{2.1}$$

wherein c is the speed of light and t is defined as the time of flight of the pulse from the emitter to the target and back. A comprehensive list of formulas and relations applicable to LiDAR is provided in Baltsavias (1999).

In addition to obtaining range information from the backscattered signal, an intensity value can be obtained from (Wagner et al., 2004):

$$P_r = \int_{R_1}^{R_2} \frac{D_t}{4\pi R^4 \beta_t^2} \cdot \eta_{sys}\, \eta_{atm} \cdot P_t\left(t - \frac{2R}{v_g}\right) \cdot \sigma(R) dR \tag{2.2}$$

wherein:

P_r the received signal power,

P_t *the* transmitted signal power,

D_r *the* diameter of receiver aperture,

R *the* range from sensor to target,

B *the width of* laser beam,

η_{sys} the system transmission factor,

η_{atm} *the* atmospheric transmission factor,

v_g *the* group velocity of the laser pulse,

$\sigma(R)$ the differential backscattering cross-section, and

dR the interval dR.

Equation 2.2 shows that the power of the received signal is a function of the transmitted signal, the optical properties of the LiDAR system, the atmospheric conditions, and the properties of the objects in the beam's path. The latter depends on the area of interaction with the beam and the reflective properties of the object (directionality and strength) (Wagner et al., 2004). These two factors are represented by a single variable, namely the backscatter cross-section. Since the scanned objects are not always flat and/or perpendicular to the path of the laser pulse, the integral is taken to include the full distance of the interaction of the beam with the target.

In most LiDAR applications, the 3D coordinates of a target object need to be obtained. To obtain the coordinates, it is necessary to know the position of the LiDAR sensor at the time when the pulse is emitted and the corresponding attitude of the laser beam, in addition to the range from the instrument to the scanned object.. It is thus common with modern mobile geospatial data acquisition that a direct geo-referencing (DG) system is employed to provide the exterior orientation (EO) parameters for a LiDAR system or other imaging sensors at all times.

A high quality DG system is typically a GNSS aided inertial integrated navigation system, such as a POS^{TM} (Position and Orientation System) manufactured by Applanix Corporation (www.applanix.com), which principally consists of GNSS receivers and Inertial Measurement Units (IMU) and estimates the 3D kinematic trajectory of a mobile platform. Although the EO of the LiDAR platform can be obtained in real-time, post-processing is generally introduced in order to achieve a more accurate and reliable solution. To correctly apply the EO, additional information is required in order to properly connect the LiDAR sensor and the IMU sensor: the lever arms and boresight angles between the two. An implementation of DG along with corresponding mathematical equations is described in Section 3.4.

2.1.2 Basic components of a LiDAR instrument

A LiDAR instrument is composed of a laser transmitter, a receiver, scanning mechanism, storage medium, and an operating system for signal digitization and on-line data acquisition (Wagner et al, 2004). Figure 2.1 gives a simplified component diagram of a LiDAR scanner.

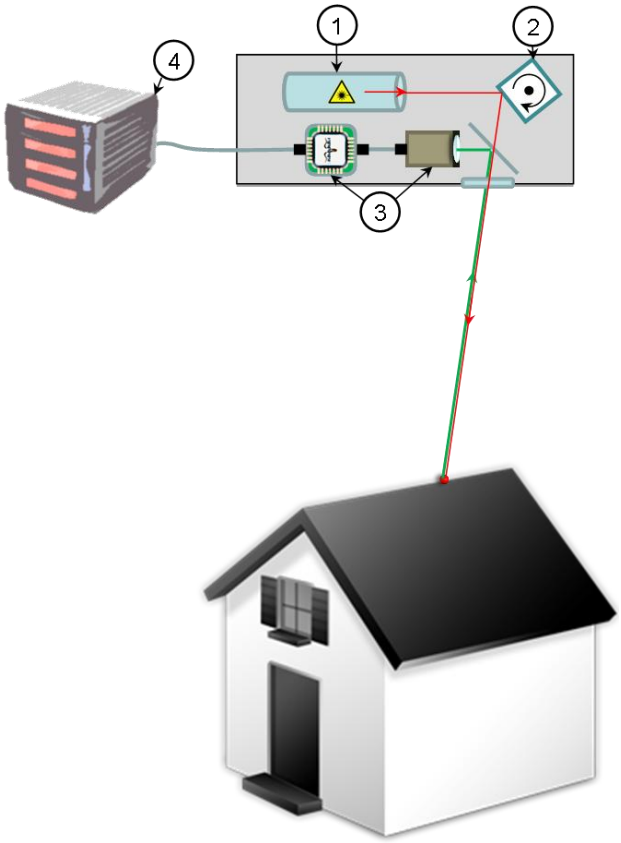

Figure 2.1 A Sketch of basic components of a LiDAR system that is composed of an emitter unit (1), scanning mechanism (2), receiver components (photodiode and digitiser) (3), and a storage unit (4)

The backbone of a LiDAR system is a laser (Light Amplification by Stimulated Emission of Radiation) which generates the emitted pulse. Every laser consists of three components: active material, a power system, and an optical system (Petrie et al., 2009).

The first component of a laser, the active material, has electrons that can be excited to raise their energy level for the purpose of photon generation. There are two types of active materials that are commonly used for topographic application laser. They are solid-state crystalline material such as neodymium-doped yttrium-aluminum garnet (Nd:YAG

λ=1046 nm) and a semiconductor material such as gallium arsenide (GaAs λ=835-840 nm). Both provide a typical pulse length (width) of around 4-10 ns.

To produce a pulse, energy is first pumped into the active material (which is referred to as "pumping" the laser). The solid-state laser uses a high intensity discharge lamp or a laser diode in the pumping process. In lasers that employ a semiconductor active material, an electrical power unit directly passes the current through the active material. This addition of energy is required in order for the electrons in the material to accumulate the energy required to jump to higher "metastable" states. Then, from these states, eventually the electrons will drop back to their lower (stable) states, at which time "spontaneous emission" occurs. "Spontaneous emission" causes the electrons to release energy in the form of photons of a certain wavelength. By chain reaction, other adjacent atoms also emit photons of the same frequency and phase. This process is referred to as the "stimulated emission". This whole process takes place in an enclosed chamber which is fully reflective on one side and semi-reflective on the other which allows the energy to build up inside the chamber. Once a critical amount of energy is reached, the energy is released in the form of a coherent beam or a short pulse.

The emitted pulse travels through the optics to the scanning mechanism of the LiDAR instrument. Figure 2.2 demonstrates the most commonly used scanner mechanisms: rotating mirrors, osculating mirrors, Palmer scanners, and optical fibers.

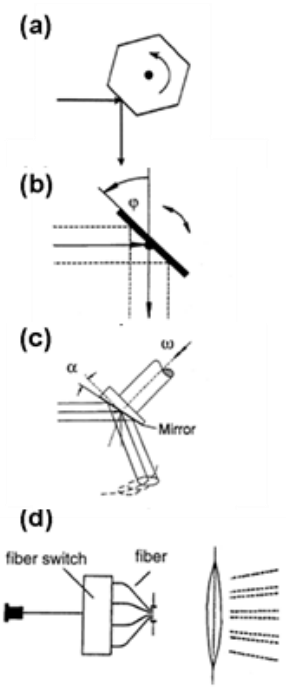
(a)
(b)
φ
(c)
ω
α
Mirror
(d)
fiber switch
fiber

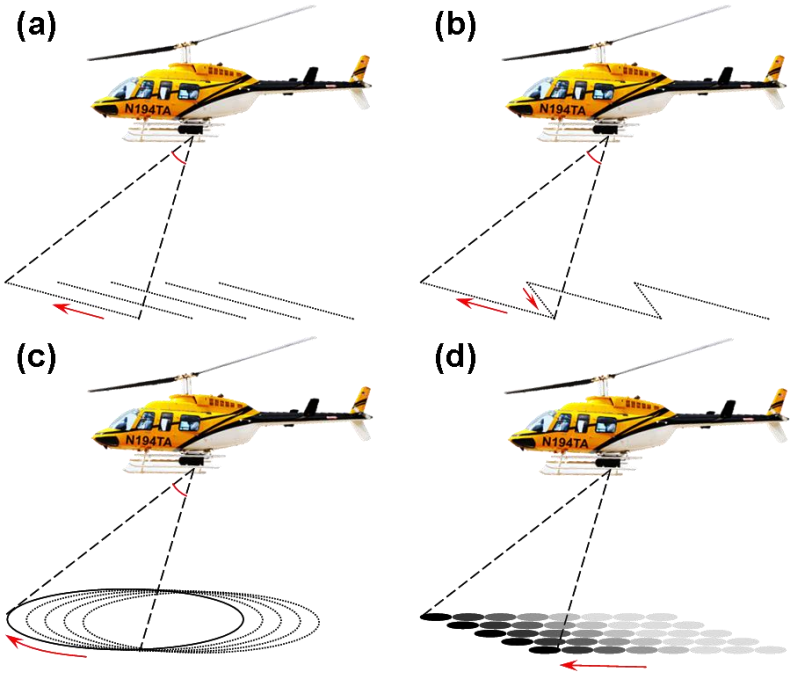

Figure 2.2 Scanning mechanisms and their resulting scan patterns: (a) rotating polygon, (b) oscillating mirror, (c) Palmer scanner, (d) fiber scanner. (Wehr at el. 1999).

Rotating mirror systems (also known as line scanners) produce sequential line by line scanning patterns (Figure 2.2a). The polygon mirror inside the LiDAR rotates at a constant rate, which makes it possible to produce uniform point sampling from line to line without errors associated with the changes of speed and accelerations of the mirror. The limitation of these scanning systems is their low flying height, as well as the swath width limitation based on the characteristics of the rotating mirror (time corresponding to distance traveled between the consecutive scan lines). The oscillating mirror can also be used as a scanner mechanism, in which the mirror moves back and forth to produce a zigzag scanning pattern (Figure 2.2b). These types of systems scan the ground continuously (no gaps as with the rotating mirror) and can be operated at high flying heights. However due to decelerations and accelerations of the mirror, which is

associated with a change of the scanning direction, some errors can be introduced into the data. In addition, the changes in velocities that the mirror experiences cause unequal spacing among the measured points, with higher point density occurring towards the edges of the scanning coverage and lower one at nadir (Wehr and Lohr, 1999). The third type of scanner mentioned above is the Palmer scanner, also called the nutating mirror, which produces an elliptical pattern (Figure 2.2c). With this pattern it becomes possible to measure the ground (closer to nadir) twice from different directions, once in the forward scanning position and once in the backward scanning position. This technique enables recording of points that might have been occluded if they were scanned from one direction only (Schaer, 2010). The drawback is that Palmer scanner systems do have a reduced field of view compared with the line or the oscillating mirror scanners. Another type of scanner is the optic fiber scanner, which is only employed by the company TopoSys, and uses an array of fibers to scan line by line. This type of scanners has a very narrow field of view compared with all the other systems. However they are able to scan lines at a substantially faster rate than any of the mirror scanners (Schnadt and Katzenbeisser, 2004). The fiber scanners produce systematic point coverage with high point densities.

After a pulse travels out of the system and comes in contact with an object, some of the energy is scattered back towards the unit where it is picked up by a detector and recorded. The detector captures the pulse and converts the optical signal of the incoming backscatter into an electronic signal. A receiver is composed of a photodiode with a

specific detector diameter (this quantity is used for a variety of calculations), which is connected to the preamplifier. The preamplifier passes the signal to a digitizer, which then converts the analogue signal to a digital one and transfers the digitized data to the storage medium.

2.2 Classification of LiDAR instruments

The commercial LiDAR instruments can be classified into two broad categories: discrete and full-waveform (FW). This categorization is based on the ability of LiDAR instruments to record the returned pulses. A FW LiDAR instrument is able to record the full signature of a returned signal, while a discrete instrument only records the locations of trigger pulses (the suspected target locations). There are some FW instruments that can record discrete pulses at the same time as the full waveform of a returned signal is being recoded.

2.2.1 Discrete return LiDAR instruments

Discrete return LiDAR instruments detect targets by identifying discrete "trigger pulses" in real-time from the backscatter signal. This process is commonly referred to as the on-the-fly range determination or pulse detection. This on-the fly pulses detection is accomplished by the hardware triggers built into the instruments. The trigger pulses, which are the discrete return pulses measured by the LiDAR system, are the results of interactions between the LiDAR emitted signal and the objects in its path, where some of the emitted IR signal is reflected back to the detector. It is common for LiDAR systems

to store the time-stamped location of a trigger pulse (time of flight or range) as well as its amplitude. In the past, discrete LiDAR instruments had the capability of recording only a single return per emitted pulse (first or last). However, as the technology has matured, the ability to record multiple targets has become a state-of-art standard.

Usually, the manufacturers of LiDAR instruments do not provide any information about the methods employed in their products for pulse detection (Mallet et al., 2009). In consequence, one may have no way of knowing the overall quality of the range measurements. There are a number of potential problems associated with the pulse detection methods used by discrete LiDAR instruments (Wagner et al., 2004). The shortcomings of the on-the-fly range determination utilized in discrete LiDAR systems are demonstrated in Figure 2.3. Firstly, the accuracy of the range estimation is often unreliable (Wagner et al., 2004), as certain algorithms do not necessarily detect the peak value of the return, but use thresholds to locate the "trigger pulses". Secondly, the algorithms used in many cases are unable to distinguish multiple targets from the returning signal, if they are located too close to each other in the profile of the laser beam. Therefore, those targets that have a sub-metre vertical separation often become indistinguishable. In addition, there is data loss that occurs due to thresholds and constraints imposed on the real-time detection algorithm by the manufacturers. These thresholds do act as a safeguard from false detections, but can also cause some of the low amplitude returns not to be detected as a result of the thresholds.

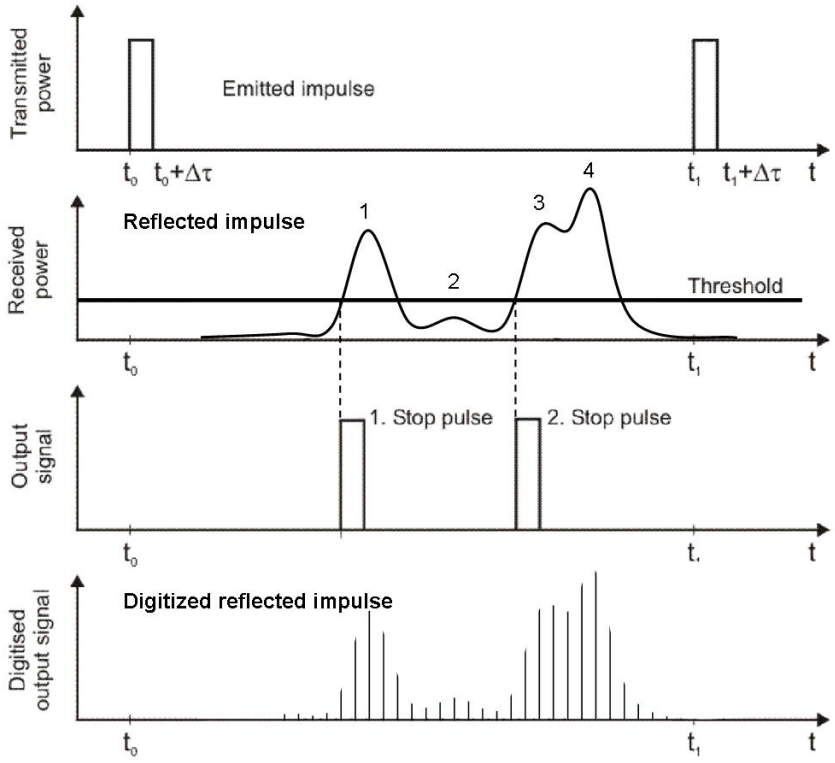

Figure 2.3 Types of errors related to the pulse detection techniques (Wagner et al., 2004) employed by discrete LiDAR instruments: error in range to the target (return #1); returns that are not picked out due to its low amplitude (lower than the threshold, return #2); and multiple returns that are registered as a single return (return #3 and #4).

2.2.2 Full-waveform LiDAR instruments

A full-waveform LiDAR instrument records the transmitted pulse and backscattered signal as a sampled waveform (Figure 2.4). This ability of a FW instrument offers certain advantages over a discrete return one.

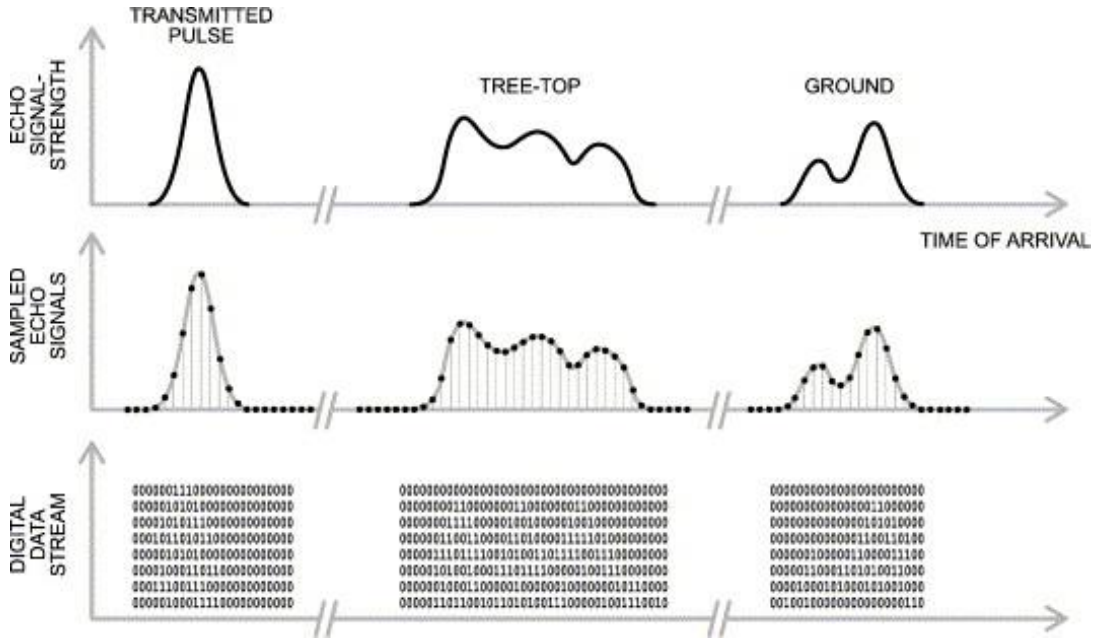

Figure 2.4 An example of the sampled waveform that is stored by the FW LiDAR, where both the transmitted and received signals are stored in 8 bit blocks for post processing. (Wagner et al., 2008)

In 2004, the first small-footprint Airborne Laser Scanner (ALS) system with the capability to record the waveform of the backscattered signal became available in the commercial market (Hug et al., 2004). The recorded waveform provided the possibility for retrieval of accurate range measurements along with other physical properties of the objects that fall in the laser footprint. Waveform parameter extraction was accomplished by using the advanced algorithms to detect return pulses in the recorded full-waveform data, such as the Gaussian decomposition or Gaussian fitting algorithms. Low amplitude

returns could now be identified from the recorded data by using a more complex analysis than the one used in a discrete LiDAR instrument (Jutzi and Stilla, 2005).

Although the full-waveform system does perform better than the discrete system in terms of distinguishing targets that are close together, there are still some limitations associated with the target separation. The range resolution for full-waveform LiDAR scanners is equal to $v_g\tau/2$, where τ is the emitted pulse duration and v_g is the group velocity of the laser in the atmosphere (Wagner et al., 2006). With a 4 nanosecond pulse, the corresponding targets with the vertical separation of less than 0.6 m become difficult to distinguish. Low amplitude return pulses pose another problem: if the amplitude of a returned pulse is too close to the noise level of the signal, the standard procedures used for pulse detection will not be sufficient to detect this target.

The commercial full-waveform pulse fitting algorithms impose thresholds and constraints to avoid false detection. One of the reasons for thresholds is to cope with the ringing effect of the scanner, which is caused by the detector electronics of the LiDAR (Magruder and Neuenschwander 2009). The Avalanche photodiode technology most commonly used by LiDAR is susceptible to this phenomenon. The ringing effect occurs when a backscatter signal is received by the photodiode from a highly reflective surface (or simply a high amplitude return). This high amplitude return causes oversaturation, as a number of the carriers associated with Avalanche process become trapped inside the electronics, and then subsequently released moments later. This delayed release causes

the appearance of an additional waveform in the recorded return signal. To ensure that the extracted points are of the best quality, the issues mentioned above have to be appropriately handled when the full-waveform data are processed.

There are a number of small footprint systems with full-waveform capability currently available in the market, for example:

- Riegl – LMS Q560 (www.riegl.com/),
- TopoSys – Falcon III (Now part of Trimble Geospatial), which is the only system to use fiber optics for transmitting/receiving the waveform,
- TopEye/Blom – Mark II (www.topeye.com/),
- Optech – ALTM 3100 (www.optech.ca/), and
- Leica – ALS60 (http://www.leica-geosystems.com/).

Part of their technical specifications are summarized in Table 2.1

Table 2.1 Technical specifications of full-waveform LiDAR systems (Mallet et al. 2009)

System	Pulse energy (mJ)	Pulse width (ns)	Scan rate (Hz)	Scan angle (˚)	Beam divergence (mrad)	Footprint size (m)	Range accuracy (cm)	Digitizer (ns)
LMS Q560	0.008	4	5-160	45	0.5	0.5@1 km	2	1
Falcon III	-	5	165-415	28	0.7	0.7@1 km	-	-
MarkII	-	4	<50	14/20	1	1@1 km	2-3	1
ALTM 3100	<0.2	8	<70	50	0.3/0.8	0.3/0.8@1 km	1	1
ALS60	<0.2	5	<90	75 usually	0.22	0.22@1 km	2	1

System	Company manufacturer	Platform	Beam deflection	Release year	Wavelength (nm)	Flying height (km)	Pulse rate (kHz)
LMS Q560	Riegl	Airborne	Polygon	2004	1550	<1.5	≤100
Falcon III	TopoSys	Airborne	Fibers	2005	1560	<2.5	50-125
MarkII	TopEye	Airborne	Palmer	2004	1064	<1	≤50
ALTM 3100	Optech	Airborne	Oscillating mirror	2004	1064	≤3.5	≤70
ALS60	Leica	Airborne	Oscillating mirror	2006	1064	0.2-6	≤50

2.3 Full-waveform data processing

A returned waveform can generally be represented as the sum of *n* components corresponding to *n* objects encountered by the beam as follows (Mallet et al., 2009):

$$y_i = \sum_{k=1}^{n} \phi_k(x_i) + b_i \tag{2.4}$$

wherein y_i is the amplitude value of the waveform at time x_i, ϕ_k is the function describing each echo (return) at time x_i, and b_i is the noise.

The most commonly used function for ϕ_k is the basic Gaussian curve as follows (Mallet et al. 2009):

$$\phi_k(x_i) = A_k \exp\left(-\frac{(x_i - \mu_k)^2}{2\sigma_k^2}\right) \tag{2.5}$$

wherein A_k is the amplitude of the Gaussian function, σ_k is the pulse width (duration), and μ_k is the position of the centre of the pulse.

In addition to these listed Gaussian functions, other functions such as the logarithmic and generalized Gaussian models can be used as well. The Generalized Gaussian model is (Chauve et al., 2007):

$$\phi_k(x) = A_k \exp\left(-\frac{|x - \mu_k|^{\alpha_k^2}}{2\sigma_k^2}\right) \tag{2.6}$$

where α is the shape parameter that defines the "sharpness" of the peak (Figure 2.6, right).

The Lognormal Gaussian model is (Chauve et al., 2007):

$$\phi_k(x) = A_k \exp\left(-\frac{(\ln(x - s_k) - \mu_k)^2}{2\sigma_k^2}\right) \tag{2.7}$$

wherein S_k parameter is the measure of asymmetry of the Gaussian model (Figure 2.5. left).

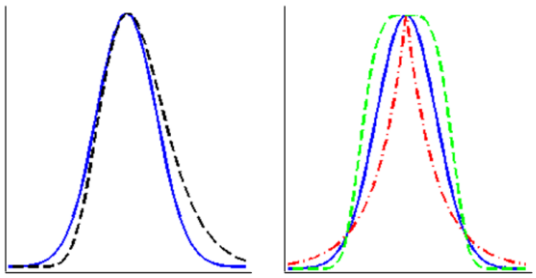

Figure 2.5 Left: Comparison between Gaussian (continuous line) and Lognormal (dashed black line) functions. Right: The generalized Gaussian functions with: α=1 is Laplace function (red dashed line), α=√2 is Gaussian function (continuous blue line), and α=2 a flattened shape (green dashed line) (Chauve et al., 2007)

The influence of the parameter α is demonstrated in Figure 2.5. α provides another piece of information about the shapes of the echoes which could be used for classification purposes, in addition to echoes width and amplitude. In Chauve et al. (2007), the fitting of the abovementioned Gaussian models is compared and discussed, and the conclusion is made in favour of using the generalized Gaussian fit.

The parameters used to describe the Gaussian curves (μ, σ, A) are linked to the geometric and radiometric properties of the target objects and the properties of the emitted pulse. The mean value (μ) is used to determine the range to the object from the LiDAR sensor, and thus is instrumental in determining the location of the target in space. The width (σ)

of the pulse provides information on the roughness of the target and is also influenced by the slope of the terrain. For a flat and "smooth" surface, the response will be similar to the emitted pulse in shape. When scanning objects that have more vertical variations (shrubs or grass), the return pulse will be wider. In addition, an increase in the angle of incidence at which the LiDAR's emitted pulse strikes a flat surface, will also result in an increase in the width of the resulting return. The amplitude (*A*) of the returned pulse is affected by the roughness and reflectivity of the scanned objects and the incidence angle.

2.4 DTM extraction

One of fundamental products derived from LiDAR data is the digital terrain model (DTM) (Liu, 2008). An accurate terrain model is critical, since many LiDAR products are derived from or using the terrain model. To generate a DTM, LiDAR points corresponding to the terrain need to be extracted or filtered from the point cloud (Figure 2.6).

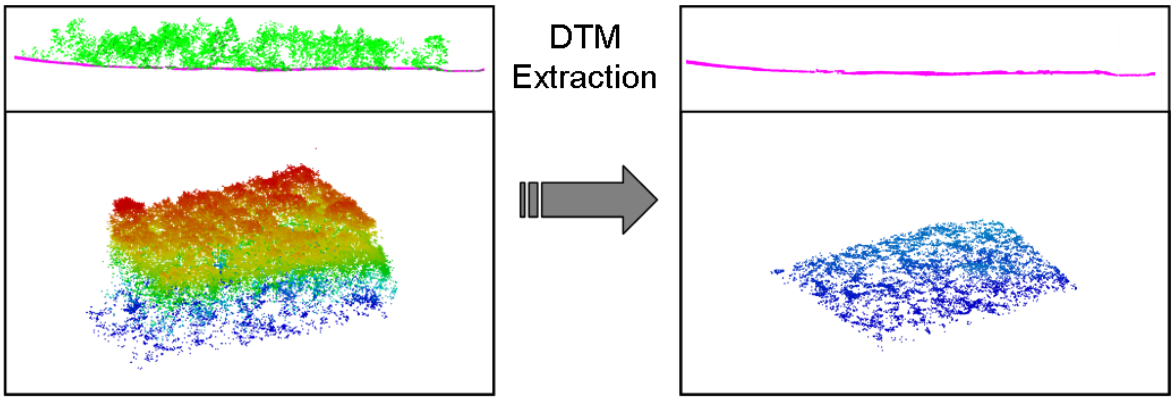

Figure 2.6 A demonstration of the DTM extraction provided in profile and in 3D views. Images on the left are of the original point cloud and on the right are the extracted terrain points.

As a result, the most essential step in the generation of DTM is the identification of the terrain points from the LiDAR data (Pfeifer et al., 2007). In general, the more ground points one has, the more accurate the resulting DTM will be. However, if points corresponding to low laying vegetation were included in the DTM generation, the resulting model might become erroneous. It is, therefore, important to separate LiDAR points generated by bare terrain from others, especially those resulted from low vegetation canopies. The question is how to separate the terrain points from the rest of the data, with minimal user input and lowest possible error, which is a critical issue that researchers try to solve in order to generate accurate DTMs, especially in vegetated areas. So far, many methods have been developed to generate DTMs from LiDAR data. The algorithms designed for the DTM extraction from discrete LiDAR data tend to utilize the geometrical properties of the point clouds. The filtering of the terrain using both the radiometric parameters and the geometrical properties has been substantially improved after the introduction of small footprint full-waveform LiDAR. This improvement is in large due to the fact that with full-waveform LiDAR a number of new parameters became available to the user. The use of these new parameters leads to an increased accuracy in the separation of terrain and non-terrain points. Generally full-waveform provides more points to work with and higher accuracy range determination - thus producing a better quality DTM than discrete return LiDAR instruments. The existing methods for the generation of DTMs can be classified into the following four categories: morphological filters, iterative surface models, segmentation/cluster based methods, and progressive TIN methods.

2.4.1 Morphological filters

Basic morphological filters are simple in concept and operation. In order to prepare the dataset for a morphological filter, the point cloud often has to be gridded first (Meng et al., 2010). A window of a set size and shape is then used to traverse through the grid going over every cell. When the window is centred on a given cell, the lowest value within the range of the window is assigned to the centre cell. This is termed as erosion operator. After the minimum values are assigned, using the same procedure and shape, the resulting grid is traversed again, however this time the maximum value in the window is assigned instead, which is referred to as the dilation operator. The grid obtained has a low pass filtered "appearance" since the high frequency components are removed. The window size of the morphological filter dictates the maximum size of the object that will be removed from the scene. Thus, the filter preserves the features that are larger in size than the window used. However, the smaller variations of the ground surface would be smoothed out, and the detailed features of the surface would be lost (Chen et al., 2007). This problem with the morphological filters was resolved in Arefi and Hahn (2005) by using a window of variable size to gradually remove the non-terrain components, thus minimizing the low pass filtering effects on the terrain points. This gradual removal of non-terrain points by iterative resizing of the window improves the ability of the filter to preserve terrain features and object boundaries.

One of variations of morphological filters is the slope based filter. It operates on a premise that the likelihood of two nearby terrain points having a large height difference is minimal, while with increased separation between points the larger height difference becomes more probable (Vosselman, 2000). Instead of looking for a point with the lowest elevation in a predefined search area, a slope filter checks if there are any points below a given point through the use of a cone-shaped region search space. If no points are found under the cone, the point at the vertex of the cone is stored as a terrain point and the next point is checked. This type of algorithms takes into account the sloping characteristics of the terrain and thus is capable of preserving certain terrain features better than the regular morphological filters. However, slope filters contain more parameters and thus require more tuning for them to operate accurately (Sithole, 2001).

2.4.2 Iterative surface model filters

With the iterative surface model, the DTM is iteratively refined through the addition of the ground points at each iteration based on certain rules and thresholds. An example of such a filter can be found in Kraus and Pfeifer (1998), where the surface fitting interpolation is implemented based on a linear, least squares model. The weights for the points are re-estimated at each iteration by analyzing the residuals in order to arrive at the model that favours the low laying points. The drawback of this method lies on the fact that the object edges and sharp terrain features (i.e., cliffs) are often smoothed out.

Elmqvist (2002) described another type of iterative surface filter employing an “active shape model” which is a deformable model that is calculated using an “energy function”. The energy function defines the elasticity of the model and acts as a cost function to determine when the model no longer requires updating (i.e., when to stop the iteration process). The initial model is first attached beneath the terrain forming an envelope under the point cloud. The elasticity of the model then determines how far up into the point cloud the terrain will propagate attaching itself to the points in the scene which it suspects to be terrain points. The model is then updated iteratively by gradually adding the local minima points that minimize the energy function. The process is repeated until the energy function converges to a solution or the Z difference between consecutive iterations becomes less than a predefined threshold. The advantage of this method is that it allows for the preservation of sharp edges in the scene. To be effective however, it does require high density LiDAR data (10 points per metre) with a high percentage of points being terrain points.

2.4.3 Segmentation/Cluster based methods

Segmentation and cluster-based methods utilize the object’s geometric and radiometric properties to classify points as terrain or non-terrain. Classification of LiDAR points into object classes, such as: ground, vegetation, buildings, roads, etc., does not only help to identify terrain points but also adds substantial value to the dataset. The automation of this process in terms of minimization of user required input has been a topic of many works and publications.

Some of the classification algorithms take advantage of the full-waveform data extracted parameters (such as pulse width etc.). This additional information improves the accuracy of classification and thus improves the quality of the resulting DTM. Wagner et al. (2008) demonstrated how the classification of vegetation vs. terrain can improve DTM extraction using the full-waveform information through the removal of non-terrain points. The ability to remove points corresponding to vegetation translates into cleaner and more accurate terrain reconstruction from the remaining data.

Nonetheless, difficulties with classification are still present. It would be rare for even a well-developed algorithm to execute without a single misclassification. The pulse width was found to be of small assistance in discriminating between the vegetation and building classes (Mallet et al., 2009). It is difficult to distinguish between vegetation and urban structures based on amplitude and width alone (Wagner et al., 2008). This difficulty can be overcome in urban environments by slope surface response modelling.

In Chauve et al. (2007), an extracted parameter α (the sharpness of detected echo) was evaluated for its effectiveness in classification. Its derivation can be found in Equation 2.6. Chauve et al. (2007) used thresholds based on trained values to perform classification with parameter α to successfully differentiate between buildings, natural ground, and vegetative areas. Furthermore, α was proved to be less sensitive to radiometric changes than the other extracted waveform parameters. Chauve et al. (2007) suggested the use of α as a discriminative parameter when associated with other variables in a supervised classification.

In Mallet et al. (2008) an approach for classification using the combination of geometric and radiometric parameters was demonstrated for full-waveform LiDAR datasets. It made use of the difference between pulse range and lowest point nearby within a certain radius, residuals from a best fitted plane estimate, deviation of local normal vector from the vertical, altitude difference between first and last pulses, the number of echoes in the waveform, the amplitude, the width, and the shape of the waveform. These variables demonstrated their promising prospects for use in the classification of objects into the classes of building, vegetation, artificial ground and natural ground.

The current research trend appears to attempt to de-couple the properties of geometry and radiometry, through efforts of precisely separating the two effects one from the other. For this task, iterative methodology has the definite benefit of being able to model the surface and then re-estimate the waveform properties form the model and classify the surface response. This iterative approach allows for parameters such as cross-section to be corrected for target's geometry (angle of incidence etc.) and to be used for classification more effectively.

Overall, the combination of the full-waveform data and the neighbourhood analysis methodologies takes advantage of both types of the classification techniques (radiometric and geometric). This combination allows for the effective use of the available data in order to provide better, more stable and consistent classification results.

2.4.4 Progressive TIN methods

Described by Axelsson (2000), the progressive TIN is an iterative algorithm that builds up a DTM using a generated TIN model. A variation of the progressive TIN algorithm is deployed as a module in the TerraSolid's software: TerraScan. The progressive TIN algorithm is also the method that was chosen to perform initial DTM extraction in this research. In particular, the progressive TIN algorithm implemented in this study is a simplistic realization of TerraSolid's ground extraction tool and was developed based on Axselsson (2000) and the information extracted from TerraScan's User Guide (Soininen, 2010). The implementation is described in more detail in Section 5.2.1

The developed routine initially creates a TIN surface model by locating the lowest points within a search space, where the size of these regions is defined by the "Maximum Building Size" variable. This variable determines the size of an area where a single local low point will be chosen from. It is similar to the window or disc size in the morphological filter's erosion operation. From these low points, an initial TIN model is then constructed. During each iteration, the algorithm evaluates all the points against the TIN using the following threshold parameters: iteration angle, iteration distance, and terrain angle, all of which are supplied by the user. The iteration angle threshold is the maximum accepted value for an angle that is computed between the candidate terrain point, the closest vertex of the TIN and candidates point's projection onto the surface of

the TIN facet (angle is labelled θ in Figure 2.7). The iteration distance threshold is the maximum allowable distance (in magnitude) of the normal vector computed between the TIN facet to the candidate point (labelled *D* in Figure 2.7). The third and final threshold parameter used in this research is the terrain angle, which is the threshold for the slopes of the three new TIN facets that form as a result of the addition of the candidate point.

If a candidate point satisfies all three thresholds, it is accepted by the TIN model. Once all the points are evaluated, the new vertices are added to the TIN model. The algorithm runs until no new point is added to the model or until fewer points than a preset threshold are introduced into the model.

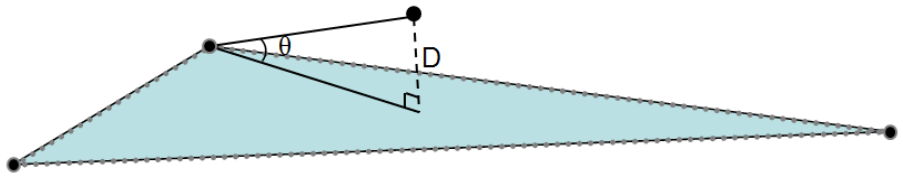

Figure.2.7 Progressive TIN parameters: θ - iteration angle and D – iteration distance

The progressive TIN algorithm itself does not differentiate between vegetation and non-vegetation points. Thus, an appropriate classification is required in order to avoid inclusion errors due to addition of low laying objects (tree trunks, shrubs, etc.) into the derived terrain model causing inaccuracies.

3 Full-waveform LiDAR data and ground reference data

In this Chapter the collected LiDAR data that was used in this study is introduced and the procedure for its direct geo-referencing is provided. Also included in this chapter is the procedure used for acquisition of the ground survey data, collected as a part of this research for validation of the developed algorithm.

3.1 Full-waveform LiDAR data

The full-waveform LiDAR data used in this study was acquired in August 2009 over an area near Sault Ste. Marie, Ontario, Canada (46°30′N, 83°25′W), with a Riegl LMS Q-560 scanner mounted on an aircraft with an Applanix' POS AV 310 system. The data were collected at the flight height of 150 - 300 m above the terrain by GeoDigital International (http://www.geodigital.com/). The terrain ranged in height from 220 to 410 m above mean sea level. The flight configuration produced a point density of about 20 points per square metre (4 pulses m^{-2}) with a nominal footprint of approximately 10-20 cm. Figure 3.1 provides an overview of the study sites which possess various natural and man-made objects such as trees of various species, dense vegetation, houses, etc. The detailed information on these study sites is listed in Table 3.1

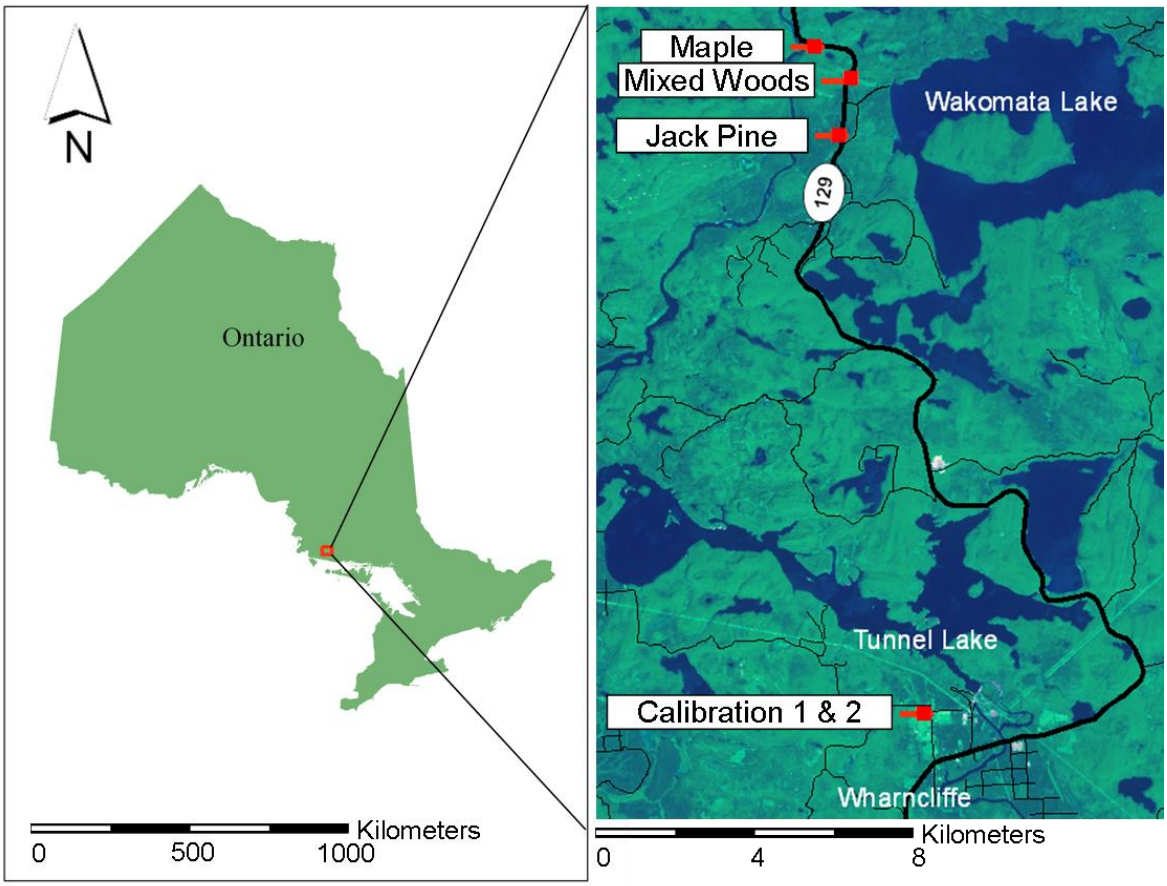

Figure 3.1 The study area with 5 study sites identified

Table 3.1 Characteristics of the selected study sites

Site	Terrain	Ground vegetation cover (density & species)
Calibration I	Flat with minimal terrain variation	Shrubs, predominantly spruce with some deciduous.
Calibration II	Flat	Grass and some shrubs
Maple	Gently rolling hill	Very dense cover, pure maple site
Mixed Wood	Steep hills	Mix of coniferous (jack pine) and deciduous, with shrubs, dense cover
Jack Pine	Gently rolling hill	Predominantly jack pine, dense cover

This LiDAR unit has two receiving sensors: one has high sensitivity (Hi) for recording weak return signals and the other has low sensitivity (Lo) for recording high strength return signals. The data from the Lo is recommended for use once the Hi sensor reaches a certain threshold at which the sensor over saturates and no longer accurately represents the signal strength. A single segment of the return is then created through the combination of the two channels (Hi and Lo) to avoid over saturation, and to retain the ability of the LiDAR to accurately record low amplitude returns.

The LMS-Q560 uses the rotating polygon scanning mechanism. It scans in lines as demonstrated in Figure 2.2 (a). The polygon has four sides, each of which is calibrated and has its own transformation parameters. These are used to calculate the coordinates of the return waveform in 3D with respect to the LiDAR reference frame.

The pulse emitted by the LMS-Q560 closely resembles a Gaussian function. A 2% discrepancy was reported in Wagner et al. (2008). Based on 1000 emitted pulses extracted from the data collected for this research, it was found that there was a 5% difference between the Gaussian model and the emitted pulse (Figure 3.2). This discrepancy is mainly due to the ringing effect, which will be described in detail in Section 4.3.

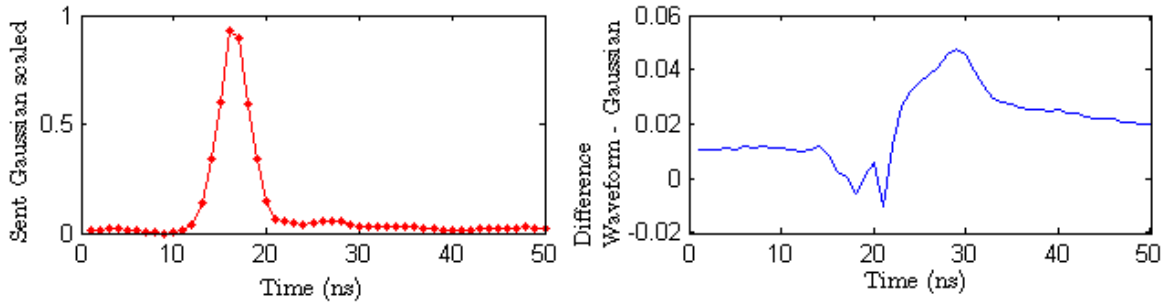

Figure 3.2 Left: the LMS-Q560 emitted waveform displayed in relative units. The plot on the right shows the deviations between the emitted pulse and a fitted Gaussian model.

3.2 Geo-referencing of LIDAR data

As mentioned in Chapter 2, for an airborne LiDAR system, the measured range from the LiDAR unit to a target is often converted to the required 3D coordinates in a real word coordinate system (referred as a mapping frame) through a series of coordinate transformation using the measurements from an on-board direct geo-referencing unit. The measured range is first converted to the 3D coordinates in the LiDAR sensor frame (s-frame), then to the coordinates in the POS reference frame (r-frame); and last to coordinates in the selected mapping frame. In the following, the implementation of the transformations carried out in this study will be described.

The first transformation implemented was to convert the range to the detected target and the angle between the laser beam and the scanner's mirror to the Cartesian coordinates, to produce an XYZ vector, in the LiDAR sensor frame (s-frame). This transformation was accomplished through the use of the precise mirror angles and a number of calibrated offsets for the mirrors and range. Equations for this transformation, as well as the

corrections to the raw waveform, are not covered here since these are proprietary properties of Riegl GmbH.

The conversion of the coordinates of a target point in the s-frame to the POS reference frame (r-frame) was achieved using the lever arm (ΔX, ΔY, ΔZ) and boresight angles (ω, θ, φ) between IMU and the LiDAR (Figure 3.3).

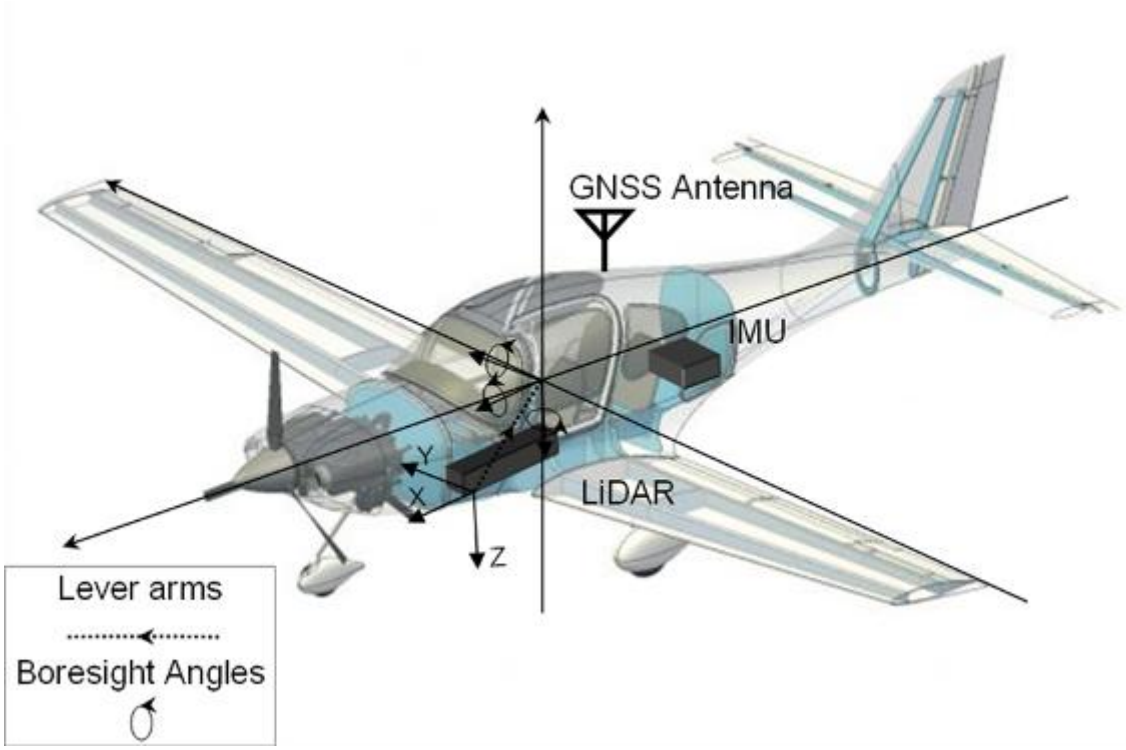

Figure 3.3 Sensor (LiDAR) reference frames to POS reference frame transformation, using lever arms and boresight angles

Mathematically, this conversion was accomplished by a 3D conformal transformation given in Equation 3.2.

$$\begin{bmatrix} X_{POS} \\ Y_{POS} \\ Z_{POS} \end{bmatrix} = Rot(-\omega,-\theta,-\varphi)\begin{bmatrix} X_{LiDAR} \\ Y_{LiDAR} \\ Z_{LiDAR} \end{bmatrix} + \begin{bmatrix} \Delta X \\ \Delta Y \\ \Delta Z \end{bmatrix} \tag{3.2}$$

$$Rot \quad (\omega,\theta,\varphi) = \begin{pmatrix} \cos(\theta)\cos(\varphi) & \sin(\varphi)\sin(\theta)\cos(\omega) - \cos(\varphi)\sin(\omega) & \cos(\omega)\sin(\theta)\cos(\varphi) + \sin(\omega)\sin(\varphi) \\ \cos(\theta)\sin(\varphi) & \sin(\varphi)\sin(\omega)\sin(\theta) + \cos(\omega)\cos(\varphi) & \sin(\varphi)\sin(\theta)\cos(\omega) - \cos(\varphi)\sin(\omega) \\ -\sin(\theta) & \cos(\theta)\sin(\varphi) & \cos(\omega)\cos(\varphi) \end{pmatrix}$$

The conversion of the coordinates of a target point in the r-frame to the mapping frame was performed by initially applying the roll, pitch and yaw angle rotations from the SBET solution to the r-frame coordinates In this intermediate step the Z-vertical was aligned with local gravity, (positive in the down direction), with Y pointing to geographical North, X pointing towards the East, and with the location of the origin remaining at the origin of the POS reference frame (Figure 3.4). Applying the angular rotations to the LiDAR data, already in the POS reference frame, using the Equation (3.3) aligns the LiDAR data with the mapping frame. The resulting transformation has essentially brought the LiDAR points into the local vertical North East Down (NED) frame.

$$\begin{bmatrix} N \\ E \\ D \end{bmatrix} = Rot(-\omega,-\theta,-\varphi)\begin{bmatrix} X_{POS} \\ Y_{POS} \\ Z_{POS} \end{bmatrix} \tag{3.3}$$

wherein Roll= -ω, Pitch = -θ, Yaw = -φ, are the rotations applied to the coordinates in the reference frame to obtain the coordinates in the NED local vertical frame. *NOTE:* POS data frequency as used was 200 Hz, thus in order to obtain position and orientation at the required time, data between two consecutive POS data points were linearly interpolated.

The next step was to then transform the rotated coordinates from the local NED frame using the post processed SBET coordinates to the mapping reference frame.

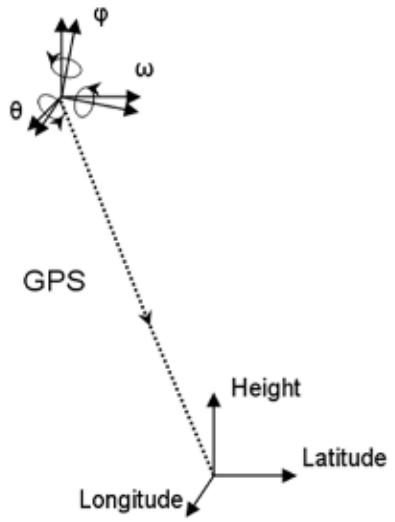

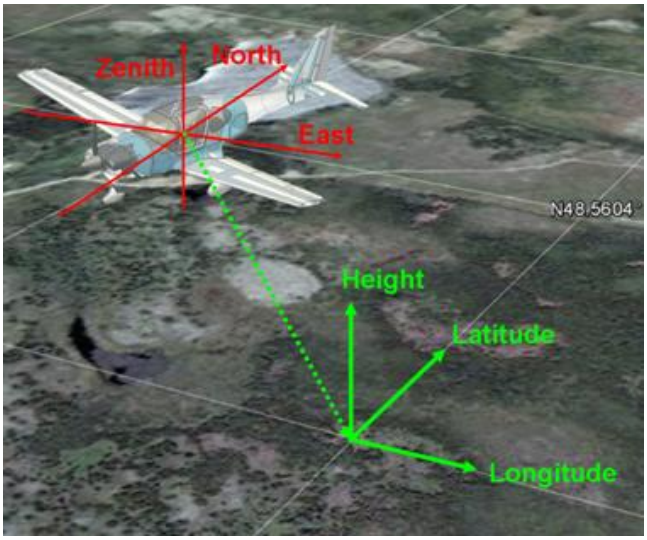

Figure 3.4 The geometry related to the coordinate transformation from the reference frame and the mapping frame.

The SBET coordinates given in WGS84 curvilinear frame were then converted to Cartesian ECEF frame using Equations 3.4 and 3.5. This conversion was performed as the ECEF coordinates were more easily combined with the local vertical coordinates then the geodetic.

$$\begin{aligned} X &= (N+h)\cos\phi\cos\lambda \\ Y &= (N+h)\cos\phi\sin\lambda \\ Z &= (N(1-e^2)+h)\cos\phi \end{aligned} \tag{3.4}$$

$$N = \frac{a}{\sqrt{1-e^2\sin^2\phi}} \tag{3.5}$$

wherein N is the radius of curvature and is measured from the surface of ellipsoid to the Z-axis along the ellipsoid normal, "*a*" is the semi major axis, and "*e*" is the eccentricity of the reference ellipsoid.

With the help of the rotation matrix *M*, the transformation from the local vertical to the geocentric was preformed, via Equation 3.6.

$$M = \begin{bmatrix} 1 & 0 & 0 \\ 0 & \sin\phi & \cos\phi \\ 0 & -\cos\phi & \sin\phi \end{bmatrix} \begin{bmatrix} -\sin\lambda & \cos\lambda & 0 \\ -\cos\lambda & -\sin\lambda & 0 \\ 0 & 0 & 1 \end{bmatrix} \tag{3.6}$$

wherein λ and Φ are the latitude and longitude from the post processed SBET solution, interpolated to sync to the LiDAR data.

$$\begin{bmatrix} X_{ECEF} \\ Y_{ECEF} \\ Z_{ECEF} \end{bmatrix} = M^T \begin{bmatrix} N \\ E \\ U \end{bmatrix} + \begin{bmatrix} X_{0\,ECEF} \\ Y_{0\,ECEF} \\ Z_{0\,ECEF} \end{bmatrix} \tag{3.7}$$

Equation 3.7 could be expanded by inserting the expressions for *M*, *N*, *E*, and *U*, as shown in Equations 3.8 and 3.9.

$$\begin{bmatrix} X_{ECEF} \\ Y_{ECEF} \\ Z_{ECEF} \end{bmatrix} = \left(\begin{bmatrix} 1 & 0 & 0 \\ 0 & \sin\phi & \cos\phi \\ 0 & -\cos\phi & \sin\phi \end{bmatrix} \begin{bmatrix} -\sin\lambda & \cos\lambda & 0 \\ -\cos\lambda & -\sin\lambda & 0 \\ 0 & 0 & 1 \end{bmatrix} \right)^{T} \begin{bmatrix} N \\ E \\ U \end{bmatrix} + \begin{bmatrix} X_{0\,ECEF} \\ Y_{0\,ECEF} \\ Z_{0\,ECEF} \end{bmatrix} \tag{3.8}$$

$$\begin{bmatrix} X_{ECEF} \\ Y_{ECEF} \\ Z_{ECEF} \end{bmatrix} = \left(\begin{bmatrix} 1 & 0 & 0 \\ 0 & \sin\phi & \cos\phi \\ 0 & -\cos\phi & \sin\phi \end{bmatrix} \begin{bmatrix} -\sin\lambda & \cos\lambda & 0 \\ -\cos\lambda & -\sin\lambda & 0 \\ 0 & 0 & 1 \end{bmatrix} \right)^{T} \left(Rot(-\omega,-\theta,\varphi) \begin{bmatrix} X_{POS} \\ Y_{POS} \\ Z_{POS} \end{bmatrix} \right) + \begin{bmatrix} X_{0\,ECEF} \\ Y_{0\,ECEF} \\ Z_{0\,ECEF} \end{bmatrix} \tag{3.9}$$

3.3 The collection and processing of ground reference data

To validate the developed method, ground surveys on the five study sites (Figure 3.1) were conducted in August and October 2011. The terrain models generated from the ground surveys were used as ground references in this study.

To collect accurate surveying data, a geodetic network was established in order to connect each study site to a global frame of reference. Each study site was surveyed using relative static GPS positioning techniques and total station equipment. In the following section, I briefly discuss the created geodetic network composed of GPS baselines, and the local networks (local traverses) that were established using the total station equipment for the purpose of collection of the topographic data at each study site. The details of the data acquisition can be found in Appendix B.

To set up a geodetic network, the documented horizontal control points from the Ministry of Natural Resources in the area of the survey were extracted from the COSINE database (www.**cosine**.mnr.gov.on.ca/, coordinate report is provided in Appendix D). Unfortunately, there were only two control points available, one for the northern study sites (station – 00820000478), and the other for the southern sites (station – 00819950063). Coincidently, the southern control station was also occupied with a GPS receiver during the 2009 LiDAR campaign as one of the base stations for post-processing of the POS data.

To connect the control points to the pre-selected study sites, a network composed of GPS baselines was established, as shown in Figure 3.5. Upon arrival at each of the preselected study sites, two GPS stations were setup 30 metres apart ("GPS1" and "GPS2") with the wooden steaks hammered into the ground as their marks (in order to establish a permanent point for the network station). The GPS receivers were run simultaneously to log the measurements for duration of at least half an hour for this short baseline.

Both of the GPS1 and GPS2 stations were then connected to the nearest available geodetic control point. Two occupations of each baseline (GPS1 to control and GPS2 to control), under different satellite configuration were performed for each GPS point pair, that resulted in a total of four observations. The double run manner of the GPS baseline data acquisition was introduced to provide with redundant observations to check for any significant errors made in the GPS baseline observations.

The GPS baseline network was finalized once all stations on the individual sites were connected to the nearby control points (Figure 3.5). The collected data was then processed and analyzed using Leica Geo Office and Columbus Best-Fit computing. The least square solution obtained can be found in Appendix C.

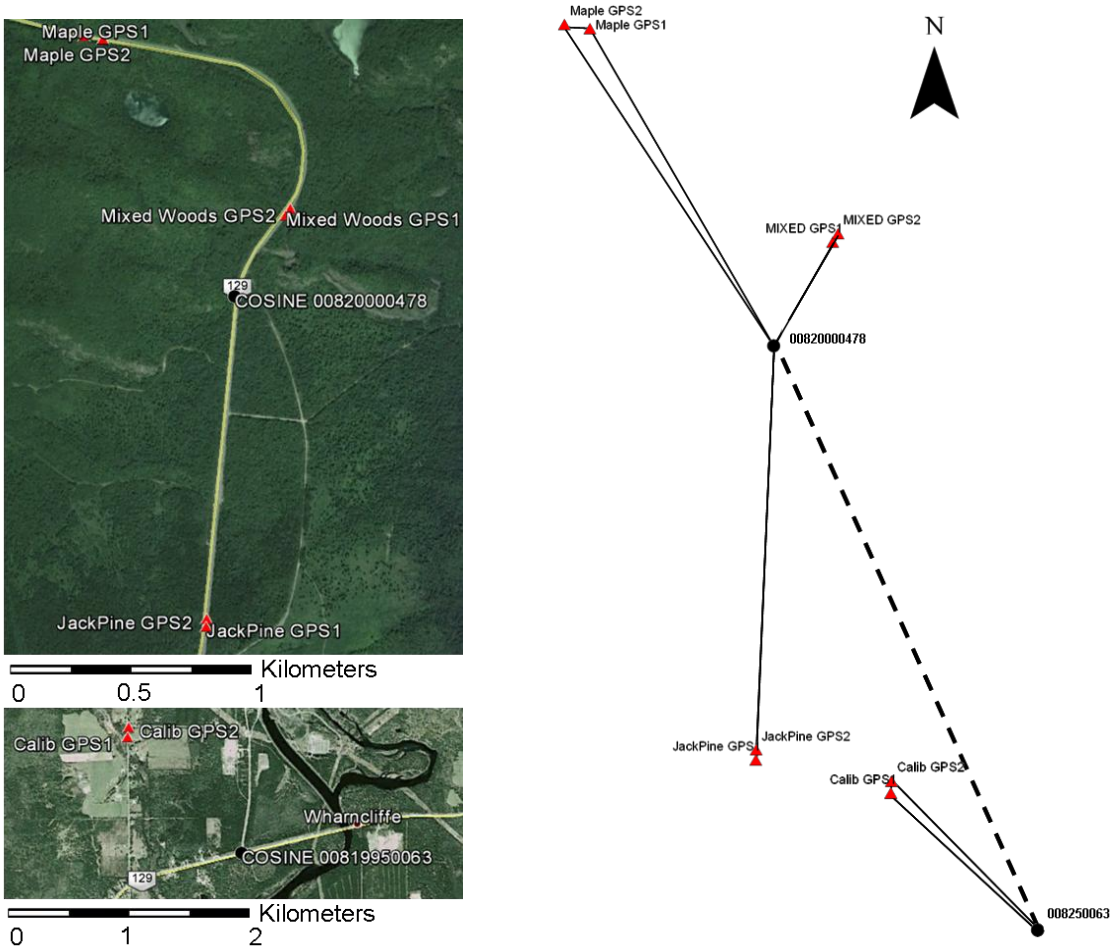

Figure 3.5 The established GNSS network. On the left is the overview map of the established points (red triangles) and control points (black circles). On the right is the diagram of the baseline measurements performed with the GNSS receivers where the segmented line is the baseline measurement between the control points, drawn not to scale in order for both control points to fit onto the plot.

After the GPS survey was completed, the total station equipment was used to establish a local traverse at each site. The first entrance point into the forest (point "A" on the edge of the tree line) was setup in a way that provided an unobstructed line of sight going into the forest and towards the study area (location of point "B") with both GPS network points also clearly visible. This setup allowed for the local traverse to be easily tied into the existing GPS network.

Depending on how far into the forest the study site was, a number of intermediate traverse points were set up to reach the plot center. The traverse points were positioned in a manner that would keep the number of total station setups to minimum whilst maintaining an unobstructed line of site between consecutive setups. The traverse points were located as far away from trees as possible in order to obtain the best view of the study plot area. The visual representation of all the sites and their corresponding traverse networks can be found in Appendix B.

To conduct the topographic survey (ground point collection), two local traverse points were used; one occupied by a reflector (to act as backsight) and the other occupied by the total station. The plot boundaries were defined using rope, which helped to navigate under the canopy and ensured systematic linear collection of the topographic points line by line across the plot, hence, providing an even distribution of terrain points. The use of small flags to mark the locations of surveyed points also greatly assisted with the data acquisition process. A group of 20 topographic points were collected at a time, and the backsight direction was checked before and after each group collection. The sharp tip of

the survey pole was rested on top of the foliage, and never forced into the ground in an attempt to obtain consistent point measurements. A summary of the total number of topographic points collected at each study site is provided in Table 3.2.

Together with the topographic points, additional check points were also collected at each of the sites for the purpose of LiDAR data validation. The description of the check points is given in Appendix F, and the result of the data acquisition campaign together with more detailed information on procedures and analysis used can be found in Appendices B through E.

Table 3.2 Topo points collected at each site

Site	Number of topo points
Calibration 1	180
Calibration 2	300
Maple	400
Mixed	250
Jack Pine	300

3.4 The assessment of ground reference data

The accuracy assessment of the ground reference data collected was carried out using error propagation techniques. The results of this assessment are summarized in Table 3.3.

To estimate the error of the ground reference data, both accuracies of the established network (traverse) and the topographic point collection had to be considered. For the latter, the survey equipment specifications were used to estimate the associated errors. The measurement uncertainties with a SOKKIA Set510 provided in the user manual were

±5” for angle and ± (2mm + 2ppm) for distance. Equation 3.10 was used to calculate the 3D accuracy of a point measured by a total station.

$$\sigma_{point}^2 = \sigma_S^2 + S^2 \frac{\sigma_\psi^2}{\rho''^2} + S_t{}^2 \cos\psi^2 \frac{\sigma_\xi^2}{\rho''^2} \tag{3.10}$$

wherein:

S is the distance measurement,

ξ is the horizontal angle measurement,

ψ is the vertical angle measurement,

σ is the associated errors of these parameters, and

ρ is the convertor from radians to seconds: 206264.8.

The maximum distance of 50 metres was observed, and for simplicity, vertical and horizontal angles of 0˚ were substituted into Equation 3.11, which yielded the following equation.

$$\sigma_{point}^2 = (0.002 + 50 \times \frac{2}{1000000})^2 + 50^2 \frac{5_\theta^2}{\rho''^2} + 50^2 \frac{5_\psi^2}{\rho''^2} \tag{3.11}$$

σ_{point}=±3.5 mm or ±0.7 cm at 2σ. With the components: ±0.67 cm error in horizontal and ±0.22 cm in vertical.

This calculated value was rather optimistic as it should be noted that the hand held survey pole was used to collect the topographic data. An additional error effect of 1 cm should be added to the horizontal component due to difficulties in levelling and poor visibility in

the dense brush. Also, due to the amount of foliage on the ground an error of up to 2 cm in the vertical direction for the measured points should be accounted for. Hence, the reasonable accuracy of the topographic points was assumed to be closer to ±1.67 cm in horizontal and ±2.2 cm in vertical in the densely forested areas.

The positional accuracy of the GPS network stations and the established traverse points were also included in topographic point position accuracy estimation. From the analysis of the GPS observations, the uncertainty of the derived GPS network point coordinates was estimated to be around ±1.83cm horizontal and ±1.50 cm vertical (Appendix C). After propagating the GPS network point error to the traverse points, the plot centre traverse point accuracies were estimated to be ±3.0 cm in horizontal direction and ±2.50 cm in vertical. Combining the positional accuracy of plot centre point with the topographic point acquisition accuracies meant that the ground topographic mapping data was expected to have accuracies of ±4.67 cm horizontal, ±4.72 cm vertical - in heavily wooded areas and ±3.67 cm horizontal, ±2.72 cm vertical - in open areas.

Table 3.3 Estimated Accuracy of the Topo Data

Conditions	Horizontal Accuracy 2σ (cm)	Vertical accuracy 2σ (cm)
GPS derived points	1.83	1.50
Plot center, traverse point	3.00	2.50
Topo points in wooded area	4.67	4.72
Topo points open area	3.67	2.72

From Table 3.3 and the LiDAR platform error estimation described in Section 6.1, it is clear that the accuracy of the ground reference data is superior to that of the LiDAR point cloud. Hence, the collected topographic data can be used to validate the proposed DTM extraction algorithm.

To assess the compatibility of the LiDAR derived point cloud data and the ground reference data, additional objects located in the vicinity of the study sites were collected during the ground survey data acquisition and were used as check points between the two datasets in the validation stage. A detailed description of these objects can be found in Appendix F. The check points mainly consisted of the lane markings on the roads that would be visible on a LiDAR point cloud intensity plots, as well as a number of road signs, utility poles, drainage pipes and vegetation free slopes, etc. Also, the Calibration II study site (open grass covered area) was used as a vertical control to check the agreement of the elevation values between the data collected by LiDAR and data surveyed with GPS and total station.

During the time between the airborne LiDAR survey and the ground reference data acquisition, highway 129 was resurfaced. All tie-ins with the road were lost. However, a few of the targets chosen as the check points were still present at the sites so that there were a sufficient number of check points to provide the necessary information on the compatibility of the two datasets.

The comparative results between the ground reference points and the LiDAR datasets indicated the horizontal position offsets ranging from 5 to 20 cm with no distinct patterns in direction of the error observed. The vertical offset (as expected) was systematic at each site and varied from 2 cm at site Calibration II to 6 cm at Maple site. These vertical offsets could be due to the difference in processing technique employed for the LiDAR geo-referencing and ground survey data processing.

The comparative results between the two datasets matched the expectation of the absolute accuracy for the platform used for the LiDAR data acquisition campaign. The accuracy of the ground reference data and the LiDAR data collected appear to be within the established limits. Thus, it can be inferred that the ground reference data can be used for the validation of the developed DTM extraction algorithm.

4 Implementation of Gaussian decomposition methods

Even though Gaussian decomposition methods were well-described in the literature, their implementation was not trivial. In this chapter, my implementation of Gaussian decomposition methods is described. I also implemented a method for the detection of the ringing pulses (described in Section 2) which is described in the following as well.

4.1 A general overview

The Gaussian decomposition (Hofton et al., 2000; Wagner et al., 2006; and Lin et al, 2010) is the most commonly used method to decompose the recorded full-waveform into several discrete echoes (equation 4.1):

$$f(t) = \sum_{i=1}^{N} A_i \exp\left(-\frac{(t-\mu_i)^2}{2\sigma_i^2}\right) \tag{4.1}$$

wherein N is the number of the Gaussian functions used to fit the recorded signal, A_i is the magnitude of the i^{th} Gaussian function (echo); and μ_i, and σ_i are its central position and echo width, respectively. N is commonly determined prior to the decomposition, while the variables A_i, μ_i and σ_i *(i=1,2..N)* are solved by minimizing the cost function (Equation 4.2) using LM optimization method (Jutzi and Stilla 2005; Chauve et al. 2007), which is available in GSL (GNU Scientific Library):

$$\varepsilon = \sum_{j=1}^{M} \left(X_j - f_j\right)^2 \tag{4.2}$$

wherein M is the number of the samples in the recorded echo; and X_j and f_j are the magnitudes calculated by Equation 4.1 at each sample point j.

4.2 Implementation of Gaussian decomposition

The key to the Gaussian decomposition is to accurately determine the number of returns and the initial value of the parameters (position, width, and magnitude) associated with each return. This initialization process requires separating the signal from background noise. A pulse with its amplitude below a certain threshold (T) might be indistinguishable or could have a detrimental effect on the overall quality of the extracted data if it is fitted. In this study, the amplitude threshold (T) for potential returns was determined experimentally, any returns with amplitudes smaller than T were not considered. In Stilla and Jutzi (2008) and Lin et al., (2010), the threshold was set as three times the standard deviation of random noise ($3\sigma_n$). The value for T in this research was calculated based on the mean and the standard deviation of the noise observed from the records of the emitted pulse. Accordingly, two different tests were carried out where 15,000 emitted waveforms were used for the computation of noise. For the first test, the amplitudes of all the recorded samples before and after the emitted pulse where evaluated (Figure 4.1, left). The mean value of the samples was found to be 3.5 and a 3σ standard deviation of 5.4 was observed. The second test was performed using only a region of the waveform near the emitted pulse (20 samples before and after the system generated pulse). This test yielded a mean value of 5 and standard deviation of 10 at 3σ (Figure 4.1, right).

Based on the experiments, T was estimated to be 8 and 15 from the two tests, respectively. It is worth noting that threshold value is usually chosen to be higher so as to avoid the effect of noise. However, a bigger T value may also result in missing some of the weak echoes. Nonetheless, this is not an issue for the algorithm proposed by this research, since the weak echoes generated by terrain under vegetation canopies are detected in the subsequent steps.

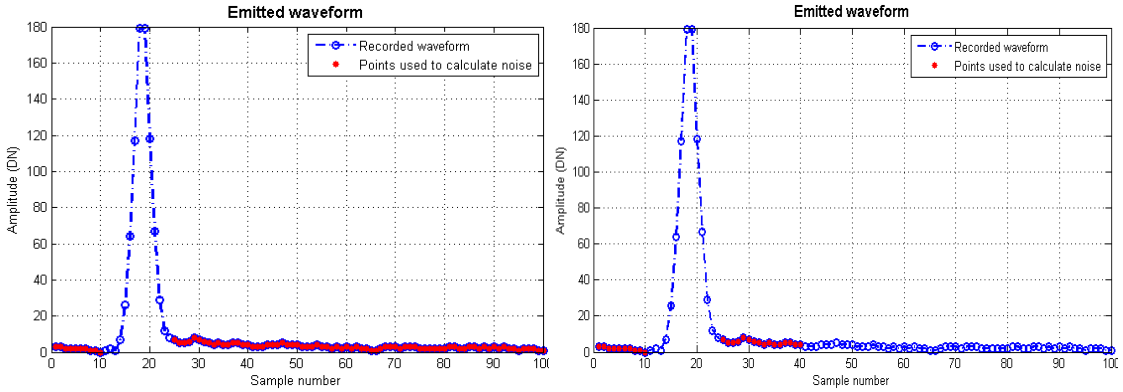

Figure 4.1 Left plot shows the waveform data (in red) used for noise calculation in Test 1 where all the samples not belonging to the identified pulse are used for noise estimation. Right plot shows the data points (in red) used for Test 2 where only the 20 samples before and after an identified pulse are used to calculate the systems' background noise.

The workflow of the implemented Gaussian decomposition algorithm is outlined in Figure 4.2. In order to initialize the LM algorithm for Gaussian fitting, the locations of the pulses were detected using a strategy described in this section, and named "initialization" (#1 in Figure 4.2). The results obtained from the LM algorithm (#2 in Figure 4.2) were then tested using a "condition check" (#3 in Figure 4.2). If the conditions were not met, the pulse locations were re-estimated (#4 in Figure 4.2). If the

conditions were satisfied, the resulting targets extracted through this algorithm were further tested for the presence of "ringing pulses" (Section 4.3).

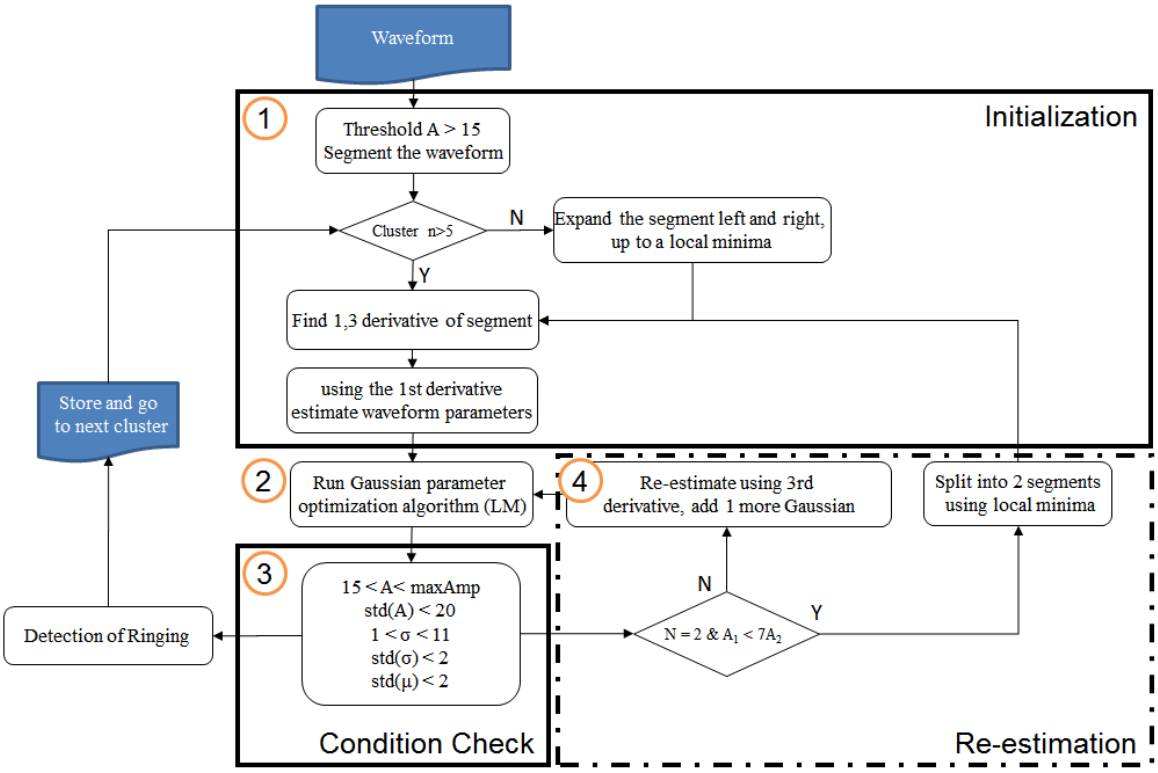

Figure 4.2 The workflow of the implemented Gaussian decomposition method.

As in the example shown in Figure 4.3, the first step of "Initialization" was to segment the continuous waveform into clusters. Each cluster was composed of points (samples) with amplitudes above the threshold value *T*, which was set as 15 in this study (Figure 4.4).

Generally speaking, it requires at least five points for the fitting of a waveform. In case where there are fewer than five samples in a given cluster, the points on either side of the grouping that are below the preset threshold *T* can be included into the cluster.

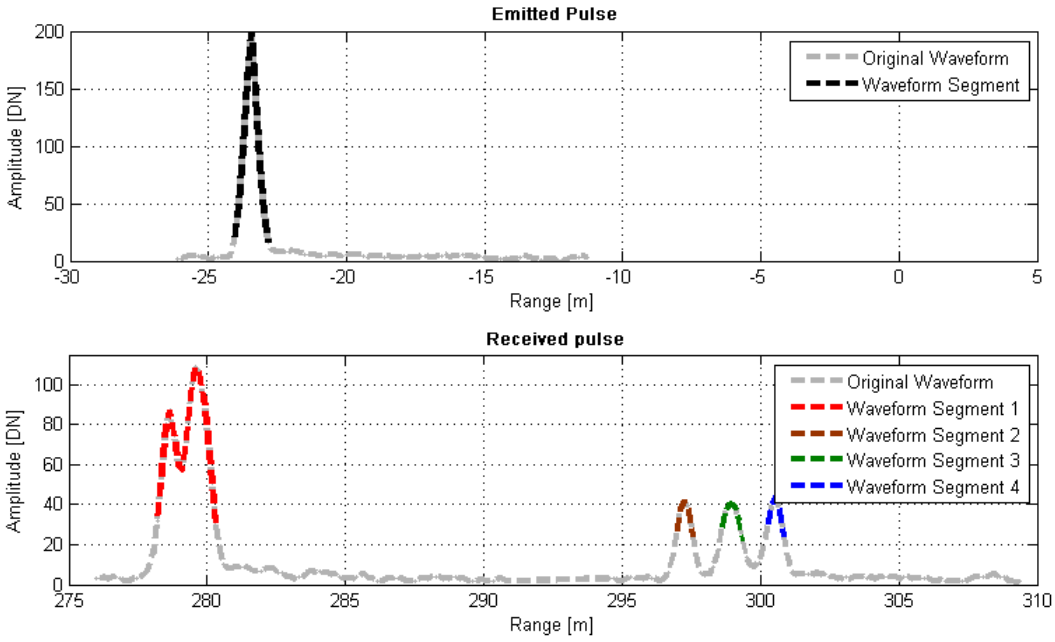

Figure 4.3 Segments generated and used (highlighted)

After the waveform was split into segments, the first, second, and third derivatives with respect to amplitude of the segments were computed (Figure 4.4). The zero crossings of first and third derivatives were used to locate the local maxima and points of inflection of the waveform respectively, which corresponded to the location of the targets, and were needed for the initialization of the LM algorithm.

For the waveform returns with well pronounced peaks where the distance between targets is sufficient enough to avoid any overlapping of pulses (Figure 4.4), only the first derivative was used for pulse detection to initialize LM algorithm (step 2 in Figure 4.2).

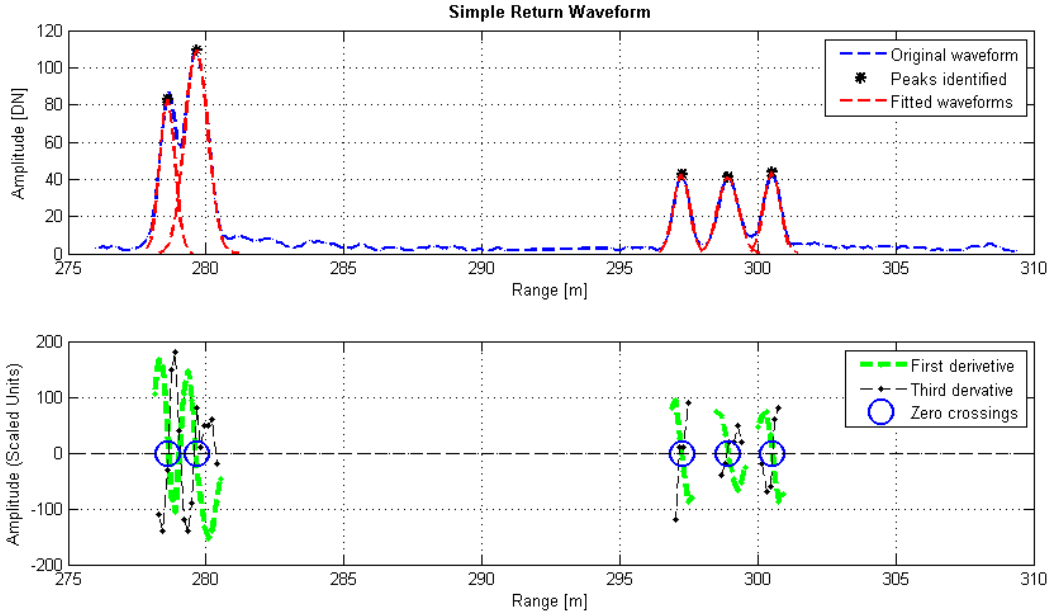

Figure 4.4 Example of a simple case of Gaussian fitting, where the pulses are easily defined and are distinguishable (top). In this type of cases, using the local minima (zero crossing of first derivative) is sufficient to pick out the individual returns (bottom)

Unfortunately, the situation depicted in Figure 4.4 was rare, especially so in the wooded areas where multiple returns from nearby objects (distance < pulse width) became virtually indistinguishable (see Figure 4.5 below). The procedures outlined in steps 3 and 4 of Figure 4.2 were implemented to deal with these complex cases through the use of the third derivative.

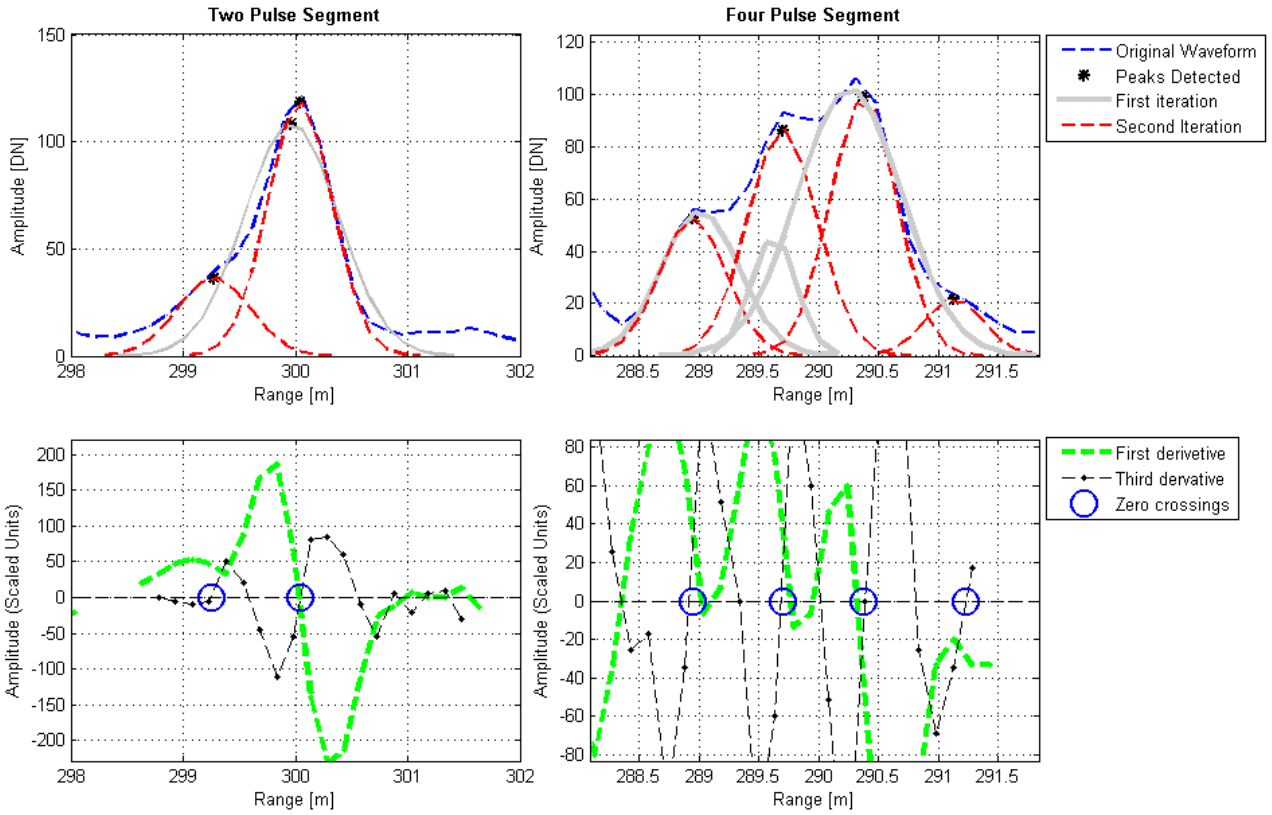

Figure 4.5 Example of a complex case of Gaussian fitting (top), where the third derivative of the waveform had to be used to successfully seed the waveforms (bottom).

Figure 4.6 demonstrates how the first and the third derivatives could be used to distinguish returns from the signature, if the pulses were overlapping. The first derivative was analyzed for the locations of zero crossing in the negative direction, as these were representative of local maxima points and provided an initial estimate of the number of waveforms. The third derivative was analyzed for the zero crossings in the positive direction, which corresponded to the points of inflection and provided the possible location of additional returns that might not be picked up by the first derivative. The

amplitude (A) and the time (μ) of the waveform corresponding to the location of the zero crossings were used to initialize the LM algorithm. The width of the emitted pulse (σ) was used as the approximation of the width of the return pulses to be fitted.

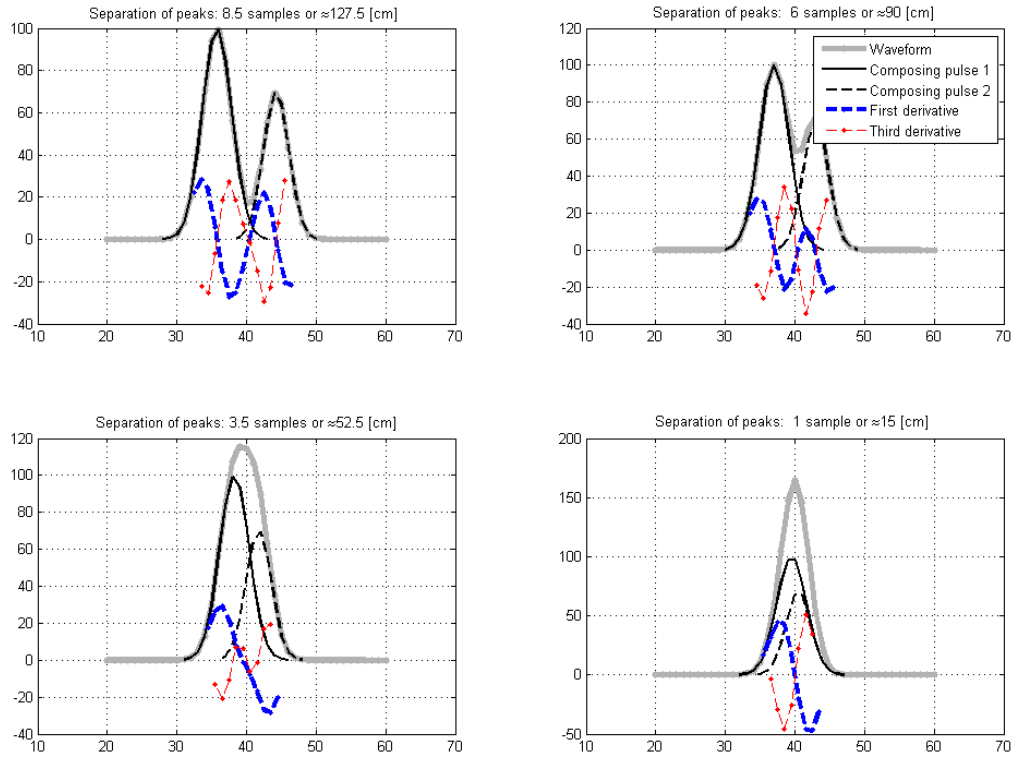

Figure 4.6 A demonstration of how the distance between the consecutive pulses affected the chances to distinguish the two individual returns on analysis (simulated data)

For the complex cases where the use of the third derivative was required, the initial pulse detection was still performed using only the first derivative zero crossings to initialize the LM algorithm. The parameters of the Gaussian functions obtained from the LM fitting were then checked to ensure that certain conditions were met ("Condition check" in

Figure 4.2). If the condition check failed, the third derivative of the waveform would be used for the re-evaluation of the location of the return pulses.

The parameters of the Gaussian functions obtained from the initial round of LM fitting were checked to see if the following conditions were met (#3 in Figure 4.2):

- The amplitude of a Gaussian function is bigger than 15 and less than 1.1 times the corresponding amplitude value of the original waveform, while all the estimated amplitude errors are less than 20 units.
- The width is less than 8 ns and more than 1 ns with an associated error of less than 2 units.
- The mean value is in an acceptable range (range of the waveform) with an associated error of less than 1 ns (15 cm).
- The fitted Gaussian curves are separated by more than 2 ns (30 cm).

It is worth mentioning that the analysis of the Chi-Squared value obtained from the LM algorithm demonstrated that this parameter might not be a good indicator for goodness of fit as it often indicated that the results were acceptable even when the condition check on the estimated parameters failed. For this reason the Chi-Squared value was not used to check the validity of the fitted waveform.

If any of the specific conditions was not met, the following steps were further taken (#4, “re-estimation” in Figure 4.2).

1) Check if the segment was initially fitted with only two pulses whose amplitudes had a ratio of 7:1 or higher. This check was done because it was found that the higher amplitude returns were often not a good fit for the regular Gaussian model causing an error in the fitting of the trailing smaller pulse (Figure 4.7). The solution to the erroneous fit was to split the segment into two parts (based on local minima) and re-process each resulting sub-segment separately.

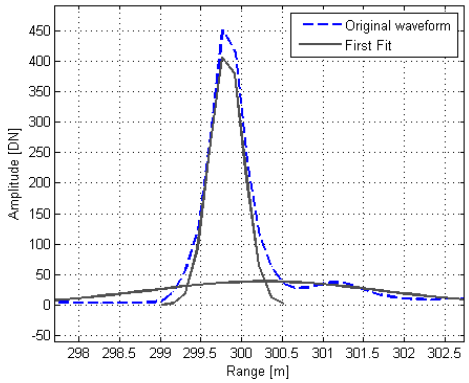

Figure 4.7 An example of a case where fitting the return waveform (blue dashed line) with two Gaussian curves (black solid lines) results in an erroneous fit. It can be seen that the second, lower amplitude pulse that has been fitted does not follow the initial waveform.

2) In all the other cases (examples given in Figure 4.5), the third derivative was analyzed, and the negative direction zero crossings were used to identify potential additional returns. A new candidate, based on third derivative zero crossing with the steepest slope was chosen as a seed for an additional pulse. The reason for this selection was that the third derivative was susceptible to noise, and thus the most likely candidate pulses were the ones with the steepest slope. At this stage the LM algorithm was then re-run using the newly selected seed.

Once the results from the Gaussian fitting were obtained, they were then analysed for the ringing effect. This procedure is described in detail in Section 4.3.

4.3 Detection of ringing

The ringing effect is an important phenomenon to be analyzed when one performs a Gaussian decomposition (Roncat et al., 2008). This phenomenon causes the appearance of false weak pulses in the full-waveform signature that generally trail a strong return (high amplitude). The ringing effect is caused by LiDAR's receiver electronics, specifically the saturation of the photo diode used for signal amplification which may make it output phantom pulses (Magruder and Neuenschwander, 2009). When these phantom (i.e., ringing) pulses are fitted with a Gaussian curve and geo-referenced, they often become points that are located visibly below the level of the terrain. These points are clear outliers compared with both the surrounding returns and the terrain data obtained during ground survey. A demonstration of the effect of ringing pulses on the generated DTM is shown in Figure 4.8. It is important, as a result, to detect and eliminate the echoes caused by the ringing effect. In this research, after the LiDAR data were initially processed, a number of pulses (from bare ground areas) were analyzed in order to extract the thresholds and parameters to be used for the identification of false returns. Two distinct patterns, in which "ringing" occurs were then identified. A workflow was then developed to enable identification of the two types of ringing pulses and this workflow is outlined in Figure 4.9 and will further be discussed in the subsequent paragraphs. These ringing pulses could be treated with a filtering algorithm designed

specifically for the pulses below the surface. However it was more practical to implement a conditional check to catch these occurrences.

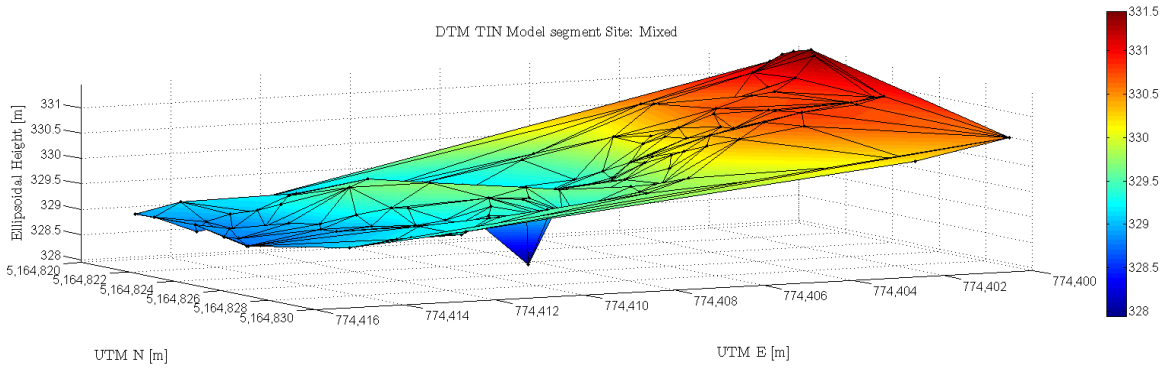

Figure 4.8 A demonstration of an outlier spike (dark blue) generated by an unhandled Type 2 "ringing" pulse

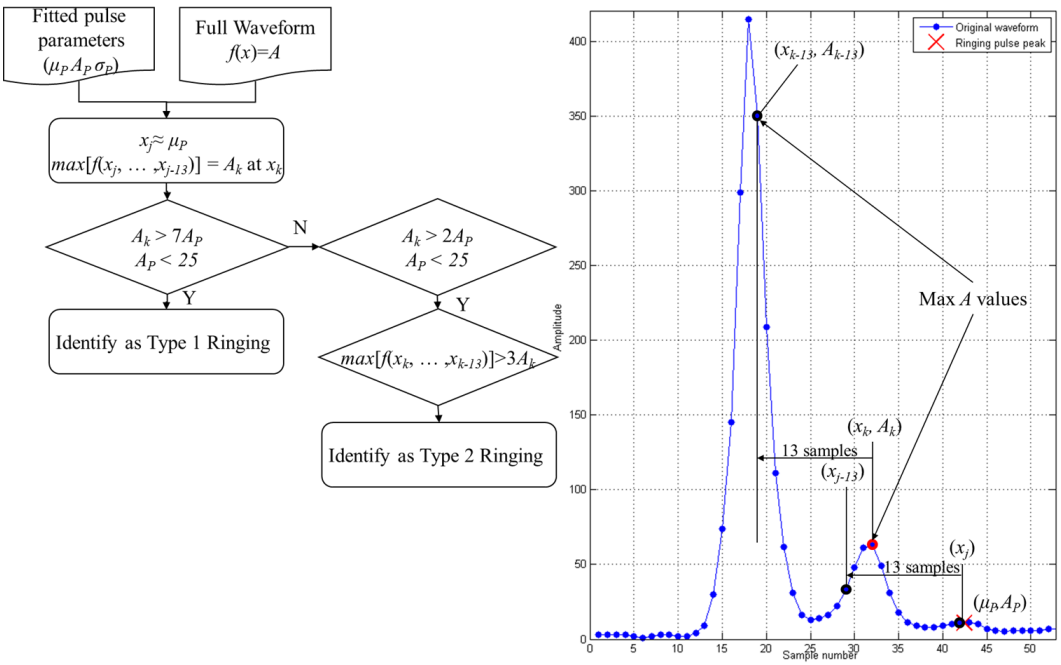

Figure 4.9 Flowchart and explanatory plot describing the workflow implemented for identification of the suspected Type 1 and Type 2 ringing pulses. Wherein μ_P and A_P are the peak location and the amplitude of the fitted pulse tested for ringing, $f(x)=A$ is the waveform from which the pulse was extracted from (where each sample x maps to an amplitude A). x_j is the sample closest to the detected

peak, and (x_k , A_k) is the location and magnitude of the maximum amplitude value within 13 samples of the fitted waveform.

As shown in Figure 4.10, the first type of ringing pulses, henceforth denoted as Type 1, often occurs after strong returns and Type 1 ringing pulses trailed a strong return within a certain distance. In case of this research, this distance was determined experimentally to be 13 samples. As a rule, the Type 1 ringing pulses were a fraction of the amplitude of the initial pulse (1:7 or less) and the amplitude of these phantom pulses was found to be below the 25 units mark.

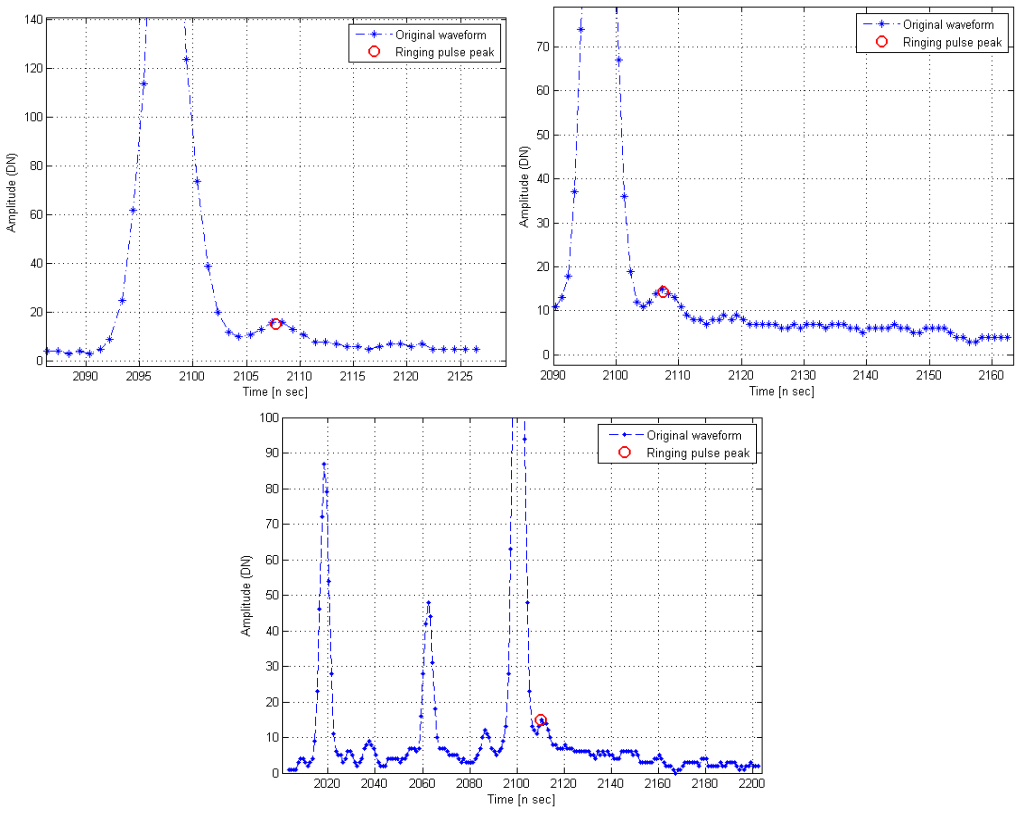

Figure 4.10 Examples of Type 1 ringing pulses (red circles).

As shown in Figure 4.11, the second type of ringing (denoted as Type 2) were the phantom pulses following two actual returned pulses. The two initial/actual consecutive

pulses had a separation of approximately 13 samples, similarly in patterns as that found in the case of Type 1 actual and ringing pulses. However due to their amplitude ratios, the first two pulses did not fall under the Type 1 ringing rule and neither did the second and third pulse. The Type 2 ringing pulses were found to be rare and occurred about once every 20,000 waveforms. If they were left unhandled, they would introduce errors into the DTM (Figure 4.8).

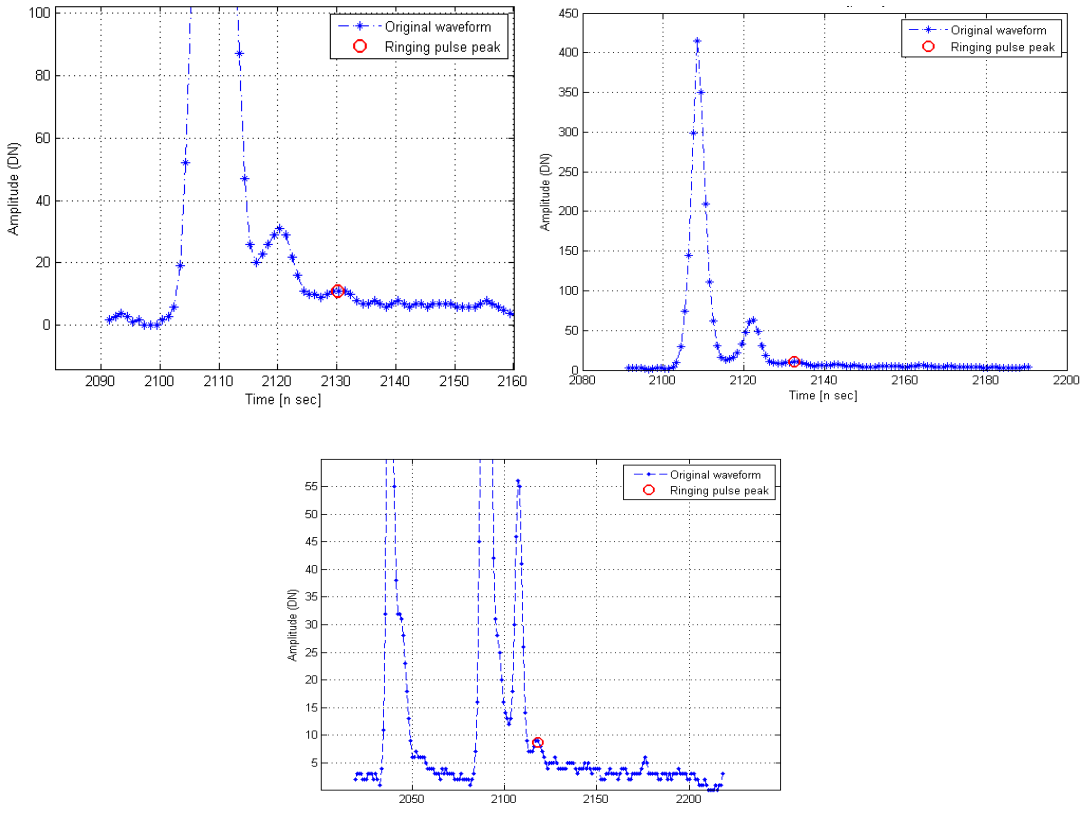

Figure 4.11 Examples of Type 2 ringing pulses (red circles).

To test for the Type 2 ringing pulses, the logic outlined in the flow chart (Figure 4.9) was used. If the check for Type 1 ringing pulses failed on the first two pulses based on their amplitudes (ratio of the amplitudes fell between 1:7 to 1:2), the third pulse would be

flagged as a Type 2 ringing pulse if it was less than 25 in amplitude, it fell within 13 samples of the second pulse and was smaller than 1/3 of amplitude of the second pulse. In other words, a candidate point was classified as a Type 2 ringing pulse if the candidate pulse was smaller than 25 in amplitude and located within 13 samples of another pulse that was three or more times the amplitude of the candidate pulse, and this neighboring pulse itself had a third sharp return pulse within 13 samples before it (300+ in amplitude).

For the implemented ringing detection method, experimental results demonstrated that the commission (Type I) error composed a high percentage of the detected ringing pulses (50-60%); the omission (Type II) error was minimal (a singular case was observed with approximately 500,000 evaluated waveforms). The reason for allowing large type I error was as follows. The inclusion of any ringing echoes in the DTM generation could cause significant errors, which has been demonstrated by Figure 4.8 the errors introduced by including ruining echoes. However, based on my experiments, the additional terrain pulses gained by reducing type II errors did not significantly affect the overall DTM quality. Thus it was determined that it was critical to keep the Type II error to the minimal, even if that meant an increased Type I error.

5 Integrated approach to DTM extraction

5.1 Outline

The method proposed in this research was an incorporation of the pulse detection of full-waveform LiDAR data and the DTM extraction, in which the weak pulse waveform extraction was performed at the same time as the DTM generation was progressed. The workflow of the proposed method is given in Figure 5.1. The input was the pre-processed waveforms as described in Chapter 3. The first step in the workflow was the Gaussian decomposition, which is described in detail in Chapter 4. The candidates for the terrain points were identified from the resulting points (the detected pulses), where only the last return points that met pre-set amplitude and width thresholds were selected. The candidate terrain points were then filtered using a combination of morphological and progressive TIN filters. The resulting terrain points were then used to create the initial TIN approximation of the DTM, based on which the terrain model would be further refined and adjusted. The process of locating more points on the ground from full-waveform LiDAR data allowed for the densification of the DTM to occur and thus delivered a more accurate representation of the ground surface.

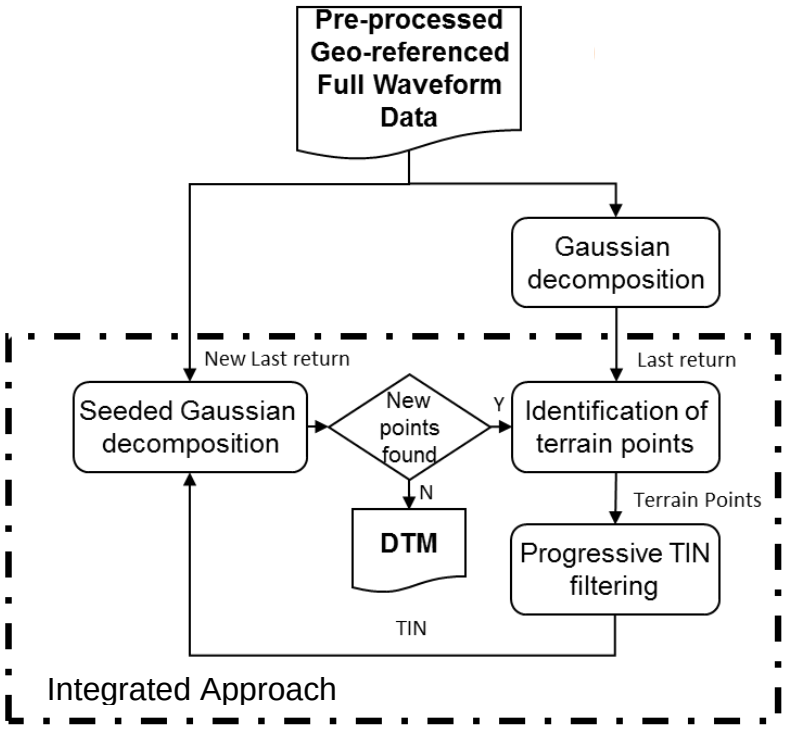

Figure 5.1 The diagram of the developed DTM extraction method

The digitized full-waveform data often contain returns that cannot be initially determined by the pulse detection and Gaussian fitting algorithms (weak echoes). On the basis of the initial DTM, it becomes possible to re-evaluate these candidate echoes embedded in the full-waveform through the proposed integrated method, which fully took advantage of the additional remaining data. The utilization of the initial DTM together with the geo-referenced waveform data allows for an indication of the area of the waveform to search for additional ground returns. This process is referred to as the "seeded Gaussian decomposition" in this research.

If an additional echo was found through the seeded Gaussian decomposition, it was then extracted and added to the list of candidate terrain points. Using these additional candidate points, the progressive TIN generation and the seeded decomposition were repeated. Once no more candidate points were located through the seeded Gaussian decomposition, the current TIN was stored as the latest updated DTM. As a result of this iterative process, the density of the ground points was increased so that the iteratively updated DTM could model the actual terrain better and better. In the following two sections, the two main components of the developed workflow: "Progressive Tin Filtering" and "Seeded Gaussian Decomposition" (SGD) are discussed in more detail.

5.2 Progressive TIN filtering

The identification of the initial terrain points was the first step in the developed method. In this research a pre-determined neighbourhood search algorithm was used to traverse through the terrain points as in Axelsson (2000) and Lin and Mills (2009). In this algorithm, the lowest points in the neighbourhood were treated as the initial terrain points. The morphological opening operation (Chen et al., 2007) (Soille, 2003) was applied to automatically identify the dominant object sizes in the scene of interest, which served as the basis for the determination of the neighbourhood size. The morphological operations, which are used to analyzing raster imagery, were adapted for LiDAR data in this research.

The window size of the morphological filter dictated the maximum size of an object that could be removed from the scene. In order to produce an optimal result, the filter size was determined automatically using an in-house algorithm developed by the Earth Observation Laboratory at York University (Jing et al., 2012). The algorithm worked by evaluating the effects of incrementing the diameter of the window and assessing the differences from one sized window to the next. In particular, the mean value of the difference of two consecutive morphologically filtered grids was computed. A series of disk shaped structuring elements (SEs) with diameters from 0.25 m to 10 m were employed in the opening operations (as per Section 2.4.1) to result in corresponding opened data clouds. In each opened dataset, the objects that fully contained the corresponding SE were retained, whereas the smaller ones were sifted. For each pair of the consecutive opened data, the mean of their differences was calculated by using the mean of the opened data with the smaller SE size as the minuend.

The result obtained from the subtraction of consecutively opened point clouds for one of the sites is shown in Figure 5.2, where the Y-axis is the mean value obtained from differencing and the X-axis is the SE diameter used. The peaks in the plot indicate the presence of objects with that specific diameter in the scene, whereas a local minimum indicated that there was a large number of objects removed between two consecutive opened images. The slope of the plot can reveal the size distribution and the scale of the objects in the scene. As demonstrated by Figure 5.2, there is a wide range of objects of different size present in this scene clustered into multiple dominant size groups smaller

than 6 m in diameter. The identification of the last local minima, before the line started "levelling off", provided the best SE size to use for a morphological filter in order to remove the high frequency components from the scene (i.e., shrubs and trees). In Figure 5.2 it is noticeable that when the opening operator had radius of 6m, the variation of the line stops and the line approaches the zero difference mark.

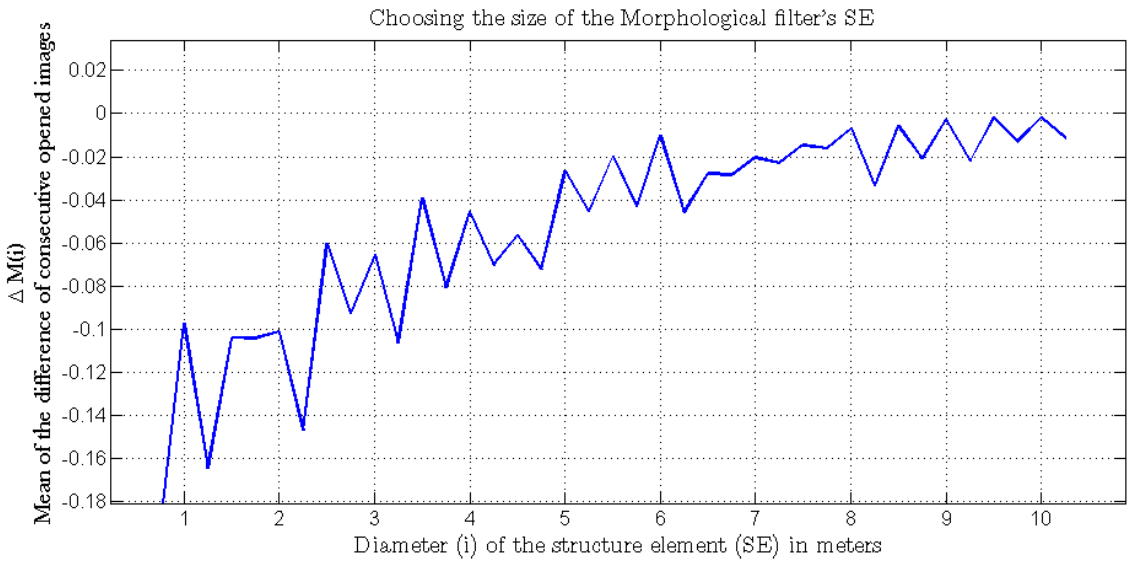

Figure 5.2 Difference between the mean values of the opened DSMs for Plot 1, ΔM(i) = M(i + 0.25) – M(i), where M(i) is the mean value of the opened DSM with the disk SE (structural element) of a diameter i metres

Based on the results obtained from the algorithm described in Jing et al. (2012), a disk of an appropriate diameter was used as the search space for each LiDAR point (in terms of their horizontal position). If a LiDAR point was the lowest in its neighbourhood, it was considered as a candidate terrain point. It is worth mentioning that the size of the neighbourhood changes from iteration to iteration as well as from site to site. In this

study, the neighbourhood was often reduced to two metres on second iteration for most of the sites.

Furthermore, the filtered points were taken as the base of the progressive TIN algorithm. This meant that the additional points were used to construct the resulting initial DTM, thus the terrain TIN model created would better fit the ground surface scanned. The TIN model generation was implemented using CGAL (Computational Geometry Algorithm Library, http://www.cgal.org/). This library made it possible to construct a TIN model from a given set of points. The progressive TIN algorithm was constructed as per the description provided in the background Section 2.4.4.

In addition to selecting the neighbourhood size, input parameters for the progressive TIN algorithm were also required. The necessary input parameters for the progressive TIN algorithm were chosen based on pre-knowledge of the study sites. In this case they were chosen based on the fact that in most cases the terrain was gently rolling and the chosen study sites did not have abrupt changes (such as cliffs, steep banks, etc.). The maximum angle of iteration was set to 6 degrees; the maximum distance of iteration was set to 1.4 metres, and the maximum resulting terrain angle chosen was 80 degrees (please see Section 2.4.4 for a review of these parameters).

In the progressive TIN algorithm, the “Barycentric Technique” (Scott, 2006) outlined in Equation 5.4 was used in order to find all points falling within a specific TIN facet. By

only considering the X and Y coordinates of each vertex (denoted as *A*, *B* and *C* in Figure 5.3) of the facet as well as only the X and Y coordinates of each test point (*P*), Equation 5.4 yielded a logical test that allowed for the conclusion of whether or not point *P* fell inside or outside the facet.

For the calculation of the iteration angle and the iteration distance, basic algebraic relationships were implemented:

$$\theta = \frac{\pi}{2} - \arccos\left(\frac{\left(\overrightarrow{AC} \times \overrightarrow{AB}\right) \cdot \overrightarrow{AP}}{\left\|\overrightarrow{AC} \times \overrightarrow{AB}\right\| \left\|\overrightarrow{AP}\right\|}\right) \tag{5.1}$$

$$D = \left\|\overrightarrow{AP}\right\| \sin\theta$$

wherein:

A is the closest vertex to point *P*

A B and *C* are vertices of the facet (labelled clockwise)

D is the vertical distance; and θ is the iteration angle

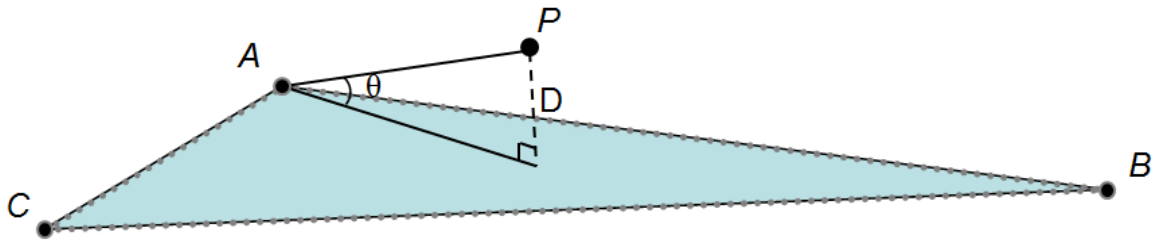

Figure 5.3 Progressive TIN algorithm parameters: θ - iteration angle and D – iteration distance, *P is* point to be tested, and *A*, *B* and *C* are TIN facet vertecies.

The terrain angle was computed for all the vertices as follows:

$$\Theta = \arctan\left(\frac{\Delta Z_P}{\sqrt{\left(\Delta X_P{}^2 + \Delta Y_P{}^2\right)}}\right) \tag{5.2}$$

wherein the ΔX_P, ΔY_P and ΔZ_P are the components of the vector from a facet vertex to point P and Θ is the terrain angle.

The progressive TIN algorithm traversed through all the candidate points to check if these could be classified as terrain. During each iteration, the newly identified terrain points were then used to recalculate the TIN model. The algorithm stopped, once no new points were added, producing a TIN model ready to be used in the seeded Gaussian decomposition.

5.3 Seeded Gaussian Decomposition

For every facet of the TIN model obtained from the progressive TIN algorithm, all of the laser waveforms passing through the facet were identified. To accomplish this, geo-referenced waveform data was used, specifically the coordinates of the point of origin (X_o, Y_o, Z_o) and unit vector (Δx, Δy, Δz) parameters of the waveforms.

Initially, the equation of the plane was computed using the three vertices of the facet. The point of intersection of the waveform with the plane that the facet created was then found by solving the systems of Equations 5.3a and 5.3b for parameter distance (*dist*) using Equation 5.3c. Substituting the derived distance back into the original equation of the vector (Equation 5.3b), the X, Y and Z of the point of intersection (with the facet plane) P

could be found. The computed points *P* were then tested to check if they fell inside the facet (and thus if the waveforms intersects the facet) using a "Barycentric Technique" Equation 5.4.

If the waveform was found to intersect the facet, it would become possible to "seed" the potential location of ground returns (terrain points) within the intersecting waveform using the distance (*dist*) obtained previously from Equations 5.3.

$$Z = aX + bY + c \tag{5.3a}$$

$$\begin{bmatrix} X_o + \Delta x \times dist \\ Y_o + \Delta y \times dist \\ Z_o + \Delta z \times dist \end{bmatrix} = \begin{bmatrix} X \\ Y \\ Z \end{bmatrix} \tag{5.3b}$$

$$Z_o + \Delta z \times dist = a(X_o + \Delta x \times dist) + b(Y_o + \Delta y \times dist) + c \tag{5.3c}$$

$$\mathrm{u} = \frac{(\overrightarrow{\mathrm{BA}} \cdot \overrightarrow{\mathrm{BA}} * \overrightarrow{\mathrm{CA}} \cdot \overrightarrow{\mathrm{PA}} - \overrightarrow{\mathrm{CA}} \cdot \overrightarrow{\mathrm{BA}} * \overrightarrow{\mathrm{BA}} \cdot \overrightarrow{\mathrm{PA}})}{(\overrightarrow{\mathrm{CA}} \cdot \overrightarrow{\mathrm{CA}} * \overrightarrow{\mathrm{BA}} \cdot \overrightarrow{\mathrm{BA}} - \overrightarrow{\mathrm{CA}} \cdot \overrightarrow{\mathrm{BA}} * \overrightarrow{\mathrm{CA}} \cdot \overrightarrow{\mathrm{BA}})}$$

$$\mathrm{v} = \frac{(\overrightarrow{\mathrm{CA}} \cdot \overrightarrow{\mathrm{CA}} * \overrightarrow{\mathrm{BA}} \cdot \overrightarrow{\mathrm{PA}} - \overrightarrow{\mathrm{CA}} \cdot \overrightarrow{\mathrm{BA}} * \overrightarrow{\mathrm{CA}} \cdot \overrightarrow{\mathrm{PA}})}{(\overrightarrow{\mathrm{CA}} \cdot \overrightarrow{\mathrm{CA}} * \overrightarrow{\mathrm{BA}} \cdot \overrightarrow{\mathrm{BA}} - \overrightarrow{\mathrm{CA}} \cdot \overrightarrow{\mathrm{BA}} * \overrightarrow{\mathrm{CA}} \cdot \overrightarrow{\mathrm{BA}})} \tag{5.4}$$

$$\text{if } \mathrm{u} >= 0 \text{ and } \mathrm{v} >= 0 \text{ and } \mathrm{u} + \mathrm{v} < 1 \text{ then the point is inside the triangle}$$

wherein A B and C are the vertices of the facet (triangle in TIN) and *P* is the point being tested.

With each consecutive facet, the number of possible intersecting waveforms was decreased which allowed to reduce the processing speed of the algorithm.

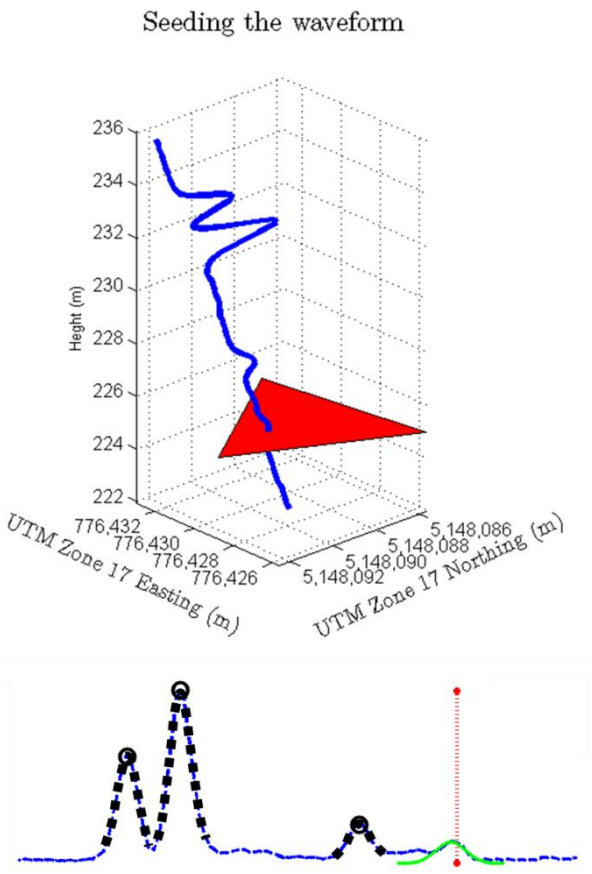

Figure 5.4 The full-waveform LiDAR signature passing through a facet of the terrain TIN model (top). The black circles are the peaks of the returns detected by the Gaussian decomposition method (bottom). The red line shows the location of the seed (point of intersection of the waveform and the TIN facet) used for the seeded Gaussian decomposition (SDG), and the green curve is the result of fitting one Gaussian function to the region near the seed.

The location on the waveform where the laser pulse intersected with the facet was used as the seed for the SGD. For example, one of laser pulses passing through the red facet in the TIN model along with its full-waveform return is shown in Figure 5.4. For the waveform in Figure 5.4, three returns were detected (black dashed line with circle marking the peak) using the Gaussian decomposition method described above, and these returns were backscattered from a tree. The red dashed line shows the location of the seed in the full waveform (the seed location was the point of intersection of the facet and the

waveform). The SGD (algorithm is described in detail in Section below) was then used to fit a Gaussian function near the seed and an additional return (green curve) was detected.

The implemented SGD algorithm (Figure 5.5) was used for detection of weak pulses in a specified (seeded) search region that was considered to most likely contain the returns associated with the terrain (visualized as a red dashed line in Figures 5.4). The proposed SGD algorithm also used LM algorithm for Gaussian parameter estimation, however the pulse detection process (step 1 in Figure 5.5) was substantially less involved than the one used for the Gaussian decomposition algorithm described previously. The seeded region (approximately one metre in either direction from the estimated terrain level) was evaluated from right to left in order to locate the cluster of points that best resembled a return pulse (green line in Figure 5.4). The rightmost maxima point in the seeded region was then identified as a first point of a segment to be fitted. The segment was grown recursively starting from the maxima point and expanded in both directions to include all the samples that were less in the amplitude than the samples added in a previous iteration.

If the total length on the segment satisfied the minimum point requirement (7 samples minimum due to larger noise effects associated with lower amplitude pulses), the Gaussian fitting was performed on the extracted segment to fit one return only (step 2 in Figure 5.5). The fitted echo was then analyzed for the width and goodness of fit requirements (step 3 in Figure 5.5) and ringing effect. If the constraints were met, then

point was geo-referenced and included into the dataset. Otherwise, the next candidate cluster in the seeded region (going right to left) was evaluated (step 4 in Figure 5.5).

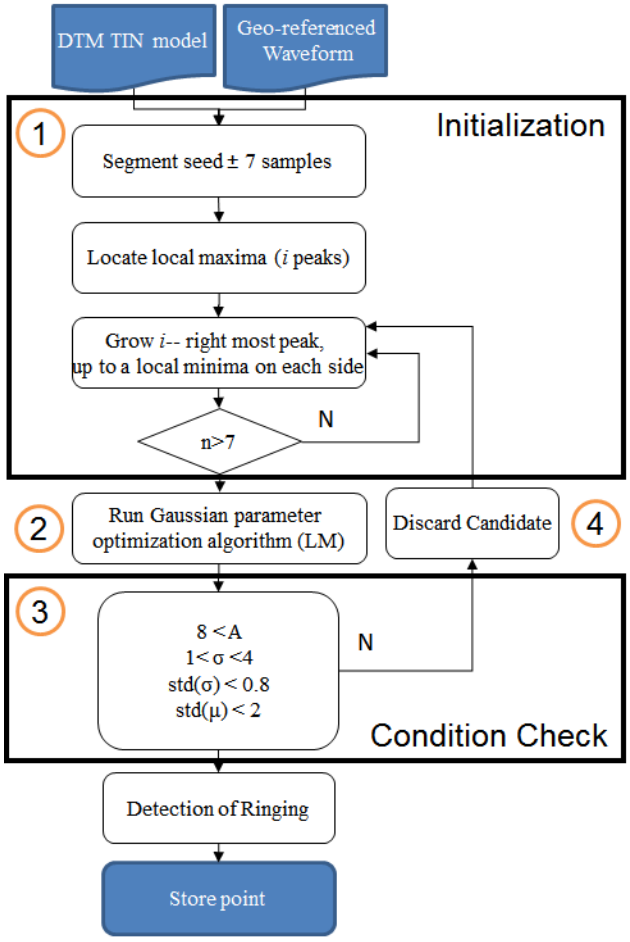

Figure 5.5 The workflow for the developed SGD algorithm.

After the SGD, a number of new candidate terrain points were detected. These new points were fed back into the module of "progressive TIN filtering" (Step 4 in Figure 5.1) together with previously derived ground points for the next iteration of the algorithm. If there were no new points detected by the SGD algorithm, the TIN terrain model used to initialize the SGD was stored as the final DTM. In general, running two iterations was

found to be sufficient for vast majority of the discernible low amplitude echoes to be included into the DTM.

6 Case study and validation

In this Chapter, the accuracy assessment of the airborne LiDAR data is discussed and the two LiDAR DTMs of the study sites, one obtained via the developed algorithm and the other from the TerraScan software, are introduced. These two LiDAR DTM extraction methods were compared with each other and evaluated against the collected ground reference data.

6.1 Accuracy assessment of the derived LiDAR data

This section provides a description of the estimate of the expected platform accuracy for the LiDAR system used to collect data for this research. The estimated accuracy was used to establish a baseline for the expected absolute and relative errors of the DTMs derived from the LiDAR point cloud data. In particular, the errors were estimated for the DTMs that made use of low amplitude ground returns. In order to estimate the errors associated with the LiDAR platform, I analyzed the accuracies of both the direct geo-referencing component and the LiDAR component used to compute the incremental coordinates form the LiDAR to the targets. The result of this error analysis provided the estimate of the LiDAR point cloud accuracy in horizontal and vertical directions.

The airborne platform contributed two types of errors to the final LiDAR derived point coordinates: the low frequency and the high frequency errors. The former was a systematic error, which caused the offset between the computed and absolute values to

slowly diverge. It was mainly a function of the SBET solution at each epoch and its deviation from the true position and orientation. The second part of the low frequency errors was driven by the constant errors due to minor systematic offsets of lever arms and boresight angles. This group of errors was responsible for systematic offsets and the slow drifts of the computed solution away from the true position and orientation values. However, since the drift changed slowly over time, its effect on the derived points would appear as a general directional offset form the true value rather than random noise.

The high frequency "relative" errors were mainly caused by the uncertainty of the waveform fitting algorithm for the extraction of the target distances. There were also some high frequency errors introduced by the angular mirror and rangefinder. Due to the stability of the epoch to epoch solution that was produced by the POS, the resulting position and orientation data were consistent in the short term and did not appear to be visually disjointed. However, when the Gaussian decomposition algorithm was used to extract the targets from the waveform, the accuracies of the estimated parameters were unrelated to each other. Therefore, the accuracies of the derived points located in the same neighbourhood might vary, so might the offsets.

Uncertainties associated with both the direct geo-referencing and the LiDAR range determination were considered here for estimation of positional accuracy of the final point cloud dataset. Specifically, the direct geo-referencing errors associated with the data collection and analysis were investigated, as these data were used to obtain the EO

parameters. In addition, errors related to the LiDAR system's raw data acquisition were considered, as well as the LiDAR rangefinder error and data processing uncertainties due to target extraction form the full-waveform signatures were considered.

The direct geo-referencing system used on the scanner platform was the Applanix POS AV 310 system with a dual-frequency GPS receiver and an IMU sensor. The system specifications provided by Applanix Corporation, (2012) for expected EO accuracies at 1σ for 3D vector position was 0.05 m - 0.30 m, and for orientation the roll, pitch, and heading were 0.015, 0.015 and 0.035 degrees respectively. The specifications for the Applanix POS AV 310 provided above are a general guideline for the expected EO sensor error after the post-processing of the collected data using the POSPac MMS software. These values were used to estimate the approximate orientation accuracy for the LiDAR platform. For position accuracies, the average 3D RMS values (1σ) obtained from POSPac MMS software (provided by GeoDigital) were used: 0.03 m, 0.03 m and 0.06 m for north, east, and up components respectively.

The rangefinder accuracy associated with Riegl's LiDAR was provided as 20 mm + 20 ppm (Hug et al., 2004; Schaer, 2010). This rangefinder accuracy value was used as a measure of the accuracy of the time-tagging of the recorded raw waveform samples, and not as a measure of the error associated with target extraction. Instead, the error associated with the fitted mean value μ, which was used to calculate the distance to the target (one of the parameters that describe a Gaussian waveform as per Equation 1.5) was

used as a measure of accuracy for the extracted target ranges. Figure 6.1 demonstrates how the estimated error for μ was affected by the higher and lower amplitude pulses. This error was highly randomized and did not behave in a systematic manner.

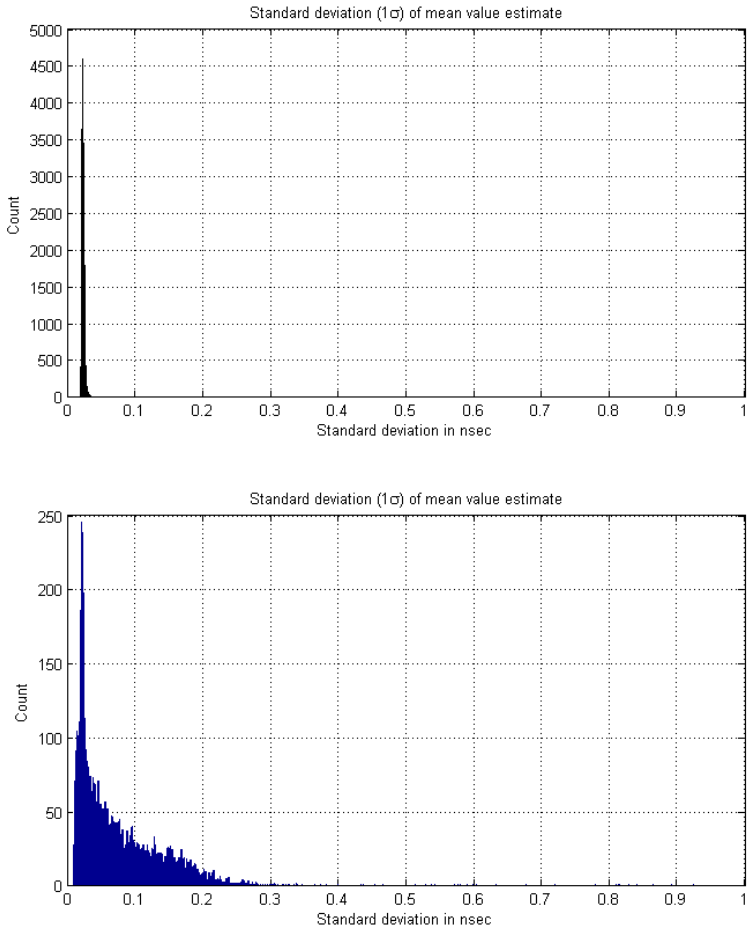

Figure 6.1 Histogram of standard deviation of the estimated error for the mean value (μ) obtained from Gaussian fitting using LM algorithm. Histogram on the bottom is from a site of mostly low amplitude (hence higher noise) pulses, while the histogram on the top is from an open area containing predominantly higher amplitude pulses.

It is visible from Figure 6.1 that the majority of the standard deviation values associated with the Gaussian fitting of the mean (μ) fell below 0.03 ns for high amplitude returns and below 0.25 ns for low amplitude returns. Thus, the error associated with the

calculated mean values (μ) can be approximated as 0.5 cm at 1 sigma (0.03 ns at 15 cm/ns) for strong (high amplitude) returns and 3.0 cm at 1 sigma (0.2 ns at·15 cm/ns) for lower amplitude returns. Since the range to target was calculated as the distance between the emitted pulse (high amplitude) and the received pulse, the estimated range error component due to target extraction was computed to be: 3.5 cm at 1 sigma from the sum of the lower and higher amplitude pulses' associated range determination errors (3 cm + 0.5 cm). Therefore the total estimated range error component was estimated at 55 mm+20 ppm at 1 sigma.

To estimate the total error of the LiDAR points coordinates due to the accuracy of the EO solution and LiDAR's range determination error, a Jacobian of a transformation matrix was computed and rigorous error propagation was performed. Substituting the LiDAR's scan direction (i.e., forward pointing system) and associated accuracies, the error values attached to the extracted LiDAR points can be calculated. The specifications for the POS orientation accuracies provided above were used as the error estimates for the orientation accuracies of the platform, while the average of the position RMS values where used for the position error estimates. The results of these estimations are demonstrated in Figure 6.2.

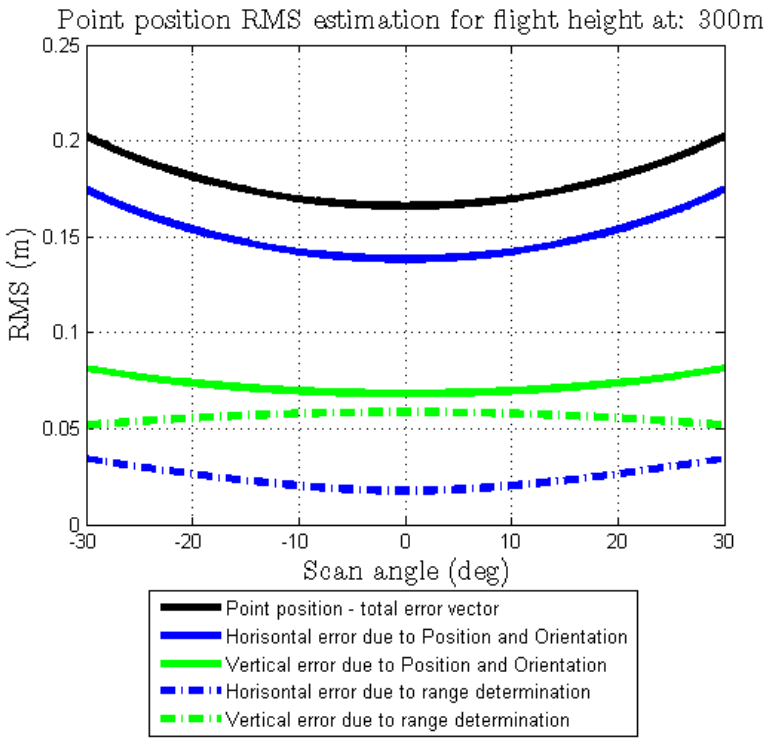

Figure 6.2 The RMSs in the positions of LiDAR points taking into consideration of the configuration of LiDAR used (forward pointing) at 300m flight height. For the calculation of the horizontal component error here, the footprint size of the LiDAR emitted pulse is not taken into consideration. From the diagram it is visible that the error associated with range is responsible for almost 50% of the total error in the vertical component (the z coordinate value).

The overall positional accuracy for the LiDAR points extracted from the low amplitude returns was estimated to be 0.20 m (1σ), with the vertical relative error component at 0.06 m and absolute error component at 0.08 m (1σ).

The absolute accuracy of the LiDAR dataset did not greatly affect the geometries of the overlapping scans for one main reason; opposite direction scan lines were flown within 10 minutes of each other. Thus, not enough time elapsed between scan lines for the solution to drift substantially and make it visibly problematic to overlap the datasets. The

vertical offset in the datasets flown over the same site in opposite direction was a few centimetres in some sites – a difference that was essentially unnoticeable when processing the LiDAR data.

The discussion of the accuracy assessment provided in this section is very general, and does not include many contributing factors such as the LiDAR footprint size or the methodology involved in obtaining the EO solution. From the final post-processed navigation dataset, only the estimated errors associated with accuracy of the position and orientation were used. In addition, only the errors associated with the target extraction from full-waveform data were used to obtain the plot above, to provide a general demonstration of the LiDAR platform's accuracies.

6.2 DTM extraction algorithm evaluation and validation

The generated DTMs for the study sites were validated using the ground survey data as well as being compared with the results obtained from commercial TerraScan software. The results of the DTM extraction were measured against three different criteria: assessment of the produced point densities; point coverage; and the analysis of the quality of the terrain height estimation of DTMs compared with the ground reference data in five study sites. Detailed plots and descriptions of these five sites can be found in Appendix B. The DTMs for these five sites generated by the developed method and by TerraScan are shown in Figure 6.3.

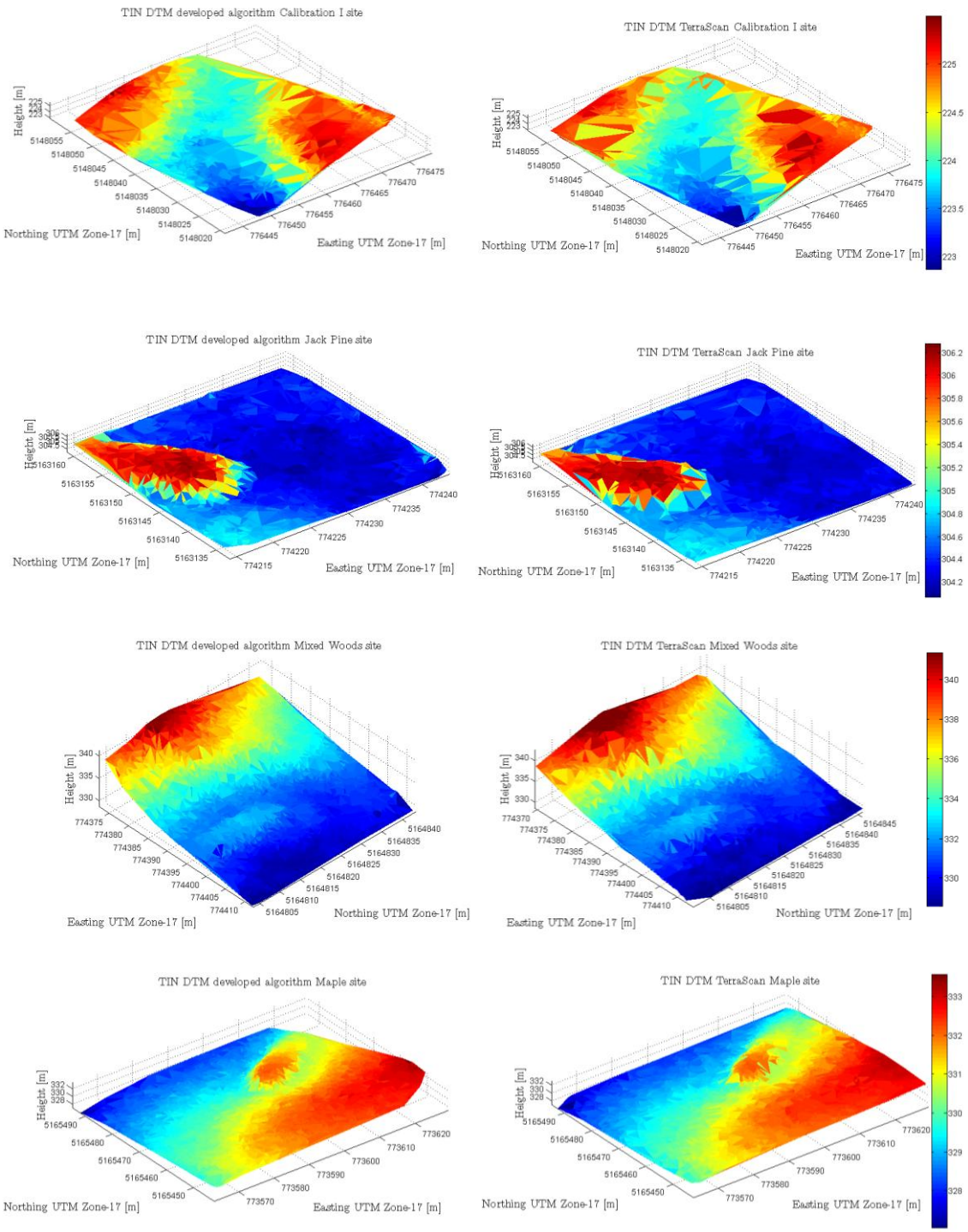

Figure 6.3 TIN representations of the DTM models created from LiDAR data using the developed algorithm (Left) and TerraScan (Right).

To clearly show the results, I provide a subset of the DTM of each forest site in Figure 6.4. From these figures it can be seen that there were more points detected using the developed algorithm and thus the mounds under trees were better defined.

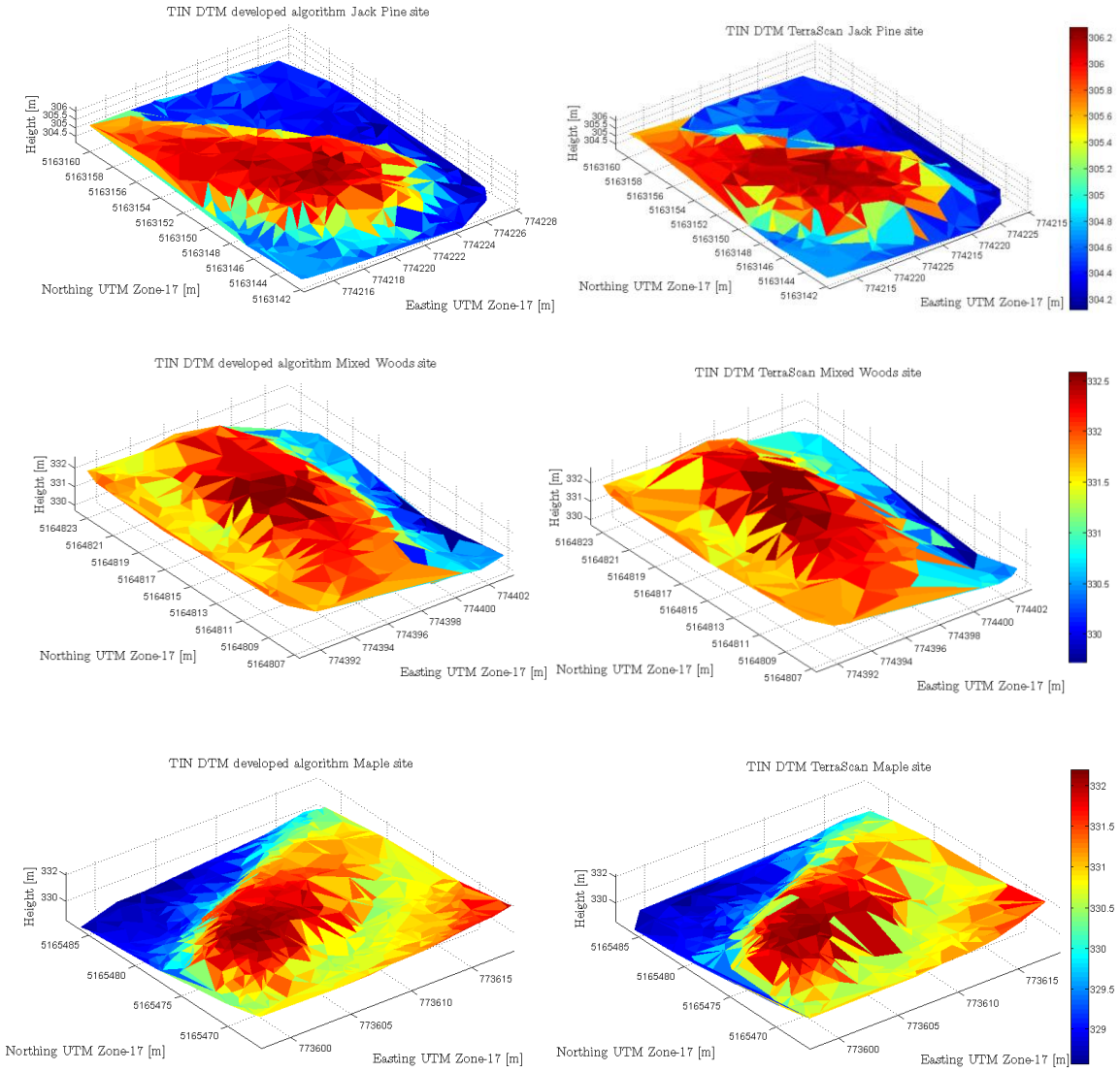

Figure 6.4 TIN representations of the DTM derived from LiDAR, zoomed in to a small mounts on (top to bottom) Jack Pine, Mixed Woods, Maple sites with developed algorithm DTM (Left) and TerraScan DTM (Right)

For visualization of the ground reference data coverage, a TIN model of the Mixed Woods site with the survey collected points projected on top of it is provided in Figure 6.5.

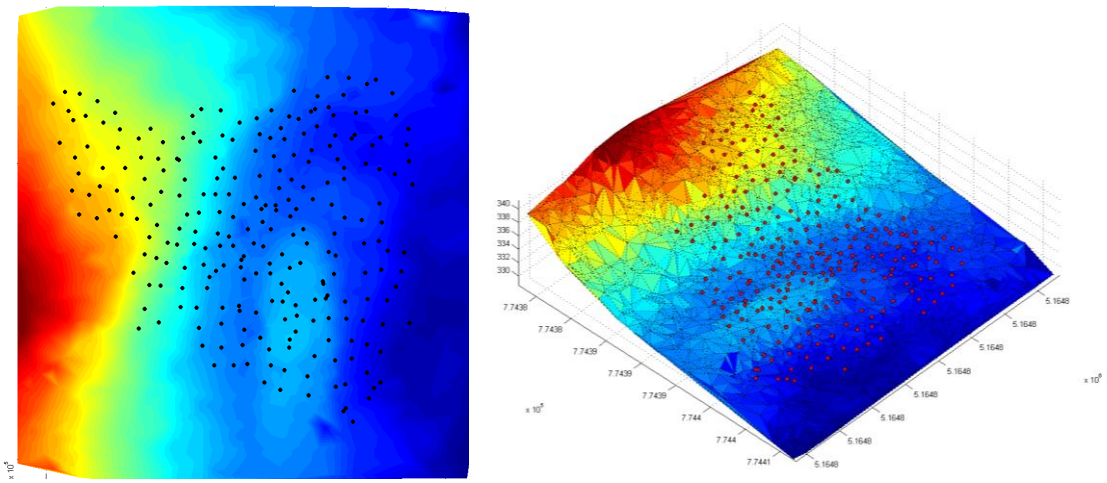

Figure 6.5 The ground reference points projected onto the extracted DTM model

By overlaying the ground points extracted using the two methods (shown in Figure 6.6), it is evident that the terrain points detected by the developed algorithm visually appeared to have more coverage and higher density than those derived with the TerraScan software.

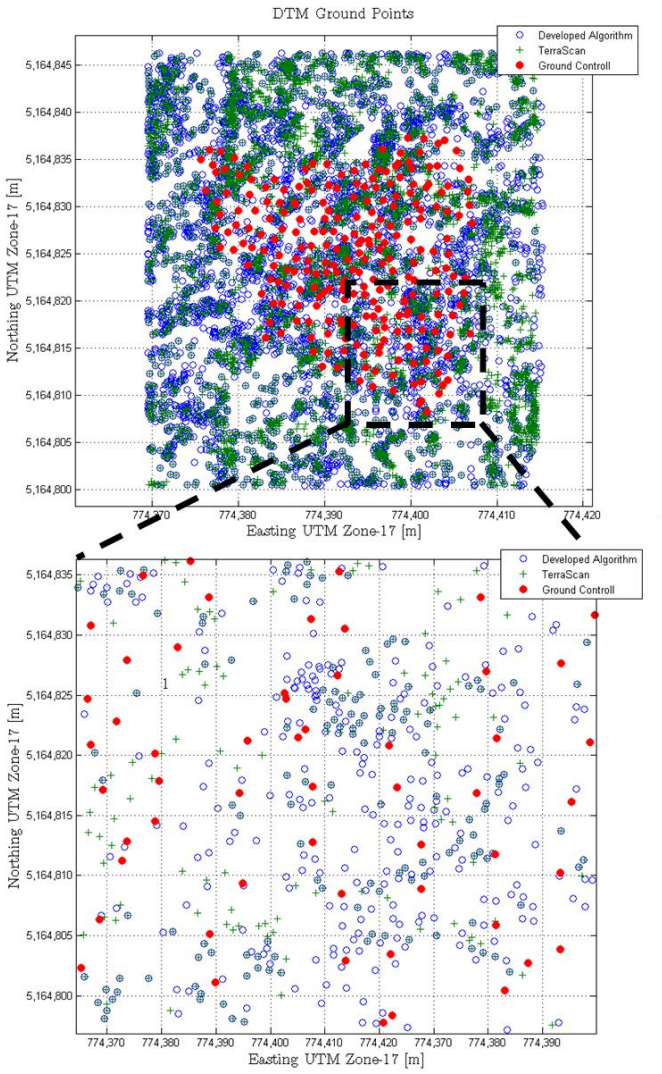

Figure 6.6 Point distribution from three different terrain models, in blue are the points form developed algorithm, in green are from TerraScan software and in red are ground reference points

Table 6.1 demonstrates the density of the detected terrain points at each site. Both DTM methods are evaluated by simply dividing the total number of terrain points detected by the area of the study site.

Table 6.1 Comparison of two different sets of LiDAR derived DTM's point densities

	Average of Site Ground Point Density (points m^{-2})		
Study Site	Ground Classification tool - TerraScan	Developed algorithm	Improvement
Calibration I	1.6	2.5	+56%
Calibration II	5.7	21	+250%
Jack Pine	2.1	2.9	+38%
Maple	1.3	2.5	+92%
Mixed Woods	1.8	2.3	+28%

The improvements in point density were mostly due to the addition of low amplitude points that were not included in the TerraScan model. The reason for the lack of low amplitude points in the TerraScan model was due to processing constraints in commercial software that were used in a LiDAR processing workflow. Table 6.2 shows the number of additional points (points that were not initially detected altogether using the commercial software) that were detected by the algorithm developed in this work.

Table 6.2 Newly detected points that were not picked up by Gaussian decomposition performed with commercial software and were detected (and classified as ground points) as a result of processing done by the developed algorithm.

	Calibration I	**Calibration II**	**Jack Pine**	**Mixed Woods**	**Maple**
Newly detected Points	675	150	795	1245	2591
Total Ground Points	2385	9000	2161	2395	6419
New points as a % of total	28%	1.67%	37%	52%	40%

The number of new points detected for the Maple and Mixed Woods study sites was larger than for the rest of the sites mainly due to the presence of heavy foliage top cover in these plots. This dense top layer of the canopy meant that the pulses that reached the ground were generally low in amplitude and were not detected by existing processing methodology as shown through these tests. The Jack Pine and Calibration I study sites contained a large number of evergreen trees. These coniferous trees did not permit the LiDAR pulses to travel through and thus as a result the waveform did not reach the ground. In addition, the Jack Pine and Calibration I study sites also had thick underbrush which can further impede the LiDAR penetration to ground, thus the number of new points detected in these study sites was not as substantial. Finally, the Calibration II study site saw the least improvement since it was an area of open terrain. Hence, most waveforms are one target returns resulting in very few additional low amplitude pulses.

To analyze the point coverage of the resulting DTMs, each site was assigned a one by one metre grid and the number of points that fell within each grid cell was calculated. A ratio of the number of cells containing at least one point to the total number of cells was computed for each DTM. This ratio provided the information on coverage of the derived terrain model while the visualization of the grid demonstrates the distribution of gaps in coverage. Figure 6.7 contains the results of this analysis for all the study sites for both DTM's extraction methods.

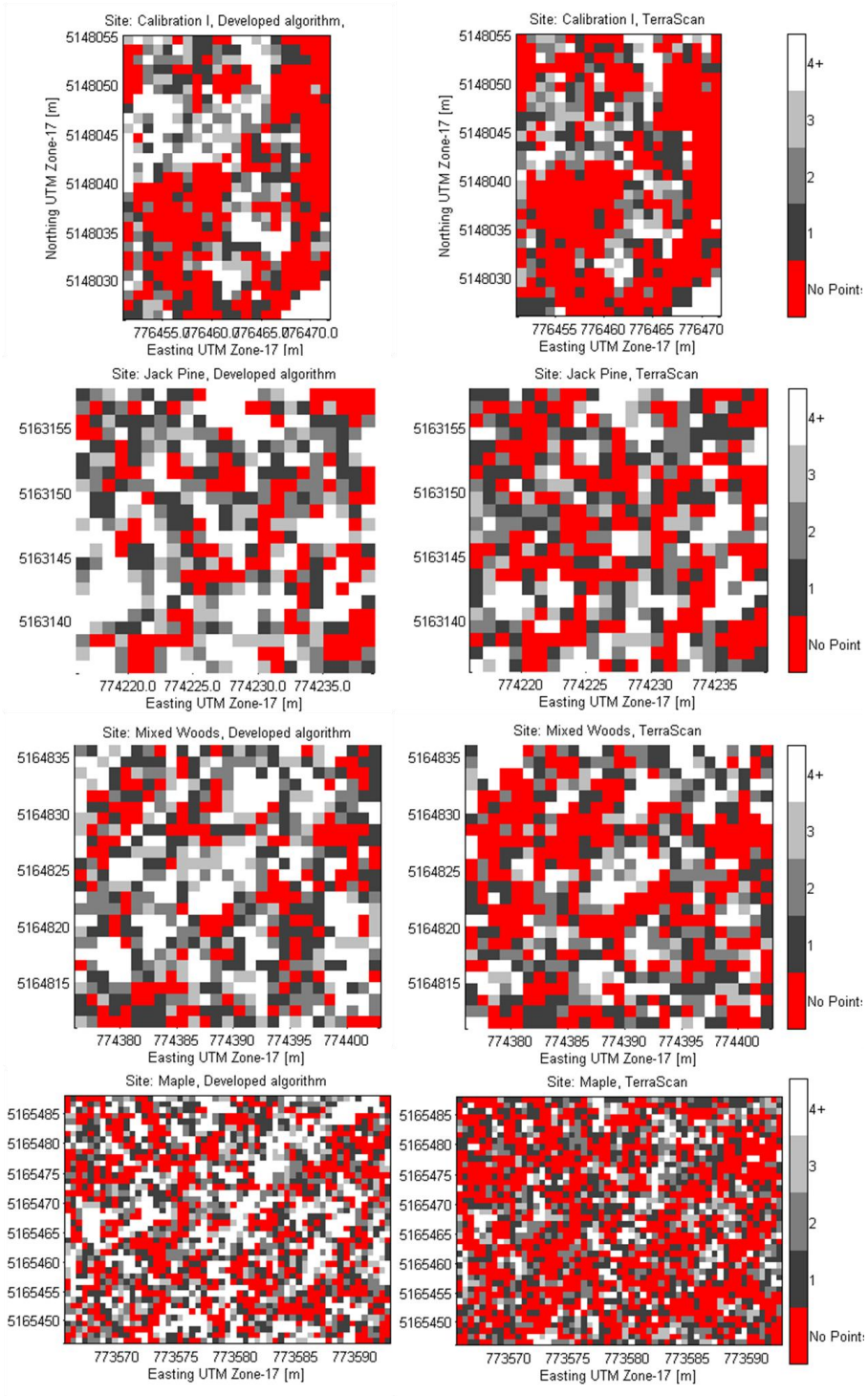

Figure 6.7 The grid of point densities and coverage at each site, with the densities from developed algorithm on the left and the TerraScan on the right. The red color represents cells where there was no points detected for the given terrain model, and points ranging from black to white representing a range from 1 point per cell to 4+ points per cell.

Table 6.3 Comparison of coverage between two DTM generation methods.

Site	Coverage TerraScan (%)	Coverage developed algorithm (%)
Calibration I	47	57.1
Jack Pine	65.5	77.9
Mixed Woods	64.7	78.8
Maple	55.1	70.2

The plots in Figure 6.7 and Table 6.3 demonstrate that the developed method generated a better point coverage than TerraScan. This overall improvement in coverage can be more beneficial for terrain reconstruction than the detection of a large number of points in areas that already had ground points detected. By minimizing gaps in coverage, there was a greater probability of detecting terrain variations that could have been missed otherwise, and therefore a more accurate representation of the terrain could be obtained as a result.

The accuracy assessment of the LiDAR derived terrain models was accomplished using the inverse distance weighting (IDW) and TIN distance analysis techniques. Detailed description of these techniques can be found in Appendix G. Figure 6.8 is a visual representation of the spatial residual distribution obtained as a result of TIN distance analysis of LiDAR DTMs versus ground surveyed data. These plots demonstrate the distribution and scale of residuals for the developed algorithm and TerraScan respectively, overlaid on the contour map of the Jack Pine study site. The histograms of the residual distributions along with spatial residual distribution plots for the rest of the sites can be found in Appendix H.

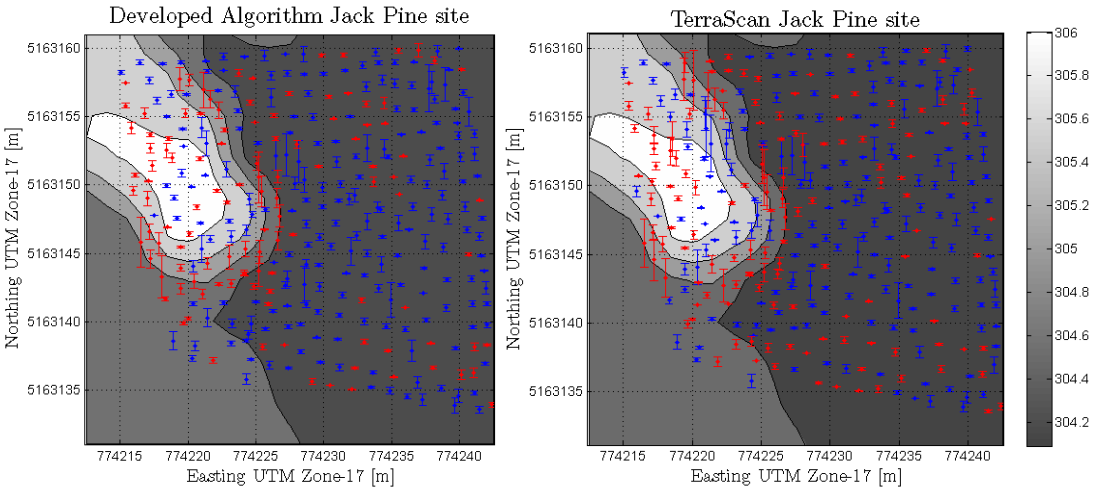

Figure 6.8 The spatial distribution of residuals obtained using TIN model distance comparison of the LiDAR derived DTMs with the ground reference data. The colour of the error bars signifies the sign of the residual value, red – negative, blue – positive.

The quantitative results of DTMs accuracy assessment are summarized in the Table 6.4. The measure of accuracy used here was the standard deviation of the vertical residual values, resulting from differencing of the LiDAR derived models with the ground reference data.

Table 6.4 demonstrates that the accuracies of the DTMs generated from LiDAR data for the wooded areas had vertical residual values that were higher than the estimated errors in Section 6.1. This outcome is expected due to the aforementioned difficulties associated with DTM generation under forest canopy. On the other hand, the vertical residuals associated with the DTM of the Calibration II site (an open field) were much smaller than the estimated error values. This site is located in an open area and the DTM consists mostly of strong ground return pulses, thus the resulting DTM is expected to be more accurate.

Table 6.4 The standard deviation and the mean values of the residuals calculated when comparing the generated terrain models from LiDAR data with the ground reference data for the preselected study sites using the TIN model distance method and IDW with interpolation making use of (a) all points within 2.5 metre search radius or (b) only using 5 closest points.

Site	Algorithm	TIN σ (cm)	TIN mean (cm)	IDW(a) σ (cm)	IDW(a) mean (cm)	IDW(b) σ (cm)	IDW (b) mean (cm)
Calibration I	Developed	5.7	1.1	6.9	6.7	7.4	4.1
	Terra Scan	5.5	2.3	8.2	2.0	8.8	1.4
	Improvement	-2.91%		15.18%		15.18%	
Calibration II	Developed	3.6	4.5	3.8	4.5	3.4	4.4
	Terra Scan	3.6	2.3	3.6	2.3	3.2	2.2
	Improvement	-0.56%		-5.52%		-8.86%	
Jack Pine	Developed	8.4	-1.7	9.1	-2.1	8.6	-2.1
	Terra Scan	9.9	-0.8	10.4	-1.8	9.5	-1.5
	Improvement	15.15%		12.50%		9.47%	
Mixed Woods	Developed	11.4	-5.1	13.7	-6.1	14.8	-6.8
	Terra Scan	14.5	2.2	18.1	-0.9	19.3	-1.0
	Improvement	21.34%		24.35%		23.29%	
Maple	Developed	8.9	-7.7	9.9	-8.1	11.3	-8.2
	Terra Scan	9.2	-7.2	10.7	-7.1	12.1	-7.6
	Improvement	3.26%		7.48%		6.94%	

It is also visible from the Table 6.4 that there was an overall improvement in accuracy for the terrain models that were generated by the developed algorithm in comparison with the ones generated by the TerraScan software. However, the DTMs obtained using the developed algorithm performed poorly for both Calibration study sites. This was likely because the Calibration study sites generally contained flat terrain that did not greatly benefit from densification of the ground points. The gently rolling terrain did not need a large point density to be accurately represented. On the other hand, it is observed that more accurate DTMs were generated by the proposed method for terrains exhibiting higher elevation variations, such as small hills. For example, in Figure 6.8, the area with higher terrain variation (the earth mound) was more accurately represented by the

developed algorithm. Table 6.5 provides the results of analysis of the generated terrain models for the sharply sloping terrain of the Mixed Woods site, as well as the subsections of the Jack Pine and Maple sites which contained small hills (earth mounds, shown in Figure 6.5). These results showed improvements. However, more datasets are required for a more definitive conclusion.

Table 6.5 The residuals calculated for subsections of the generated terrain models using TIN model distance. Subsets contained small earth mounds located at each site

Site	Algorithm	TIN σ(cm)
Small hill Jack Pine site	Developed	9.9
	Terra Scan	13.3
	Improvement: 25.12%	
Small hill Mixed Woods site	Developed	10.7
	Terra Scan	15.1
	Improvement: 29.10%	
Small hill Maple site	Developed	11.5
	Terra Scan	12.4
	Improvement: 7.7%	

The linear regression plots which are provided in Figure 6.9 were generated to compare the elevation values from the LiDAR DTMs with the ground surveyed ones for all study sites. When comparing the correlation (R^2) values at each site for the two sets of DTMs, it can be seen that for the sites containing dense vegetation and variable terrains, the DTMs obtained through the developed algorithm demonstrated higher R^2 values. The RMSE values also tend to be lower for DTMs generated using methodology developed in this research. This further demonstrates the improved performance of the developed algorithm over existing methodology in the forested areas with high terrain variation.

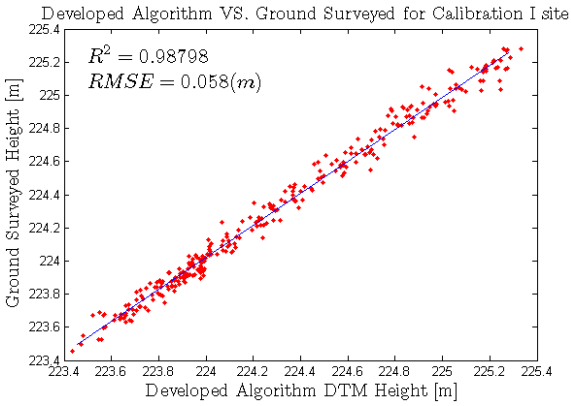
Developed Algorithm VS. Ground Surveyed for Calibration I site
$R^2 = 0.98798$
$RMSE = 0.058(m)$
Ground Surveyed Height [m]
Developed Algorithm DTM Height [m]

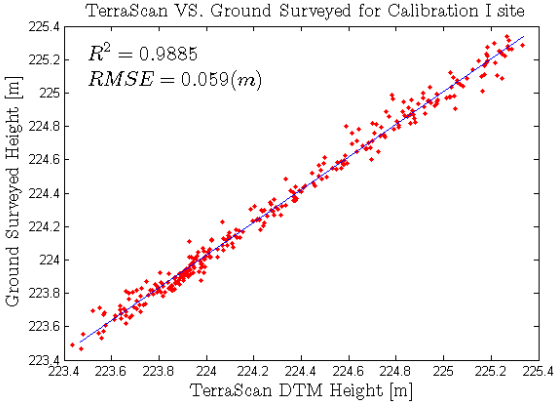
TerraScan VS. Ground Surveyed for Calibration I site
$R^2 = 0.9885$
$RMSE = 0.059(m)$
Ground Surveyed Height [m]
TerraScan DTM Height [m]

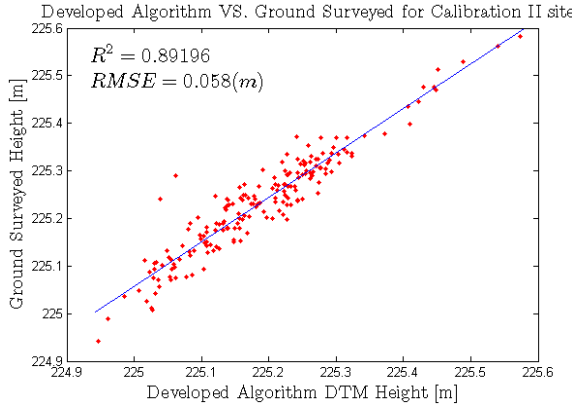
Developed Algorithm VS. Ground Surveyed for Calibration II site
$R^2 = 0.89196$
$RMSE = 0.058(m)$
Ground Surveyed Height [m]
Developed Algorithm DTM Height [m]

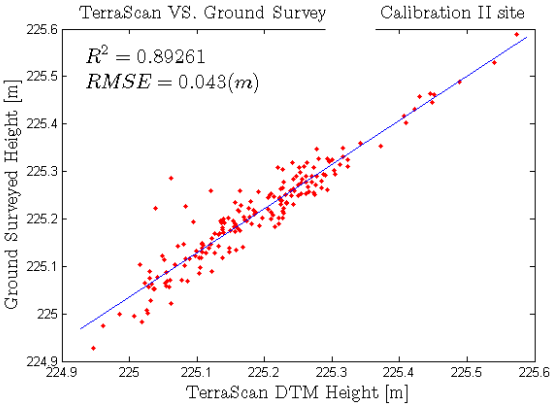
TerraScan VS. Ground Survey
Calibration II site
$R^2 = 0.89261$
$RMSE = 0.043(m)$
Ground Surveyed Height [m]
TerraScan DTM Height [m]

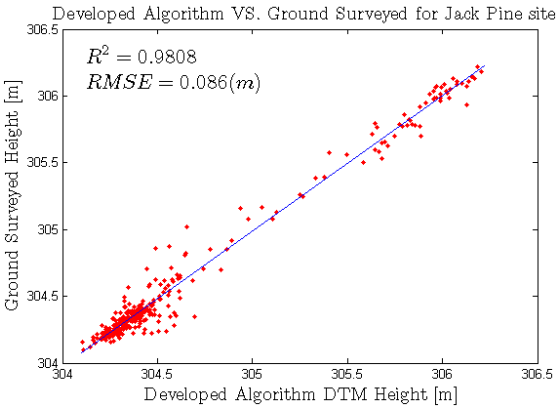
Developed Algorithm VS. Ground Surveyed for Jack Pine site
$R^2 = 0.9808$
$RMSE = 0.086(m)$
Ground Surveyed Height [m]
Developed Algorithm DTM Height [m]

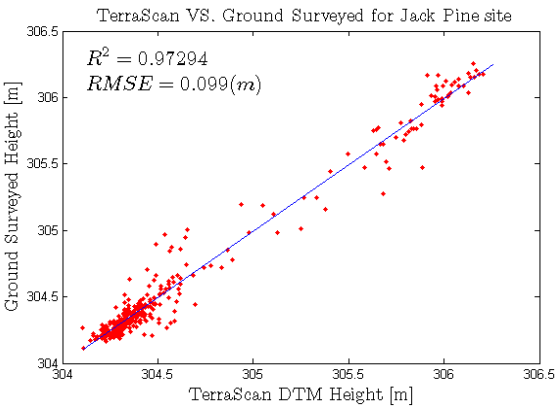
TerraScan VS. Ground Surveyed for Jack Pine site
$R^2 = 0.97294$
$RMSE = 0.099(m)$
Ground Surveyed Height [m]
TerraScan DTM Height [m]

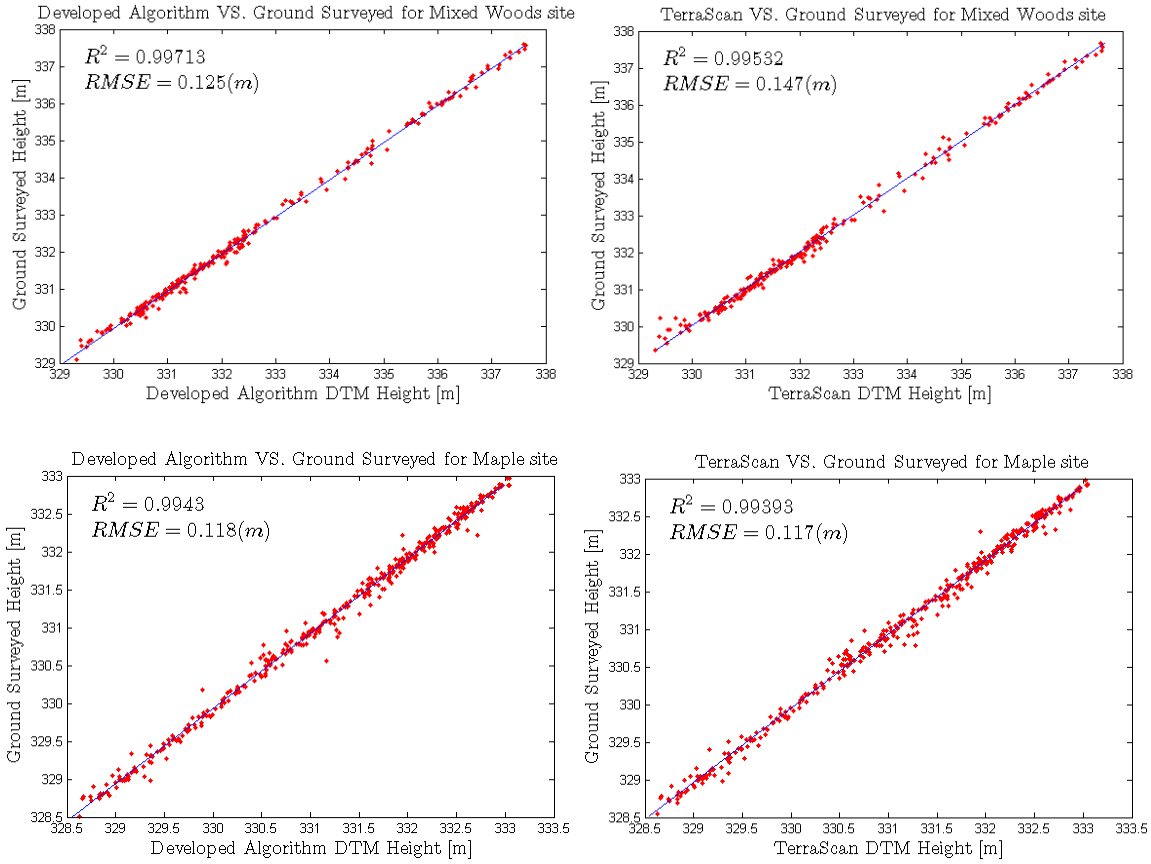

Figure 6.9 The linear regression plots comparing the elevation values for LiDAR extracted DTM with ground survey data. A TIN model of the LiDAR DTM's was used to derive the elevation at the coordinates corresponding to the ground survey points.

An observation on the overall accuracy can be made based on the flat unobscured terrain of the Calibration II study site. This segment provided a good baseline indication of the vertical accuracy values to be expected from the airborne LiDAR system. The Calibration II site has the lowest probability to contain errors associated with classification of low vegetation as terrain. In addition, this site predominantly contains only high amplitude returns, which generally have substantially less range error then the lower amplitude returns (as per Figure 6.1). The residual values for both DTM generation methods evaluated here against the ground reference data had 1σ standard deviation of 3.6 cm,

with mean residual value of approximately 3 cm. These results fall well within the ranges for theoretical error evaluation of LiDAR data provided in Section 6.1.

7 Conclusion and future work

Throughout this research, I developed an integrated approach to improve the DTM generation in vegetated area by detecting the weak pulses (with low amplitudes) generated from the terrain under trees. These weak echoes cannot be detected by commonly used Gaussian decomposition methods; but are very important for accurate DTM generation in wooded areas. The integrated approach incorporated the echo detection, terrain identification, and TIN model generation in an iterative process. In such a way, the built TIN model guided the echo detection in terms of its location and provided a constraint on Gaussian decompositions. As a result, the weak echo in a recoded full waveform that usually was generated by the terrain under vegetation was detected. In heavily forested areas, the extraction of low amplitude return pulses from full-waveform LiDAR signatures provided a denser point sampling of the terrain and thus a more accurate DTM.

More ground echoes were detected by the developed method compared with TerraScan's ground extraction routine. The point distribution and density plots (Figure 6.6 and 6.7) demonstrated the consistent improvements (by an average of 12%) in point coverage of the derived DTMs. The denser LiDAR point detection with the developed method contributed to more accurate DTM, especially for areas containing hilly or variable terrain.

The definite benefits of the addition of low amplitude, lower accuracy pulses to the DTM generation were clearly exhibited in the study sites of Jack Pine, Mixed Woods, and Maple (Table 6.3). The standard deviations of residuals in the DTM generated by the developed method were less than 11.4 cm for these three sites, while those corresponding to the TerraScan were up to 14.5 cm. Compared with TerraScan, the developed method improved the DTM accuracy by up to 21%. The improvement was even more significant (up to 29%) if only considering small areas in the three sites that have hills or mounds (Table 6.5).

As expected, the DTM generated for the study sites of the Calibration I and Calibration II did not benefit from the introduction of lower amplitude points. For the Calibration study sites, the introduction of noisy points into the flat terrain could have offset the results of improved accuracy due to increased coverage, thus leaving the quality of the derived DTM practically unchanged. When extracting features that would not be discernible otherwise, such as low amplitude pulses, careful consideration has to be made to find a balance between introducing errors into the model by sacrificing range accuracy and improving the quality of the generated DTM. For further development of the algorithm designed in this research, one potential is the addition of a cost-benefit analysis to evaluate how much point position accuracy can be sacrificed in order to extract additional terrain features. This decision making process would subdivide the scanned area into zones and identify areas that would benefit from having additional point coverage. This classification would assist in determining where the inclusion of the lower amplitude

pulses would benefit the terrain extraction and where it would be detrimental to quality of the derived DTM. There certainly is a need to monitor the accuracy of the derived points, and to have an error value assigned to the coordinates of each point extracted from the LiDAR waveform. In addition, the error estimation methodology introduced in Section 6.1 can be further enhanced and included into the waveform range extraction algorithms. This information will allow the end user to have more flexibility with point cloud data, providing the possibility of selecting points based on the user's accuracy requirements in order to achieve the desired DTM quality. This type of accuracy assessment is generally not considered in LiDAR data processing and could be a potential topic of future work.

In summary, an integrated approach was developed in the course of this research designed to improve the DTM generation from full-waveform LiDAR data. Clear improvement (up to 29%) was demonstrated over an existing methodology in the areas of heavy vegetation and variable terrain.

The software implemented in this research was a result of a top to bottom implementation of the designed methodology. Our approach provided a significant control and flexibility for the algorithm development as most of the aspects of the software were coded internally and thus could be modified and evaluated individually to fulfill the setout objectives.

8 References

Applanix Corporation (2012). POSAV™ Specifications. http://applanix.com/media/downloads/products/specs/POSAV_SPECS_0812.pdf [On-line] May 2012.

Arefi, H., and Hahn, M. (2005). A morphological reconstruction algorithm for separating off-terrain points from terrain points in laser scanning data. *International Archives of Photogrammetry, Remote Sensing and Spatial Information Sciences*, *36*(3/W19).

Axelsson, P. (2000). DEM generation from laser scanner data using adaptive TIN models. *International Archives of Photogrammetry and Remote Sensing*, *33*(B4/1; PART 4): 111-118.

Baltsavias, E. P. (1999). Airborne laser scanning: basic relations and formulas. *ISPRS Journal of Photogrammetry and Remote Sensing*, *54*(2): 199-214.

Cgal, C. G. A. L. (2012). Computational geometry algorithms library. http://www.cgal.org/ [On-Line] Jan 2012.

Chauve, A., C. E. Mallet, F. E. E. Bretar, S. Durrieu, M. P. Deseilligny, and W. Puech, (2007). Processing full-waveform lidat data: modeling raw signals. *International Archives of the Photogrammetry, Remote Sensing and Spatial Information Sciences*, 36(3/W52): 102-107.

Chen, Q., Gong, P., Baldocchi, D., and Xie, G. (2007). Filtering airborne laser scanning data with morphological methods. *Photogrammetric Engineering and Remote Sensing*, *73*(2): 175.

Craymer, M. R. (2006). The evolution of NAD83 in Canada. *Geomatica*, *60*(2): 151-164.

Elmqvist, M. (2002). Ground surface estimation from airborne laser scanner data using active shape models. *International Archives of Photogrammetry Remote Sensing and Spatial Information Sciences*, *34*(3/A): 114-118.

Glennie, C. (2007). Rigorous 3D error analysis of kinematic scanning LIDAR systems. *Journal of Applied Geodesy*, *1*(3): 147.

Gonga-Saholiariliva, N., Gunnell, Y., Petit, C., and Mering, C. (2011). Techniques for quantifying the accuracy of gridded elevation models and for mapping uncertainty in digital terrain analysis. *Progress in Physical Geography*, *35*(6): 739-764.

Green, P. J. (1995). Reversible jump Markov chain Monte Carlo computation and Bayesian model determination. *Biometrika*, *82*(4): 711-732.

Hodgson, M. E., Jensen, J., Raber, G., Tullis, J., Davis, B. A., Thompson, G., and Schuckman, K. (2005). An evaluation of lidar-derived elevation and terrain slope in leaf-off conditions. *Photogrammetric Engineering and Remote Sensing*, *71*(7): 817

Hofton, M. A., Minster, J. B., & Blair, J. B. (2000). Decomposition of laser altimeter waveforms. *Geoscience and Remote Sensing, IEEE Transactions on*, *38*(4): 1989-1996.

Hug, C., Ullrich, A., & Grimm, A. (2004). Litemapper-5600-a waveform-digitizing LiDAR terrain and vegetation mapping system. *International Archives of Photogrammetry, Remote Sensing and Spatial Information Sciences*, *36*(Part 8): W2.

Hyyppä, J., Hyyppä, H., Litkey, P., Yu, X., Haggrén, H., Rönnholm, P., and Maltamo, M. (2004). Algorithms and methods of airborne laser-scanning for forest measurements. *International Archives of Photogrammetry, Remote Sensing and Spatial Information Sciences*, *36*(8/W2): 82-89.

Jalobeanu, A., and Gonçalves, G. R. (2012). The Full-waveform Lidar Riegl LMS-Q680i: From Reverse Engineering to Sensor Modeling. *Proceedings of ASPRS Annual Conference: Sacramento 2012,* 1-9

Jelalian, A. V. (1992) *Laser radar syeterns*. Artech House, Boston and London.

Jing, L., Hu, B., Noland, T., and Li, J. (2012). An individual tree crown delineation method based on multi-scale segmentation of imagery. *ISPRS Journal of Photogrammetry and Remote Sensing*, *70*: 88-98.

Jutzi, B., and Stilla, U. (2005). Measuring and processing the waveform of laser pulses. *Optical*, 194-203.

Jutzi, B., and Stilla, U. (2006). Range determination with waveform recording laser systems using a Wiener Filter. *ISPRS Journal of Photogrammetry and Remote Sensing*, *61*(2): 95-107.

Kraus, K., and Pfeifer, N. (1998). Determination of terrain models in wooded areas with airborne laser scanner data. *ISPRS Journal of Photogrammetry and remote Sensing*, *53*(4): 193-203.

Lin, Y. C., Mills, J. P., and Smith-Voysey, S. (2010). Rigorous pulse detection from full-waveform airborne laser scanning data. *International Journal of Remote Sensing, 31*(5): 1303-1324.

Lin, Y.-C. and J. P. Mills, (2009). Integration of full-waveform information into the airborne laser scanning data filtering process. *International Archives of the Photogrammetry, Remote Sensing and Spatial Information Sciences*, 38 (3/W8): 224-229.

Lin, Y.-C., J. Mills, and S. Smith-Voysey, (2008). Detection of weak and overlapping pulses from waveform airborne laser scanning data. SilviLaser 2008, 478-487, Sept. 17-19, Edinburgh, UK.

Liu, X. (2008). Airborne LiDAR for DEM generation: some critical issues. *Progress in Physical Geography*, *32*(1): 31-49.

Magruder, L. A., and Neuenschwander, A. L. (2009). Lidar full-waveform data analysis for detection of faint returns through obscurants. In *SPIE Defense, Security, and Sensing* (pp. 73230L-73230L). International Society for Optics and Photonics.

Mallet, C., and Bretar, F. (2009). Full-waveform topographic lidar: State-of-the-art. *ISPRS Journal of Photogrammetry and Remote Sensing*, *64*(1): 1-16.

Mallet, C., Bretar, F., and Soergel, U. (2008). Analysis of full-waveform lidar data for classification of urban areas. *Photogrammetrie Fernerkundung Geoinformation*, *5*: 337-349.

Meng, X., Currit, N., and Zhao, K. (2010). Ground filtering algorithms for airborne LiDAR data: a review of critical issues. *Remote Sensing*, *2*(3): 833-860.

Mostafa, M. M., and Schwarz, K. P. (2001). Digital image georeferencing from a multiple camera system by GPS/INS. *ISPRS journal of photogrammetry and remote sensing*, *56*(1): 1-12.

Persson, Å., Söderman, U., Töpel, J., and Ahlberg, S. (2005). Visualization and analysis of full-waveform airborne laser scanner data. *International Archives of Photogrammetry, Remote Sensing and Spatial Information Sciences*, *36*(3/W19): 103-108.

Petrie, G., and Toth, C. K. (2009). Introduction to laser ranging, profiling, and scanning. *Topographic Laser Ranging and Scanning Principles and Processing*, 1-27.

Pfeifer, N., and Briese, C. (2007). Geometrical aspects of airborne laser scanning and terrestrial laser scanning. *International Archives of Photogrammetry, Remote Sensing and Spatial Information Sciences*, *36*(3/W52): 311-319.

Reitberger, J., Krzystek, P., and U. Stilla, 2008. Analysis of full-waveform LiDAR data for the classification of deciduous and coniferous trees. International Journal of Remote Sensing, 29(5): 1407-1431.

Riegl, L. M. S. (2009). *Q560 Technical Specification, Riegl Laser Measurement Systems*, Horn, Austria.

Roncat, A., Wagner, W., Melzer, T., and Ullrich, A. (2008). Echo detection and localization in full-waveform airborne laser scanner data using the averaged square difference function estimator. *The Photogrammetric Journal of Finland*, *21*(1): 62-75.

Schaer, P. (2010). *In-flight quality assessment and data processing for airborne laser scanning* (Doctoral dissertation, ÉCOLE POLYTECHNIQUE FÉDÉRALE DE LAUSANNE).

Schnadt, K., and Katzenbeisser, R. (2004). Unique airborne fiber scanner technique for application-oriented LIDAR products. *International Archives of Photogrammetry, Remote Sensing and Spatial Information Sciences*, *36*(Part 8): W2.

Scott J. (2006). Point in triangle test. http://www.blackpawn.com/texts/pointinpoly/default.html [On-Line] June 2011

Sithole, G. (2001). Filtering of laser altimetry data using a slope adaptive filter. *International Archives of Photogrammetry Remote Sensing and Spatial Information Sciences*, *34*(3/W4): 203-210.

Soille, P. (2003). *Morphological image analysis: principles and applications*. Springer-Verlag New York, Inc.

Soininen, A. (2010). *Terrascan user's guide*. Terrasolid, Helsinki, Finland. www.terrasolid.fi/system/files/tscan_1.pdf [On-line] Oct 10

Stilla, U., and Jutzi, B. (2008). Waveform analysis for small-footprint pulsed laser systems. *Topographic Laser Ranging and Scanning: Principles and Processing*, 215-234.

Stilla, U., Yao, W., and Jutzi, B. (2007). Detection of weak laser pulses by full-waveform stacking. *International Archives of Photogrammetry, Remote Sensing and Spatial Information Sciences*, *36*(Part 3): W49A.

Su, J. and E. Bork, 2006. Influence of vegetation, slope, and LiDAR sampling angle on DEM accuracy. *Photogrammetric Engineering & Remote Sensing*, 72(11):1265-1274.

Vosselman, G. (2000). Slope based filtering of laser altimetry data. *International Archives of Photogrammetry and Remote Sensing*, *33*(B3/2; PART 3): 935-942.

Wagner, W., M. Hollaus, C. Briese, and V. Ducic, 2008. 3D vegetation mapping using small-footprint full-waveform airborne laser scanners. *International Journal of Remote Sensing*, 29(5): 1433-1452.

Wagner, W., Ullrich, A., Ducic, V., Melzer, T., and Studnicka, N. (2006). Gaussian decomposition and calibration of a novel small-footprint full-waveform digitising airborne laser scanner. *ISPRS Journal of Photogrammetry and Remote Sensing*, *60*(2): 100-112

Wagner, W., Ullrich, A., Melzer, T., Briese, C., and Kraus, K. (2004). From single-pulse to full-waveform airborne laser scanners: potential and practical challenges. *International Archives of Photogrammetry and Remote Sensing*, *35*(B3): 201-206.

Wehr, A., and Lohr, U. (1999). Airborne laser scanning—an introduction and overview. *ISPRS Journal of Photogrammetry and Remote Sensing*, *54*(2): 68-82.

Whiteway, J., Daly, M., Carswell, A., Duck, T., Dickinson, C., Komguem, L., and Cook, C. (2008). Lidar on the Phoenix mission to Mars. *Journal of Geophysical Research: Planets (1991–2012)*, *113*(E3).

Zhang, K., Chen, S. C., Whitman, D., Shyu, M. L., Yan, J., and Zhang, C. (2003). A progressive morphological filter for removing nonground measurements from airborne LIDAR data. *Geoscience and Remote Sensing, IEEE Transactions on*, *41*(4): 872-882.

9 Appendices

Appendix A - Implementation of the LM algorithm

As mentioned before, the LM (Levenberg-Marquardt) optimization method is commonly used in the Gaussian decomposition of full-waveform LiDAR returns (e,g, Jutzi and Stilla, 2005 and Chauve et al., 2007) and thus employed in this study as well, and was implemented using the GNU online scientific library. With the key points having been described in the main texts, I will, in this appendix, provide the general workflow and some of the equations used.

The library provides the tools needed to perform the LM optimisation on data. The user still needs to specify the least squares fitting model (Equation 9.1), the partial derivatives with respect to the parameters being estimated, the Jacobian matrix (Equation 9.2), the initial values of the parameters, the waveform data to be fitted and the associated stochastic information.

The partial derivatives of the Gaussian model (Equation 2.5) with respect to μ, A and σ are given by:

$$\partial A_i(t) = e^{-\frac{(t-\mu_i)^2}{2\sigma_i^2}}$$

$$\partial \mu_i(t) = A_i \times e^{-\frac{(t-\mu_i)^2}{2\sigma_i^2}} \times \frac{(t-\mu_i)}{\sigma_i^2} \tag{9.1}$$

$$\partial \sigma_i(t) = A_i \times e^{-\frac{(t-\mu_i)^2}{2\sigma_i^2}} \times \frac{(t-\mu_i)^2}{\sigma_i^3}$$

The Jacobian matrix with N components is given by:

$$J = \begin{bmatrix} \partial A_1(t_1) & \partial \mu_1(t_1) & \partial \sigma_1(t_1) & \partial A_2(t_1) & \partial \mu_2(t_1) & \partial \sigma_2(t_1) & \cdots & \partial A_N(t_1) & \partial \mu_N(t_1) & \partial \sigma_N(t_1) \\ \partial A_1(t_2) & \partial \mu_1(t_2) & \partial \sigma_1(t_2) & \partial A_2(t_2) & \partial \mu_2(t_2) & \partial \sigma_2(t_2) & \cdots & \partial A_N(t_2) & \partial \mu_N(t_2) & \partial \sigma_N(t_2) \\ \vdots & \vdots & \vdots & \vdots & \vdots & \vdots & \ddots & \vdots & \vdots & \vdots \\ \partial A_1(t_j) & \partial \mu_1(t_j) & \partial \sigma_1(t_j) & \partial A_2(t_j) & \partial \mu_2(t_j) & \partial \sigma_2(t_j) & \cdots & \partial A_N(t_j) & \partial \mu_N(t_j) & \partial \sigma_N(t_j) \end{bmatrix} \tag{7.2}$$

The outputs from the LM algorithm are waveform parameters and their associated variance values, as well as the index of goodness-of-fit. These parameters are tested to ensure proper pulse detection.

The LM algorithm is very sensitive to the initial values of parameters. Inadequate initial parameter estimation may cause the solution to diverge due to non-linearity of the initial model. The more accurate the initial estimation of parameters is, the fewer iterations the algorithm will require to converge to a solution.

Correct estimation of number of Gaussians to fit a waveform is essential not only for the overall accuracy of the estimated Gaussian parameters (to avoiding over or under fitting), but also is important for accurate determination of the objects in the beam's path. Errors in under or over fitting at this stage will lead to omission and commission errors.

Appendix B - Site description and statistics

Table 9.1 Site description[1]

Site	Terrain Slope	Species Type	Canopy Cover	Other Comments
Maple	Smooth, intermediate	90% Sugar maple – Shade-tolerant deciduous; 15% oak.	Maple dominant top canopy, dense and closed; Seldom intermediate canopy; A few low understory vegetation which is mostly deciduous.	Younger generation, 20-40 years old
Jack Pine	Flat	90% Jack pine – shade-intolerant coniferous; 10% sugar maple, red maple and balsam fir.	Closed canopy; Jack pine dominant top canopy, relatively open; most of the intermediate foliage of jack pines is dead; other intermediate species are young generation deciduous; definite understory with grass and bushes	40 – 50 years old or more. Most trees are mature. A few dead small jack pines due to natural competition within community.
Mixed	Sharp	60% White birch – shade-intolerant deciduous; 40% Sugar maple – Shade-tolerant deciduous;	Open mixed deciduous forest; isolated white birch occupy high level canopy, but half of them are dead; Maple dominates intermediate canopy; Dense understory cover.	The shape of the birch trees is very irregular. Most of the birch is mature however maple trees are young. Fallen trees are normal in this area. Age of trees cannot be anticipated.
Calibration	Flat	45% Black spruce – shade-tolerant; 45% Sugar maple; 10% balsam fir.	Mixed forest; Open canopy, canopy height is lower. Black spruce and maple both dominant in the top canopy, with intermediate deciduous which are mostly young maple trees. Very little understory or grass.	Forest has been disturbed by human activities or managed. Average height is about 15 metres.

[1] Provided by Jili Li after the survey of the study sites for use in this thesis

The Maple site

Maple is the northernmost site selected. Data were collected in two flight lines; SDF file code 185601 and 186531, north and south flight direction were made available for this research. The density of these scans was 45 points m^{-2} (2 scans overlay). This site has a small hill in the middle of the study site, an earth mount from original highway construction from 1950's.

From ground reference, the following positioning information was made available:

1) 400 Topo points (Acquired Aug 2011)
2) 35 Road points (Acquired Aug 2011)
3) 20 points on side railing poles (Acquired Oct 2011)
4) 75 topo the banks along the highway for determination of the vertical offset (Acquired Oct 2011)

The local traverse for this site is given in Figure 9.1 below.

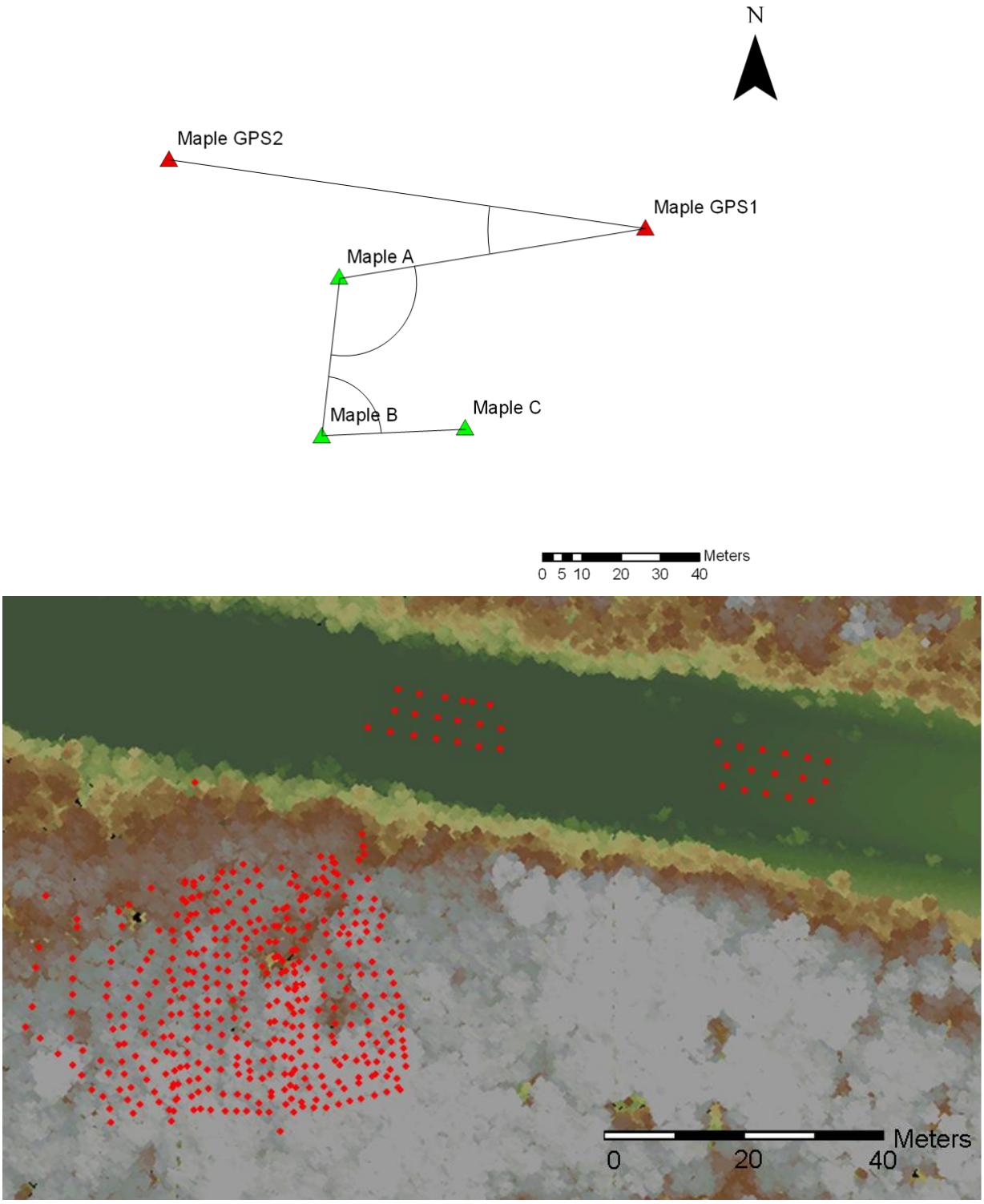

Figure 9.1 Local traverse (top), and ground reference points collected (red) overlaid the LiDAR data (bottom) Maple site

The Mixed woods site

Data were collected in two flight lines (SDF file 184724 and 195317, NORTH and SOUTH flight direction) and have the density of scans of 34 points m^{-2} (2 scans overlay). The site is situated on a steep slope, (part of a larger hill) and contains small hill in the middle, an earth mount is from original highway construction from 1950's.

From ground reference, the following positioning information was made available:

1) 250 topo points (Acquired Aug 2011)
2) 30 road points (Acquired Aug 2011)

The local traverse for this site is shown in Figure 9.2.

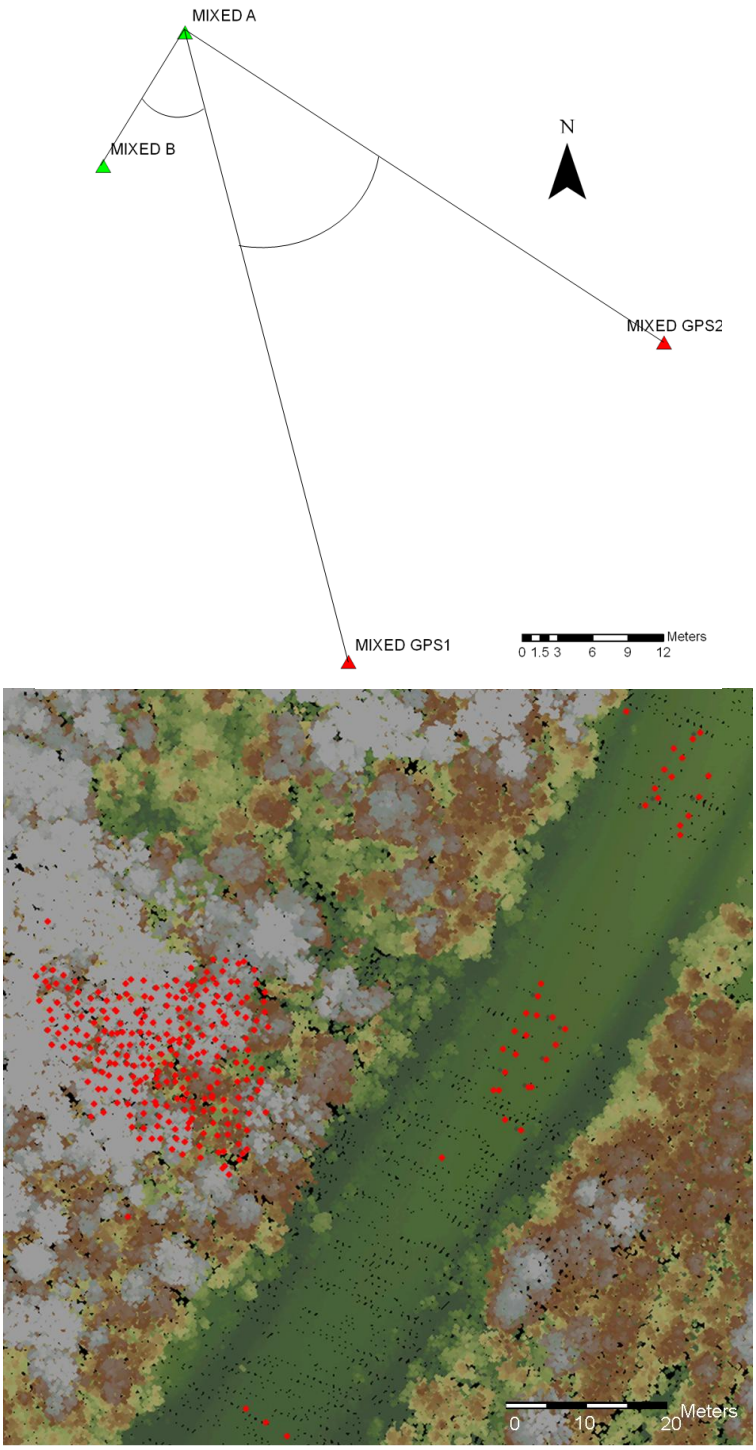

Figure 9.2 Local traverse (top), and ground reference points collected (red) overlaid the LiDAR data (bottom) Mixed Woods site

The Jack Pine site

For this site, data acquisition was carried out along two flight lines (SDF file 184902 and 185151 in the north and south flight directions, respectively), which resulted in the scan density of 36 pulses m^{-2}.

This site is located on gently rolling terrain and has a small hill on the edge of the study site; the mount is from original highway construction from 1950's. The topographic data made available from Survey are as follows:

1) 300 Topo points (Acquired Aug 2011)
2) 30 Road points (Acquired Aug 2011)
3) 6 points on a drain pipe, to check the horizontal accuracy (Acquired Aug 2011)

The local traverse for this site is given in Figure 9.3 below.

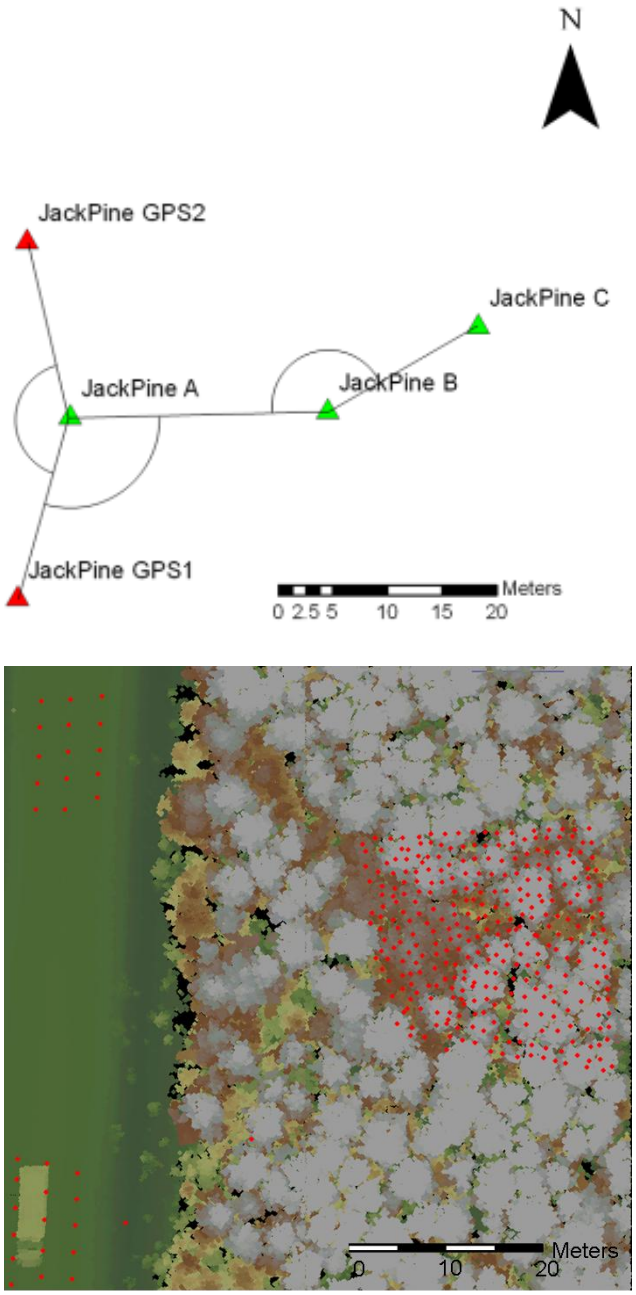

Figure 9.3 Local traverse (top), and ground reference points collected (red) overlaid the LiDAR data (bottom) Jack Pine site

The calibration site 1 and 2

These two study sites are located few tens of metres apart. Data acquisition was carried out along two flight lines (SDF file code 153758 and 154207, south and north flight directions, respectively), which resulted in the scan density of 40 pulses m^{-2} .

One section (Calibration Site 1) contains a small forested area, predominantly spruce trees, with some deciduous and dense understory. From ground reference, the following positioning information was made available:

1) 180 topo points (Acquired Aug 2011)
2) 30 Road points (Acquired Aug 2011)

Second section (Calibration Site 2) contains gently rolling terrain section of an open field. This site was selected for the purposes of determination of vertical datum used in initial data acquisition campaign, as well as a validation of accuracy of LiDAR data.

From ground reference, the following positioning information was made available:

1) 300 topo points (Acquired Aug 2011)
2) 30 Road points (Acquired Aug 2011)
3) 4 posts, to check the accuracy of the survey, and tie the survey with LiDAR (Acquired Aug 2011)

The local traverse for this site is given in Figure 9.4 below.

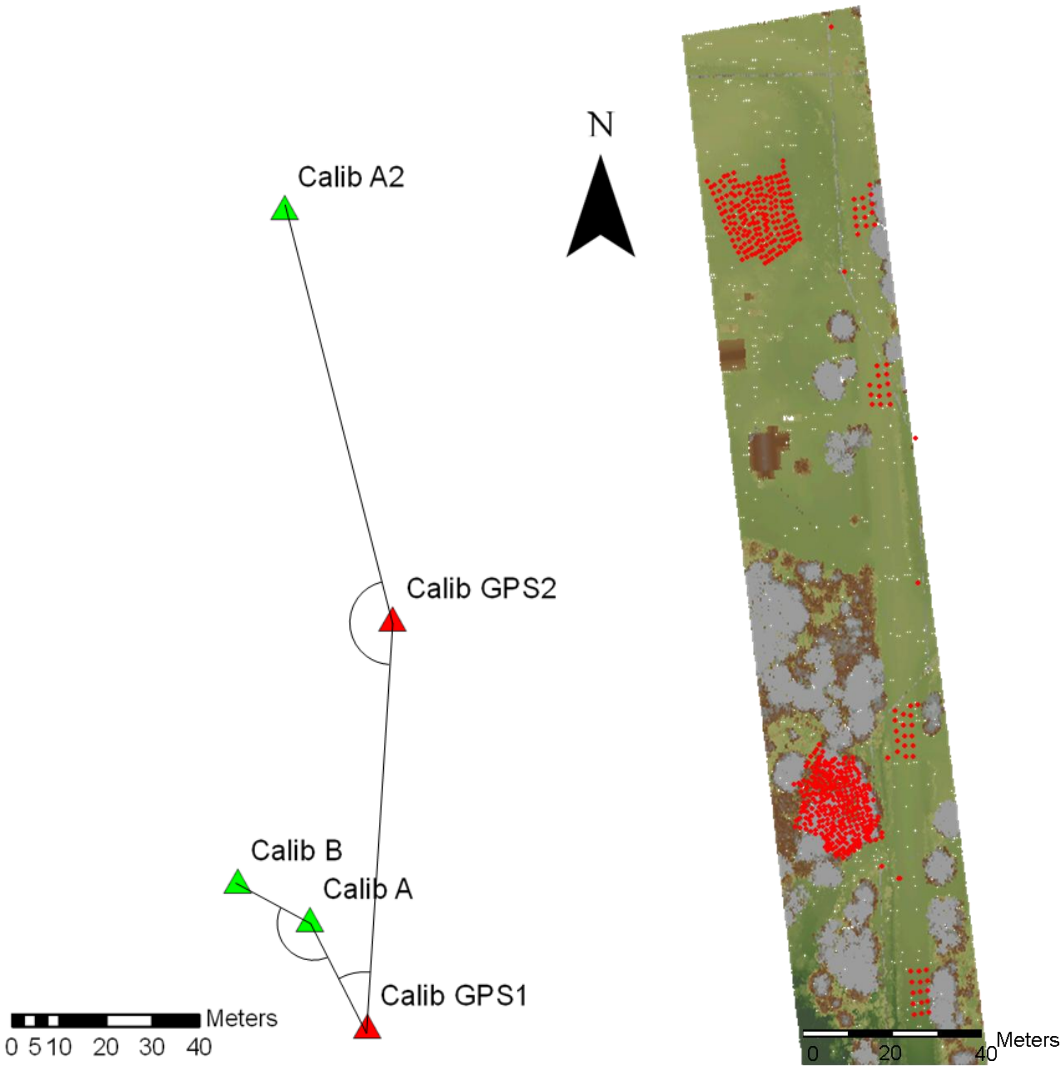

Figure 9.4 Local traverse (left), and ground reference points collected (red) overlaid the LiDAR data (right) Calibration I and II site

Total time of the ground survey

The ground survey was conducted by a two person team, for 7 days in Aug 2011 and then 2 days in Oct 2011.

Appendix C – Data processing

Equipment selection

To provide a good reference data set to validate the generated DTM, the data measured on the ground (referred to as ground reference or topographic data) must have a high accuracy and thus it is important to choose the appropriate equipment. Due to a lack of feature objects in forests which could be used as potential tie points between the topographic measurements and the LiDAR dataset, and also in order to geo-reference the topographic data, Leica 1200 GPS Receivers were used to establish a GPS control network, which linked the surveying area with the closest existing geodetic control points.

Each site was then surveyed using the SOKKIA Set510 total station with Carlson Survey CE data collector, to acquire the topographic data of the area, using the following auxiliary equipment:

Instruments list

Leica 1200 GPS Receivers

SOKKIA Set510

Angular accuracy 5”

Distance accuracy ±(2 + 2xD[km])mm for distances up to 100m

Carlson Data Collector SurvCE

Adaptors/Tribrachs/Tripods

Reflectors

Telescopic rod

Tape

Total station data analysis

The raw files from the data collector were read using the software provided by Carlson (X-Port), the formatted output was then passed to Matlab, where only the needed data were extracted.

Equipment calibration

The following steps were taken to reduce equipment systematic errors. Zero error tests were performed, and the zero error constants for all the total station prism pairings were calculated. All prisms had virtually the same constant value of around 1.2 mm. The collimation and index errors were also computed. Collimation, the horizontal angle misclosure, was calculated to be around 0.5". The index error was variable, due to re-calibration of the Sokkia instrument in the field due to the malfunction of the compensator. There were three different values for index error used for data processing since the re-calibration of the compensator was acknowledged in the field notes.

Traverse data analysis

Station adjustment

Station adjustment was performed on each individual group of observations (from the same station) separately, to produce the final horizontal and vertical angles and distances at each station, which were then used for the traverse calculations. These computations were performed to identify gross outliers and exclude erroneous data from later calculations. The readings for both vertical and horizontal angles at each station were estimated and analyzed.

Since a data collector was used to record the traverse data, the data collection was accomplished in the following manner: Face right BD – FD, Face left FD – BD. To calculate the horizontal angles, the differences between the two consecutive readings (face right and face left) were used (Equation 9.3). If the difference in horizontal angle between face left – face right was more than 10" the angles were discarded. If the difference was less than 10", the two faces were averaged and the resulting values were compared between sets, at which point their standard deviation from the mean value was considered.

For vertical angles, the readings to a target in a single set were averaged and then checked for consistency with other sets. The distances readings to targets were consistent (mm difference) and were just averaged over all the sets.

$$\angle \boldsymbol{\psi}_{AB} = \frac{1}{2}\left[(F.L.)\right]$$

$$\angle \psi_{AB} = \frac{(F.L.\angle \psi_B - F.L.\angle \psi_A) + (F.R.\angle \psi_B - F.R.\angle \psi_A)}{2}$$

$$\angle \psi_{AB} = \frac{(F.L.\angle \psi_B - F.L.\angle \psi_A) + (F.R.\angle \psi_B - F.R.\angle \psi_A)}{2} \qquad (9.3)$$

$$\angle \xi_A = \frac{(F.R.\angle \xi_A + 360 - F.L.\angle \xi_A)}{2}$$

Wherein: F.R. is face right, F.L. is face left, $\angle \psi_{AB}$ is the horizontal angle between A-B and ξ_A is the vertical angle of A

After each set was processed separately the different sets were compared. The average was taken over all the readings and the standard deviation was then calculated. If a gross outlier was found it was removed from the set of observations.

Traverse network analysis

The curvilinear coordinates from GPS1 and GPS2 stations were converted to Cartesian coordinates, using the Equation (9.4).

$$\begin{aligned} X &= (N+h)\cos\phi\cos\lambda \\ Y &= (N+h)\cos\phi\sin\lambda \\ Z &= (N(1-e^2)+h)\cos\phi \end{aligned} \qquad (9.4)$$

$$N = \frac{a}{\sqrt{1-e^2\sin^2\phi}} \qquad (9.5)$$

Wherein *N* is the radius of curvature and is measured from the surface to the Z-axis along the ellipsoid normal, where "*a*" is the semi major axis and "*e*" is the eccentricity of the reference ellipsoid.

After the station adjustment was completed for multiple sets of total station measurements, the vertical and horizontal angles, as well as the target heights and instrument heights were used to calculate the NEU incremental coordinates from the instrument station to a target point (Equation 9.6).

$$\begin{bmatrix} N \\ E \\ U \end{bmatrix} = S \begin{bmatrix} \cos\xi\cos\psi \\ \cos\xi\sin\psi \\ \sin\xi \end{bmatrix} + \begin{bmatrix} 0 \\ 0 \\ \Delta H \end{bmatrix} \tag{9.6}$$

wherein *S* is the slope distance corrected for atmospheric conditions, ξ is the vertical angles from the station to the target, ψ is the azimuth of the target direction $\psi = \psi_0 + \angle\psi_{AB}$, in which $\angle\psi_{AB}$ is the horizontal angle between the backsight and the target direction, and ψ_0 is the azimuth of the backsight direction. And finally $\Delta H = I.H. - T.H.$, which is the difference of the instrument height and the target height.

These NEU values are added to the geocentric coordinates of the "at" station, (Equation 9.7) to obtain the target ECEF coordinates:

$$\begin{bmatrix} X \\ Y \\ Z \end{bmatrix}_{target} = \begin{bmatrix} X \\ Y \\ Z \end{bmatrix}_{station} + T \begin{bmatrix} N \\ E \\ U \end{bmatrix} \tag{9.7}$$

Wherein:

$$T = \begin{bmatrix} -\sin\varphi\cos\lambda & -\sin\lambda & \cos\varphi\cos\lambda \\ -\sin\varphi\sin\lambda & \cos\lambda & \cos\varphi\sin\lambda \\ \cos\varphi & 0 & \sin\varphi \end{bmatrix} \tag{9.8}$$

φ is the latitude at the station

λ is the longitude at the station

The corresponding variance covariance (VCV) matrix of the station coordinates can be calculated using the Equation (9.9):

$$\Sigma_{NEU} = F \begin{bmatrix} \sigma_S^{\,2} & 0 & 0 \\ 0 & \sigma_\xi^{\,2} & 0 \\ 0 & 0 & \sigma_\psi^{\,2} \end{bmatrix} F^T \tag{9.9}$$

With:

$$F = \begin{bmatrix} \cos\xi\cos\psi & -S\sin\xi\cos\psi/\rho'' & -S\cos\xi\sin\psi/\rho'' \\ \cos\xi\sin\psi & -S\sin\xi\sin\psi/\rho'' & -S\cos\xi\cos\psi/\rho'' \\ \sin\xi & -S\cos\xi/\rho'' & 0 \end{bmatrix} \tag{9.10}$$

The resulting variance-covariance matrix Σ_{NEU} is then combined where applicable between consecutive stations to compute the propagated error.

Topographic data analysis

The initial step in coordinate calculation of the topographic points is to apply the applicable corrections. The zero error of the EDM instrument was applied to the distance measurements, as well as the index error in the vertical angle reading was added.

On the basis of the azimuths of the backsight direction calculated from the traverse, the incremental coordinates of the topographic points in NEU were calculated using the horizontal and vertical angle and slope distance measurements from total station for all the topo points with respect to the instrument station as in Equation 9.6. The only difference $\Delta\underline{H}$ of a topo point was calculated as $\Delta H = H.I - H.P.$, wherein the *H.P.* was the height of the survey pole at the topo point. These incremental coordinates in NEU were then converted to the incremental coordinates in ECEF frame using Equation 9.6.

GPS Data Processing

The GPS data processing was performed in two steps: the individual baseline solution using Leica Geo-Office and the least square adjustment of the GPS baseline network using Columbus Best Fitting Software.

Individual Baseline Solution

The GPS collected base station data, were initially processed using the Leica Geo Office software to compute the baselines between two stations. Baseline output from Leica Geo-Office is given in the Table 9.2

Table 9.2 GPS baselines, with standard deviations attached, as per processing with Leica Geo Office

From	To	dX [m]	dY [m]	dZ [m]	σX [mm]	σY [mm]	σZ [mm]	Duration
MIXED2	**478**	-195.892	-282.175	-249.165	0.1	0.2	0.3	43' 31"
50026	**478**	-3909.729	12287.786	12155.341	0.2	0.3	0.3	6h 01' 37"
478	**JACKPINE2**	-9.140	-972.794	-946.561	0.2	0.3	0.3	33' 21"
478	**MAPLE2**	-725.269	713.450	740.507	0.1	0.2	0.3	38' 18"
478	**MAPLE2**	-725.263	713.444	740.51	0.2	0.3	0.4	30' 56"
478	**MIXED2**	195.891	282.177	249.16	0.2	0.3	0.3	39' 43"
478	**JACKPINE2**	-9.165	-972.786	-946.573	0.3	0.6	0.7	42' 11"
MAPLE2	**MAPLE1**	85.188	-6.793	-7.993	0.2	0.3	0.3	1h 24' 05"
MAPLE2	**MAPLE1**	85.189	-6.792	-7.997	0.1	0.1	0.1	6h 26' 30"
MIXED1	**MIXED2**	16.162	21.420	18.941	0.1	0.1	0.1	4h 13' 21"
JACKPINE1	**JACKPINE2**	-0.363	23.649	22.574	0.1	0.2	0.2	4h 12' 16"
478	**JACKPINE1**	-9.506	-949.093	-924.007	0.2	0.5	0.5	1h 53' 45"
CALIB1	**CALIB2**	-2.159	-62.929	-59.354	0.2	0.3	0.3	1h 22' 32"
50026	**CALIB2**	-1071.294	614.819	700.867	0.2	0.4	0.4	1h 58' 09"
478	**MIXED1**	179.73	260.766	230.230	0.2	0.4	0.5	1h 23' 55"
478	**MAPLE1**	-640.089	706.670	732.517	0.2	0.4	0.5	1h 57' 36"

Adjustment of GPS Baseline Network

The GPS baseline network constructed from the baseline measurements was then adjusted using the Columbus Best Fit Computing. The chosen horizontal control was the control point 00819950063, since the other control point: 00820000478, was found to be compromised (most likely shifted during re-pavement of the highway 126). The adjusted geodetic coordinates of topographic mapping control points are given in Table 9.3:

Table 9.3 Final station coordinates and errors from Columbus ITRF 2005

Station	Latitude (N) (d m s)	SD (m)	Longitude (W) (d m s)	σ (m)	Ellip. Height (m)	SD (m)
478	46-34-40.05952	0.009	83-25-14.36061	0.0074	291.802	0.009
50026	46-25-11.80741	0	83-23-18.41225	0	186.466	0
CALIB1	46-25-47.45895	0.0138	83-24-04.49872	0.0105	188.380	0.0138
CALIB2	46-25-44.67315	0.0104	83-24-04.93784	0.0074	188.292	0.0104
JACKPINE1	46-33-57.34057	0.0119	83-25-19.91023	0.0092	268.183	0.0119
JACKPINE2	46-33-56.28435	0.0112	83-25-20.02064	0.0089	267.981	0.0112
MAPLE1	46-35-14.60047	0.011	83-25-40.42475	0.0088	290.997	0.0111
MAPLE2	46-35-15.16643	0.0106	83-25-44.36325	0.0083	285.469	0.0106
MIXED1	46-34-50.79247	0.0111	83-25-04.57192	0.0089	295.126	0.0111
MIXED2	46-34-51.67093	0.0105	83-25-03.70257	0.0084	295.530	0.0106

Note: Station 00820000478 (control point) has a 7 cm difference in ellipsoidal height, if calculated using the GPS baseline instead of being fixed as a control station.

Appendix D – The control points

The two control points were obtained from COSINE Online Service

(http://www.cosine.mnr.gov.on.ca/cosine) as follows:

STATION: **00820000478**
Horizontal datum: NAD-1983:CSRS:CBNv3-1997.0
Accuracy: ..... CSRS class D
Latitude: .....N46°34'40.05648"
Longitude: ..... W83°25'14.37228"
Ellipsoidal elevation: 291.876
UTM-17 Easting: E314526.317
UTM-17 Northing:.....N5161094.064
UTM-17 Cmbd sc-fact:.....0.99997710
UTM-17 Mrdnl convg: ..... -1°45'31.1"

STATION: **00819950063**
Horizontal datum: NAD-1983:CSRS:CBNv3-1997.0
Horizontal accuracy: ..... CSRS class D
Latitude: .....N46°25'11.80741"
Longitude: ..... W83°23'18.41225"
Ellipsoidal elevation: 186.466
UTM-17 Easting: E316463.658
UTM-17 Northing:.....N5143480.156
UTM-17 Cmbd sc-fact:.....0.99998485
UTM-17 Mrdnl convg: ..... -1°43'50.5"

Appendix E – Horizontal datum and orthometric height

NAD 1983 CSRS: CBN v3-1997

The coordinates of control points were provided in NAD 1983 CSRS:CBN v3-1997. A transformation was required in order to have these coordinates with WGS84 ITRF 2005. There is no conversion from specific transformation from CBN v3 at 1997.0 to WGS84. There is however the Helmert transformations from the fundamental realizations of NAD83(CSRS) reference frame (which was 1997.0) to the various realizations of ITRF. And WGS84 is derived from specific ITRF's (Craymer 2006).

Depending on ITRF needed, the transformations are performed using that epoch's specific parameters, an example of these parameters are given in Table 9.4.

Table 9.4 Example of ITRF2005 transformation parameters

Items	***TX* m**	***TY* m**	***TZ* m**	***RX* mas**	***RY* mas**	***RZ* mas**	***DS* ppb**
Parameters	0.9963	-1.9024	-0.5219	-25.915	-9.426	-11.599	-0.775
Items	***dTX* m/y**	***dTY* m/y**	***dTZ* m/y**	***dRX* mas/y**	***dRY* mas/y**	***dRZ* mas/y**	***dDS* ppb/y**
Parameters	0.0005	-0.0013	0.0019	-0.067	0.757	0.051	-0.102

The transformations and the relationship between NAD83(CSRS) and ITRF is demonstrated by the formulas 9.11 and 9.12 below.

$$\begin{bmatrix} X_N \\ Y_N \\ Z_N \end{bmatrix} = \begin{bmatrix} T_X(t) \\ T_Y(t) \\ T_Z(t) \end{bmatrix} + \begin{bmatrix} 1+DS(t) & -R_Z(t) & R_Y(t) \\ R_Z(t) & 1+DS(t) & -R_X(t) \\ -R_Y(t) & R_X(t) & 1+DS(t) \end{bmatrix} \begin{bmatrix} X_I(t) \\ Y_I(t) \\ Z_I(t) \end{bmatrix} \quad (9.11)$$

wherein, X_N, Y_N, Z_N are the geocentric Cartesian coordinates in NAD83(CSRS) at epoch of observation. $X_I(t)$,$Y_I(t)$,$Z_I(t)$ are the geocentric Cartesian coordinates in ITRF at epoch t.

The constants in the equation above are calculated using the following formulas.

$$
\begin{aligned}
T_X(t) &= T_X + dT_X(t)\cdot(t-1997.0)m \\
T_Y(t) &= T_Y + dT_Y(t)\cdot(t-1997.0)m \\
T_Z(t) &= T_Z + dT_Z(t)\cdot(t-1997.0)m \\
R_X(t) &= [R_X + dR_X\cdot(t-1997.0)]\cdot krad \\
R_Y(t) &= [R_Y + dR_Y\cdot(t-1997.0)]\cdot krad \\
R_Z(t) &= [R_Z + dR_Z\cdot(t-1997.0)]\cdot krad \\
DS(t) &= DS + dDS\cdot(t-1997.0)\,ppb
\end{aligned}
\qquad (9.12)
$$

wherein, t is the epoch of ITRF coordinates and constant k is given as 4.84813681 x 10^{-9} rad/mas.

In summary, in order to compute the WGS84 coordinates in a relevant ITRF realization, one needs to use the correct transformation parameters, which are determined by the epoch in which the final ITRF needs to be, and the epoch of observation.

Orthometric and ellipsoidal heights

The heights determined from GPS measurements are generally ellipsoidal heights with WGS84. The heights of the LiDAR dataset that was acquired in 2009 were the orthometric heights. Unfortunately the specific vertical system (orthometric height) used

for calculation of navigational solution was not provided with the dataset, thus the vertical offset had to be computed from the collected data and compared to a known database of height offsets in order to find a match.

The offsets between the ellipsoidal and orthometric heights were gathered from the following online service: The Natural Recourses Canada's (NRCan) GPS vH 2.1 Geoid Height Transformation Program[2]. NRCan's GPS H v2.1 software supports multiple Geoid Models (different years and sources). The orthometric elevations obtained from the software for the surveyed stations are listed in Table 9.5.

Table 9.5 The different geoid heights for the stations, obtained via GPS H 3.1 Software

Station	Latitude (N)	Longitude (W)	Ellipsoidal Height	EGM95 NAD83 (CSRS)	EGM95 ITRF (2005)	***CGVD28 NAD83 (CSRS)***	CGVD28 ITRF (2005)	EGM08 NAD83 (CSRS)	EGM08 ITRF (2005)	LiDAR minus Survey Data
00820000478	46-34-40.05952	83-25-14.36061	291.8018	-35.633	-36.625	**-36.54**	-37.532	-36.126	-37.118	**N/A**
00819950026	46-25-11.80741	83-23-18.41225	186.466	-35.88	-36.877	**-36.822**	-37.819	-36.371	-37.368	**N/A**
CALIB1	46-25-47.45895	83-24-04.49872	188.3796	-35.868	-36.865	**-36.806**	-37.803	-36.359	-37.356	**36.84**
CALIB2	46-25-44.67315	83-24-04.93784	188.2919	-35.869	-36.866	**-36.807**	-37.804	-36.36	-37.357	**36.82**
JACKPINE1	46-33-57.34057	83-25-19.91023	268.1827	-35.655	-36.647	**-36.566**	-37.559	-36.15	-37.143	**36.54**
JACKPINE2	46-33-56.28435	83-25-20.02064	267.981	-35.656	-36.648	**-36.567**	-37.559	-36.151	-37.143	**36.54**
MAPLE1	46-35-14.60047	83-25-40.42475	290.9971	-35.615	-36.606	**-36.523**	-37.515	-36.111	-37.103	**36.44**
MAPLE2	46-35-15.16643	83-25-44.36325	285.4689	-35.615	-36.607	**-36.524**	-37.515	-36.112	-37.104	**36.44**
MIXED1	46-34-50.79247	83-25-04.57192	295.1256	-35.625	-36.617	**-36.531**	-37.523	-36.118	-37.110	**36.47**
MIXED2	46-34-51.67093	83-25-03.70257	295.5312	-35.625	-36.617	**-36.531**	-37.523	-36.117	-37.109	**36.47**

[2] webapp.geod.nrcan.gc.ca/geod/tools-outils/index.php

From the table, the orthometric height correction CGVD28 in NAD83 (CSRS) was found to be the best fit to the LiDAR data (Table 9.5, column: “LiDAR minus survey data”). This correction was the closest in value to the discrepancy encountered when the elevation data from the field survey is compared with the airborne LiDAR data. Thus the ground data vertical values were transformed using the CGVD28 NAD83(CSRS) height transformation to make them compatible to the LiDAR data collected.

Appendix F – Tie points

In order to provide a measure of consistency in horizontal coordinates between LiDAR collected data and ground survey acquired points, an attempt was made in the field to collect features that were discernible in the LiDAR dataset. Due to the passage of time since the data acquisition and the re-pavement of the highway 129, many of the collected points could not be used for the purposes of validation. Below the full list of objects collected for the horizontal accuracy assessment is provided at each site.

Maple site

Road Centreline

Although the road was repaved, the center line was close to the surveyed position (Figure 9.5).

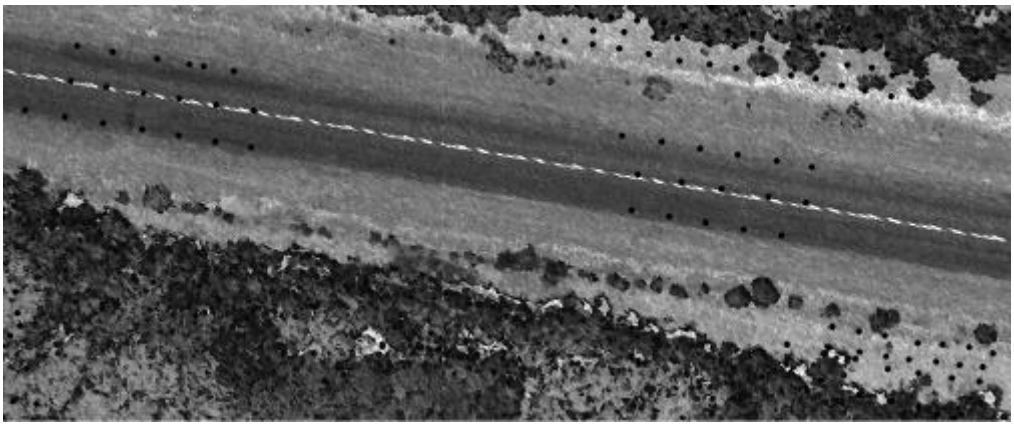

Figure 9.5 LiDAR intensity image, road Maple with survey points overlay

The measured road markings in the east section of the plot were less than 10 cm south of the LiDAR acquired center line, and in the west section these were around 15 cm north of the LiDAR acquired center line.

Road Fence Posts

The images from 2009 and 2011 demonstrated that new posts and fence were installed. Thus no comparison could be made. Figure 9.6 demonstrates that the locations of the posts on the intercity LiDAR plot and collected by ground survey do not coincide.

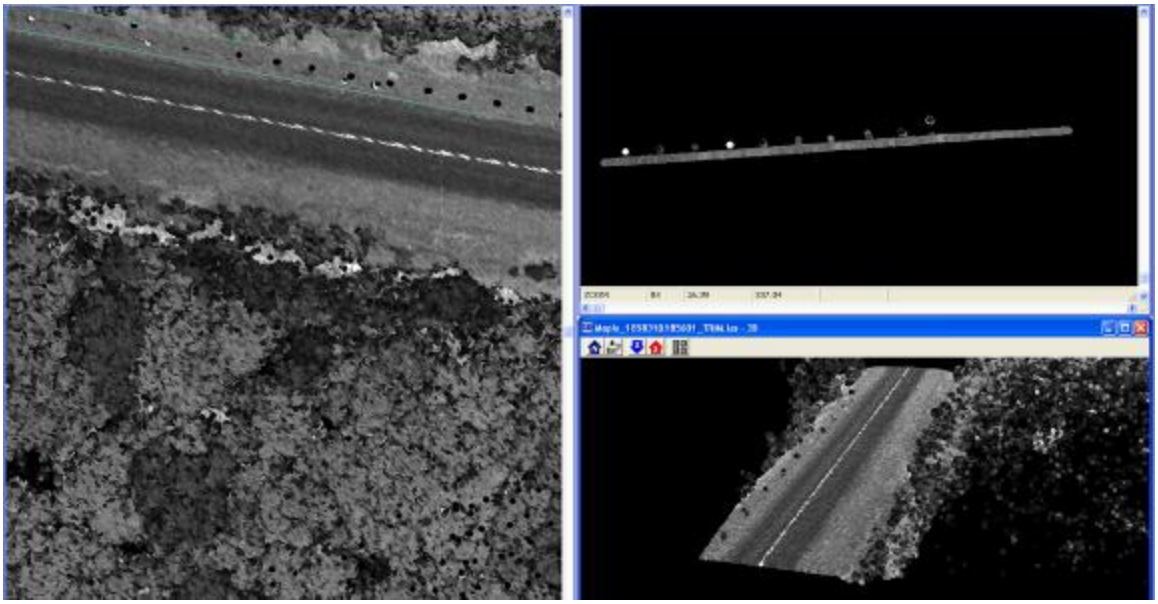

Figure 9.6 LiDAR intensity image, road fence posts Maple with survey points overlay

Mixed woods site

Road Centreline

Again, even though the road was repaved, the center line seems to be close to the original position with an offset ~15 cm (Figure 9.7). Due to the inconsistencies with the data collection other points could not be used for the comparison.

Figure 9.7 LiDAR intensity image, road Mixed site with survey points overlay

Calibration I and II sites

Road Centreline

No center line was visible on the intensity plot, however good vertical alignment was obtained, with standard deviation value of ~1 cm (1σ) and a mean offset of few mm.

Utility Poles

Locations of four utility posts were surveyed at the Calibration site. Out of four utility poles surveyed one was seemingly replaced since the data acquisition campaign (visually looked new from site photos). The remaining three posts matched well across the two datasets. There was also a road sign on the site that was visible from the acquired LiDAR data. Upon comparison to the survey data the horizontal coordinates matched the LiDAR data very well. The offsets between the ground truth and the LiDAR data are provided in Table 9.6.

Table 9.6 Posts and sign coordinate comparison, collected as part of accuracy assessment of Calibration Site. Pole 1 has been replaced since the original LiDAR survey.

Point ID	Physical location on the object	LAS Dataset Coordinates[m] Easting, Northing, Height			Surveyed Coordinates [m] Easting, Northing, Height		
***Pole 1**	South-East Side	776474.420	5148020.850	228.67	776474.591	5148020.723	189.113
Pole 2	South Side	776463.580	5148194.390	226.16	776463.624	5148194.413	187.973
Pole 3	South Side	776459.640	5148265.800	227.00	776459.742	5148265.821	189.610
Pole 4	North-West Side	776484.370	5148145.660	228.70	776484.368	5148145.730	189.236
Sign 1	Tip	776476.110	5148052.420	228.21	776476.188	5148052.415	187.953

Point ID	dE	dN	Horizontal[m]
***Pole 1**	-0.127	0.171	0.213
Pole 2	0.023	0.044	0.050
Pole 3	0.021	0.102	0.105
Pole 4	0.070	-0.002	0.070
Sign 1	-0.005	0.078	0.078

Jack Pine site

Road Centreline

Due to the re-pavement of the road, the surveyed position of the center line was far from the position in the LiDAR intensity plot. The centreline in the northern section (Figure 9.8) of the study site was deviated about 40 cm to the East from the LiDAR data.

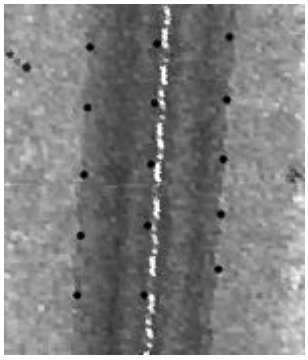

Figure 9.8 LiDAR intensity image, road (northern segment) jack pine site with survey points overlay

The south section (Figure 9.9) appeared to have the difference of less than 10 cm with the centreline.

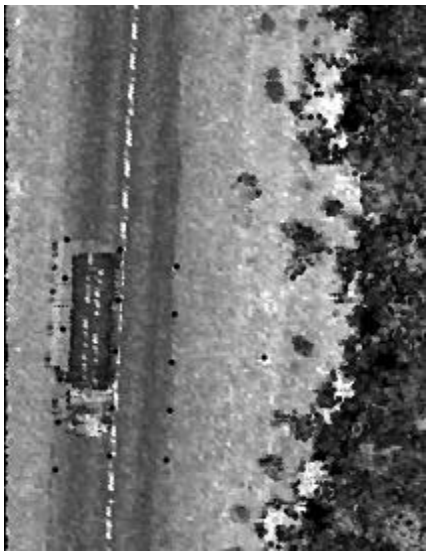

Figure 9.9 LiDAR intensity image, road (southern segment) jack pine site with survey points overlay

GPS1 and GPS2 markers

There were GPS ground check points present at this site, covered by about 1 m by 1 m check board pattern reflective material (Figure 9.10). These targets were installed during the initial data acquisition in 2009 and had survived until ground reference acquisition campaign in 2011. The GPS point (mark in red in Figure 9.10) fit the LiDAR data well.

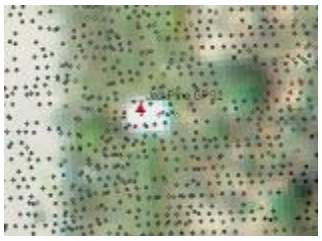

Figure 9.10 Ortho photo, Jack Pine GPS2 (red triangle) overlaid with LiDAR data

Drainage pipe

A drainage pipe, running perpendicularly under the road having a diameter of 1.1 m, was clearly visible in the scan. Six points were surveyed along the pipe: two corresponding to the left and right most tips, two more at the location where the pipe disappeared under the pavement, and two between on either side (Figures 9.11 and 9.12).

Figure 9.11 Orthophoto, Jack Pine drainage pipe, with survey data overlay

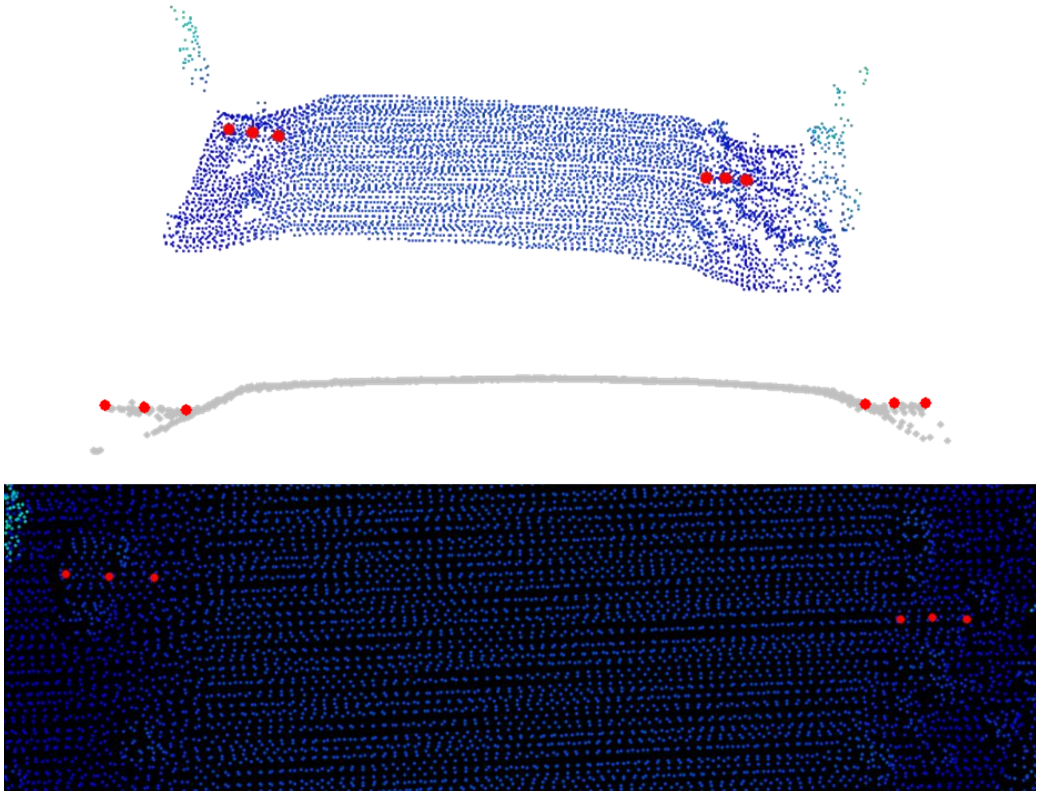

Figure 9.12 Drainage pipe LiDAR data with survey points overlaid (survey points are in red), 3D view, profile view and top view.

From the LiDAR dataset, the points corresponding to the tip of the pipes were extracted, and their coordinates were compared.

Table 9.7 Pipe edge tie points comparisont

	LAS File Coordinates [m]		Surveyed Coordinates [m]		
Point ID	**E**	**N**	**E**	**N**	**Displacement [m]**
Pipe 1	774175.100	5163231.990	774175.055	5163231.990	0.045
Pipe 6	774195.860	5163230.980	774195.877	5163230.945	0.039

The LiDAR points corresponding to the ridge of the pipe were fitted using equation of the line to have produced the following best fit equation:

$$Y = -0.0497226X + 5201734.529$$

Using the equation of the line of best fit together with the Easting coordinates obtained from the survey, the Northing coordinates of the pipe were re-estimated. The obtained displacement between the survey derived coordinates and the LiDAR points are given in Table 9.8.

Table 9.8 Pipe tie points comparison to linear fit

	Surveyed Coordintaes [m]		Derived using equation of the line	
Point ID	**E**	**N**	**Est. N**	**Displacement Surveyed N – Est. N**
Pipe 1	774175.055	5163231.990	5163231.961	-0.029
Pipe 2	774176.058	5163231.937	5163231.912	-0.025
Pipe 3	774177.116	5163231.909	5163231.859	-0.050
Pipe 4	774194.345	5163230.957	5163231.002	0.046
Pipe 5	774195.071	5163230.981	5163230.966	-0.015
Pipe 6	774195.877	5163230.945	5163230.926	-0.019

The horizontal control in N-S direction indicated a good degree of accuracy. The tips of the pipe demonstrated that the E-W direction matched well between the ground reference and LiDAR data.

Appendix G – Quality assessment tools used

To run a comparative analysis on the derived DTM's to assess the quality of resulting product a set of functions specified in this chapter was implemented in Matlab. Two different methods were used to analyze the quality of the DTMs obtained; one method involved using the IDW (inverse distance weighting) and another TIN distance analysis. These were used to interpolate the DTMs obtained from LiDAR to estimate the heights at coordinates corresponding in location to ground reference points, in order to perform a valid comparison to the survey collected elevation values.

IDW (inverse distance weighting), algorithm first assigns weights based on distance to the points located in the neighbourhood of the point whose height is being estimated (Equation 9.13, Figure 9.13). The inverse square distance weighting relationship was used here.

$$w_i = \frac{\left(d_{pi}{}^2\right)^{-1}}{\sum_{k=1}^{n}\left(d_{pk}{}^2\right)^{-1}} \qquad (9.13)$$

Wherein d_{pi} is the radial distance from point estimated p to a neighboring point i. The neighbourhood is composed of a total of n points (thus the bottom of the equation is a sum of square of distances to the n nearest points), resulting in a weight w_i assigned to the Z value at point i.

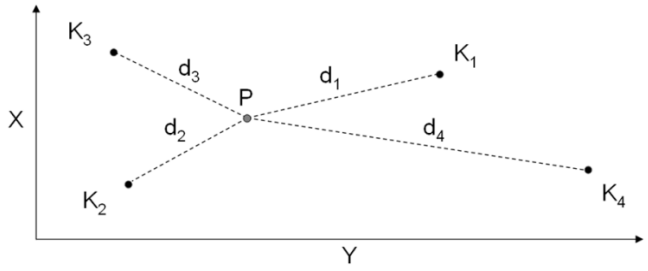

Figure 9.13 IDW, using distance to assign weights to points

By applying the weights obtained in Equation 9.13 to the height of each neighbourhood point and summing these values up as per Equation 9.14 the estimate for the Z value of the new point *p* can be obtained.

$$Z_p = \sum_{k=1}^{n} \left(w_k Z_k \right) \tag{9.14}$$

It is possible to impose further conditions on this algorithm, here we chose to restrict the neighbourhood search space to 5 m and only use 5 closest points for calculation of elevation.

TIN model distance analysis is accomplished by initially generating a TIN model and then extracting the elevation value at the horizontal coordinate corresponding in location to the point being interpolated. Here the ground truth points collected are compared to the TIN generated from LiDAR point cloud.

In order to find the facet where the point *P* falls in, Equation 5.4 for Barycentric Technique is again used from Section 5.2.2 above.

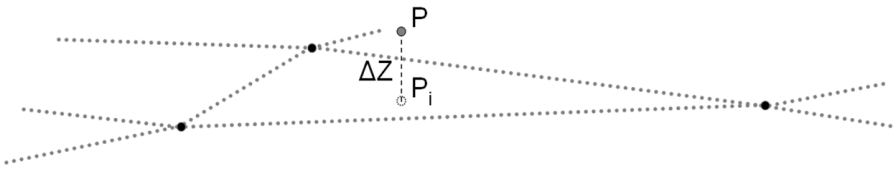

Figure 9.14 Projecting a point *P* onto a surface of a TIN facet to estimate the height difference (ΔZ) between the point on the surface of the facet P_i and initial point *P*

Substituting the X, Y coordinate pair of point *P* (X_p, Y_p) into the equation of the plane (for the facet) as per Equation 9.15, produces the Z value at that location, thus the residual can be easily obtained via:

$$\begin{aligned} Z &= a_i X + b_i Y + c_i \\ Z_{pi} &= a_i X_p + b_i Y_p + c_i \\ \Delta Z &= Z_p - Z_{pi} \end{aligned} \qquad (9.15)$$

Wherein a_i, b_i, c_i, are parameters describing equation of the plane for facet *i*, Z_{pi} was the projected value for Z on facet *i* for point *P*, ΔZ was the resulting residual from differencing the original value of height at point *P* and calculated projected height.

For both assessment methods described above, the horizontal X and Y coordinates of the ground reference data were used to calculate the Z value by interpolating the LiDAR derived DTMs. The final obtained residual values are the offsets from the vertical of the ground reference data to the location of the derived Z value of the LiDAR DTMs with the same X and Y coordinates. A positive residual demonstrates that LiDAR DTM is above the ground reference data thus negative residual show that the DTM derived point is below the survey data.

Appendix H – Additional experimental result plots

Figure 9.15 provides the histogram distribution of the residuals at each site. A positive residual demonstrates that LiDAR DTM is above the ground reference data and a negative residual indicates that the DTM derived point is below the surveyed data.

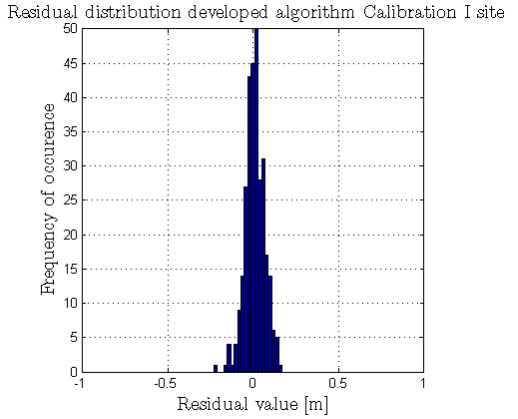

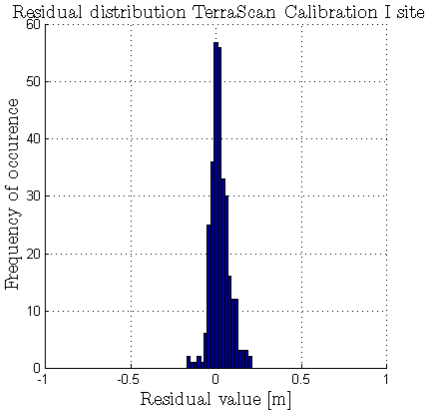

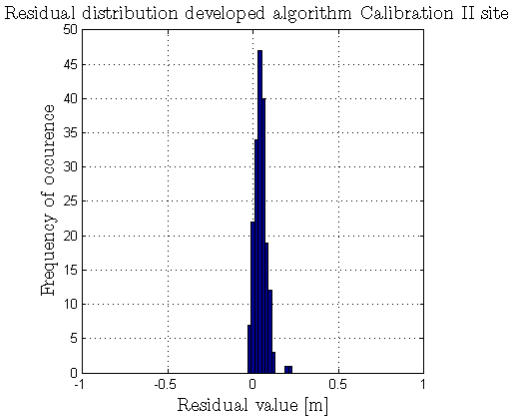

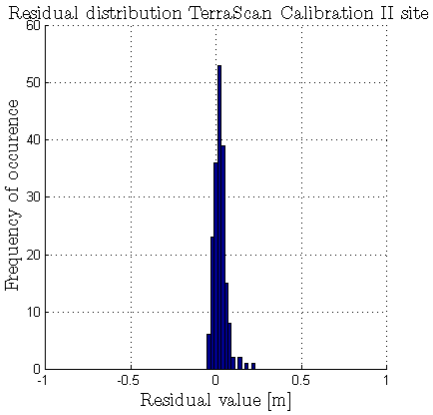

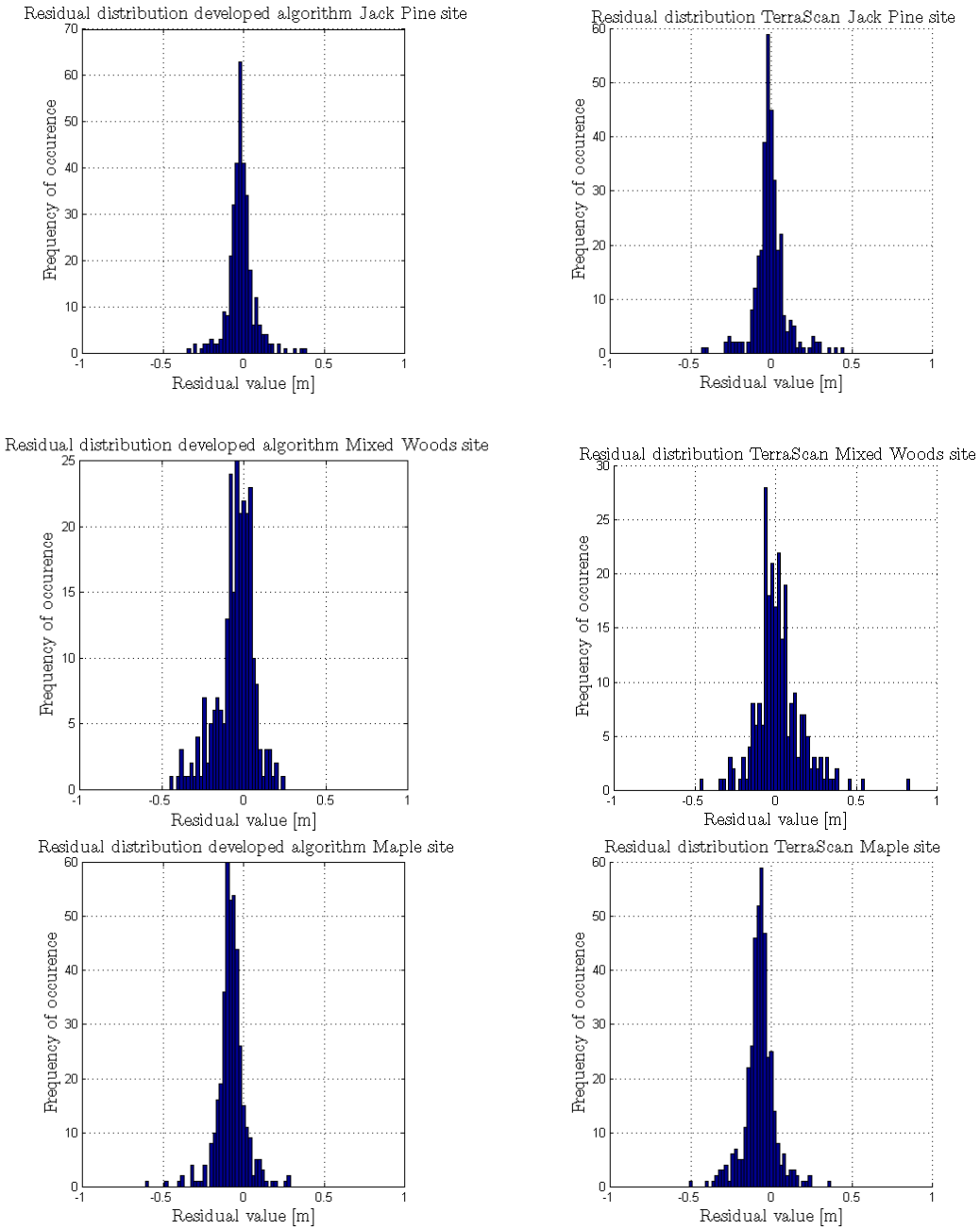

Figure 9.15 Histogram distribution of residuals obtained using TIN model distance comparison of the LiDAR derived DTMs with the ground reference data.

All the histograms of the residual distributions in Figure 9.15 appear to follow a normal distribution pattern.

Below are the plots of spatial distribution of residuals obtained using TIN model distance comparison of the LiDAR derived DTMs with the ground reference data. The colour of the error bars signifies the sign of the residual value, red – negative, blue – positive. The scale of the residuals is: 5:1 (1 metre plot distance is a 0.2 m residual magnitude).

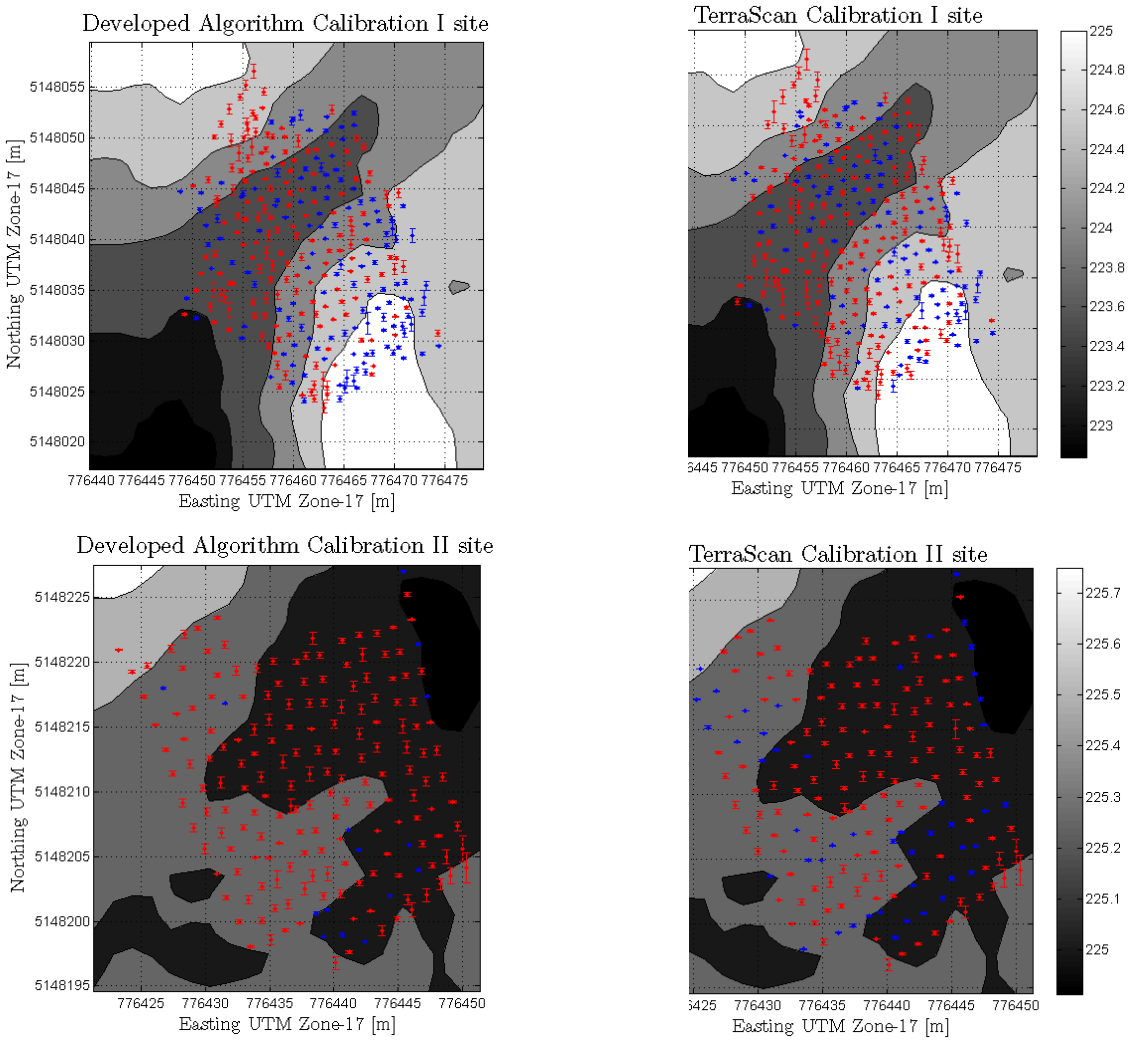

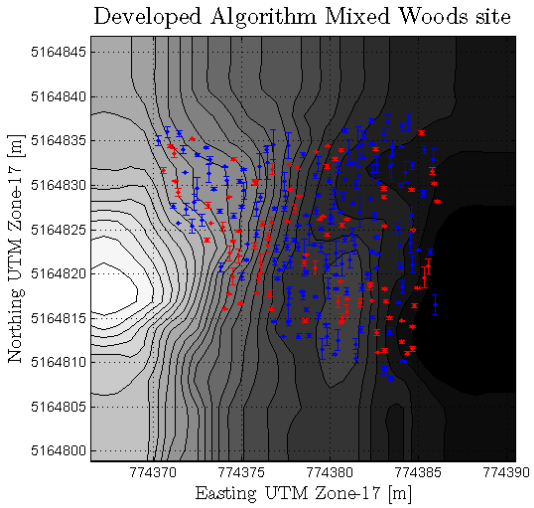
Developed Algorithm Mixed Woods site
Northing UTM Zone-17 [m]
5164845
5164840
5164835
5164830
5164825
5164820
5164815
5164810
5164805
5164800
774370
774375
774380
774385
774390
Easting UTM Zone-17 [m]

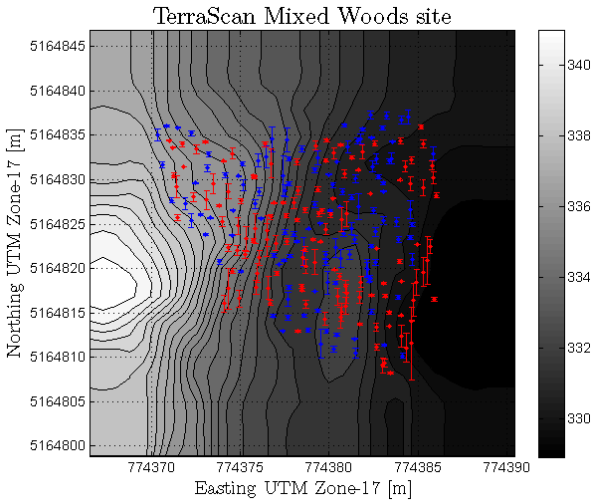
TerraScan Mixed Woods site
Northing UTM Zone-17 [m]
5164845
5164840
5164835
5164830
5164825
5164820
5164815
5164810
5164805
5164800
774370
774375
774380
774385
774390
Easting UTM Zone-17 [m]
340
338
336
334
332
330

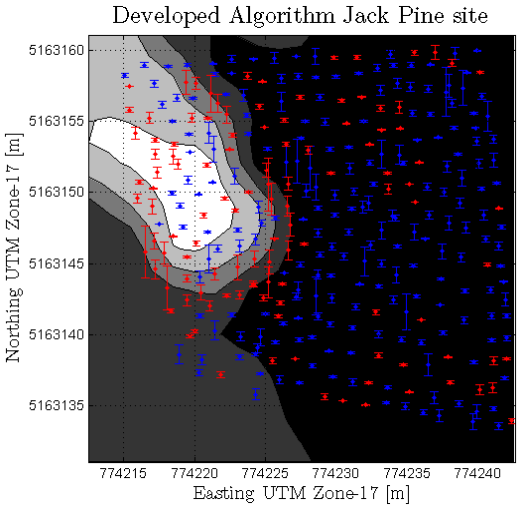
Developed Algorithm Jack Pine site
Northing UTM Zone-17 [m]
5163160
5163155
5163150
5163145
5163140
5163135
774215
774220
774225
774230
774235
774240
Easting UTM Zone-17 [m]

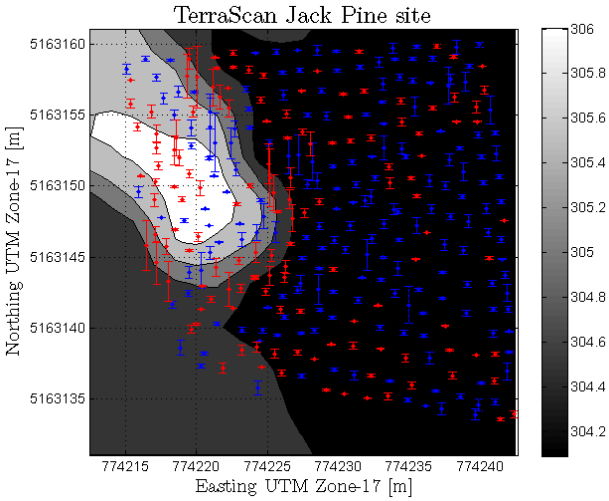
TerraScan Jack Pine site
Northing UTM Zone-17 [m]
5163160
5163155
5163150
5163145
5163140
5163135
774215
774220
774225
774230
774235
774240
Easting UTM Zone-17 [m]
306
305.8
305.6
305.4
305.2
305
304.8
304.6
304.4
304.2

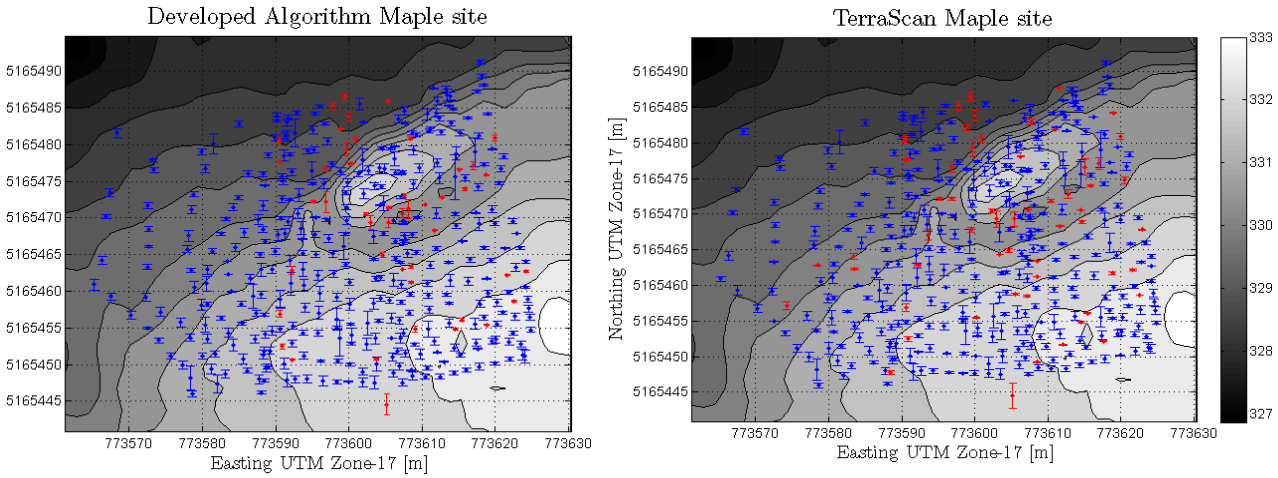

Figure 9.16 Spatial representation of residual distribution at each site The scale of the residuals is: 5:1 (1 metre plot distance is a 0.2m residual magnitude).

All the residual distributions in Figure 9.16 appear to be mostly random in nature, with the developed algorithm residual values showing improvement in the areas of higher terrain variations.